

Juho Montonen

## **INTEGRATED HUB GEAR MOTOR FOR HEAVY-DUTY OFF-ROAD WORKING MACHINES – INTERDISCIPLINARY DESIGN**

Thesis for the degree of Doctor of Science (Technology) to be presented with due permission for public examination and criticism in the Auditorium of the Student Union House at Lappeenranta University of Technology, Lappeenranta, Finland on the 23<sup>rd</sup> of March, 2017, at noon.

Acta Universitatis  
Lappeenrantaensis 735

Supervisors Professor Juha Pyrhönen  
LUT School of Energy Systems  
Lappeenranta University of Technology  
Finland

Dr. Pia Lindh  
LUT School of Energy Systems  
Lappeenranta University of Technology  
Finland

Reviewers Professor Wen-Ping Cao  
School of Engineering and Applied Science  
Aston University  
Great Britain

Professor Kurt Stockman  
Department of Industrial System and Product Design  
University of Ghent  
Belgium

Opponents Professor Kurt Stockman  
Department of Industrial System and Product Design  
University of Ghent  
Belgium

Professor Tapani Jokinen  
School of Electrical Engineering  
Aalto University  
Finland

ISBN 978-952-335-052-6  
ISBN 978-952-335-053-3 (PDF)  
ISSN-L 1456-4491  
ISSN 1456-4491  
Lappeenrannan teknillinen yliopisto  
LUT Yliopistopaino 2017

# Abstract

**Juho Montonen**

Dissertation, Lappeenranta University of Technology

Lappeenranta 2017

99 pages

Acta Universitatis Lappeenrantaensis 735

Diss. Lappeenranta University of Technology

ISBN 978-952-335-052-6, ISBN 978-952-335-053-3 (PDF), ISSN-L 1456-4491,

ISSN 1456-4491

This doctoral dissertation studies solutions that meet the demands made for the propulsion motors of off-road working machines. It has been shown that in a hybridization process, without a mechanical gear, it is not possible to cover all the required torque-speed operating points set by the driving conditions of the traditional off-road working machine without largely overdimensioning the electrical components.

The dissertation presents a novel solution, which combines a two-step planetary gearbox and a tooth-coil permanent magnet synchronous machine with embedded magnets to solve the problem. The important boundary conditions in terms of the electromagnetic design, mechanics, and cooling are discussed. The high design flexibility offered by permanent magnet synchronous machines is utilized to the full to find a feasible integrated design. Furthermore, the dissertation presents a solution for a gear change mechanism, which is located inside an integrated electric motor gear assembly.

The designed and measured performance of the integrated system meets the needs of many off-road working machines. The prototype motor has about 40 kW power and could be adapted for instance on each wheel of a farming tractor, bucket loader, or harvester. The same technology could also be used in on-road applications, such as buses or trucks, intended for difficult terrains.

Keywords: permanent magnet synchronous machine, torque, working machine, planetary gearbox



## Acknowledgements

This research work for the doctoral dissertation has been carried out over the years 2012–2016 at Lappeenranta University of Technology, partly financed by the Technology Industries of Finland Centennial Foundation. This financing enabled the key persons from LUT and Saimaa University of Applied Sciences to efficiently combine their knowledge and design a totally new electric traction motor drive system. The key personnel involved were Prof. Juha Pyrhönen, Prof. Jussi Sopenen, Simo Sinkko, M.Sc., and Tommi Nummelin, B.Sc. In addition to these gentlemen, many other important researchers or supporting persons were involved in the practical implementation of the prototype.

I thank all the people involved in the preparation of this doctoral dissertation. Especially, I express my gratitude to Professor Juha Pyrhönen, who has believed in me all the way through my university studies. I am thankful for his endless guidance and funny stories that gave me always a big smile. I also want to thank Dr. Pia Lindh for her support and all the good laughs we have had over the years.

I also express my gratitude to the pre-examiners Professor Wen-Ping Cao and Professor Kurt Stockman for the thorough review work and valuable comments that helped me to significantly improve the quality of this doctoral dissertation.

My very special thanks go to Dr. Janne Nerg, who has greatly increased my knowledge of the thermal analysis of electrical machines. The work of our laboratory staff Antti Suikki, Martti Lindh, Kyösti Tikkanen, Lauri Niinimäki, Markku Niemelä, Kimmo Tolsa, and Jouni Ryhänen is highly appreciated. Thank you for constructing the test setup and making the measurements possible. The work of Dr. Hanna Niemelä for editing the language of this doctoral dissertation is highly appreciated.

The financial support by the Research Foundation of Lappeenranta University of Technology, Emil Aaltonen Foundation, Walter Ahlström Foundation, the Finnish Foundation for Technology Promotion, Henry Ford Foundation, Kaute Foundation, and Ulla Tuominen Foundation is gratefully acknowledged.

I also express my gratitude to all my Finnish colleagues, friends, paratrooper jump team, and especially my loving family for their help and support in this process. I want to thank my family about everything in my life.

Finally, my biggest thanks go to my wife Anita, whose everlasting love gave me the motivation to complete this work. The day we met was the best day in my life, and the days after that have all been full of joy. I love you more today than yesterday but far less than the day after tomorrow. A big thank also goes to our furry family member Walssi, who has reminded me that I must go out for long walks every now and then.

Juho Montonen  
January 2017  
Lappeenranta



*To Anita*

*So it shall be written and so it shall be done!*

(S. Harris: Seventh Son of a Seventh Son, 1988)



# Contents

**Abstract**

**Acknowledgements**

**Contents**

**Nomenclature** **11**

**1 Introduction** **15**

- 1.1 Overview of motor types used in traction applications ..... 16
- 1.2 Requirements of heavy-duty off-road working machines ..... 19
- 1.3 Practical motivation and objectives of the doctoral dissertation ..... 20
- 1.4 Outline of the doctoral dissertation ..... 21
- 1.5 Scientific contributions ..... 22
- 1.6 List of publications ..... 22
- 1.7 Summary of Chapter 1 ..... 24

**2 Permanent magnet synchronous motor with embedded magnets and tooth-coil windings** **25**

- 2.1 Mathematical model of a permanent magnet synchronous machine ..... 25
- 2.2 Electromagnetic design ..... 31
- 2.3 Synchronous inductance and performance analysis ..... 36
- 2.4 Machine loss calculation ..... 38
- 2.5 Control principles of the traction salient pole PMSM ..... 39
  - 2.5.1 Maximum torque per ampere control (MTPA) ..... 39
  - 2.5.2 Field weakening control ..... 40
  - 2.5.3 Maximum torque per volt control (MTPV) ..... 41
- 2.6 Summary of Chapter 2 ..... 42

**3 Integrated solution** **43**

- 3.1 Electromagnetic design ..... 44
  - 3.1.1 Winding configuration ..... 49
- 3.2 Saturation and cross-saturation ..... 54
- 3.3 Torque quality ..... 56
- 3.4 Short-circuit test ..... 58
- 3.5 Control of the prototype machine ..... 61
- 3.6 Mechanical design ..... 61
- 3.7 Thermal design ..... 63
- 3.8 Manufacturing a prototype ..... 69
- 3.9 Summary of Chapter 3 ..... 74

**4 Additional equipment** **75**

- 4.1 Linear electromagnetic actuator ..... 75

4.2 Rotor position sensing.....	78
4.3 Overall system control.....	78
4.4 Summary of Chapter 4 .....	80
<b>5 Measurements</b>	<b>81</b>
5.1 Summary of Chapter 5 .....	86
<b>6 Conclusions</b>	<b>88</b>
6.1 Suggestions for future work .....	90
<b>References</b>	<b>92</b>
<b>Appendix A: Cooling oil datasheet</b>	<b>99</b>

## Nomenclature

### Abbreviations and symbols

$\xi$	wetted surface proportion of the partly immersed rotor	-
$\sigma_{F_{\tan}}$	tangential stress	Pa
$\mu$	dynamic viscosity	Pas
$\mu_0$	permeability of vacuum	Vs/Am
$A$	surface area	m <sup>2</sup>
$B$	flux density	T
$b$	width	m
$c$	constant for the calculation of traction force	-
$d$	lamination sheet thickness	m
$D_s$	air-gap diameter	m
$E$	electric field strength, induced voltage	V/m, V
$e_{PM}$	permanent-magnet-induced voltage	V
$f$	frequency	1/s
$F$	force	N
$G$	conductance	1/Ω
$g$	gravitational constant	m/s <sup>2</sup>
$h$	height	m
$I$	current	A, RMS
$i_s$	stator current	A
$i_{sd}$	current along the d-axis	A
$i_{sq}$	current along the q-axis	A
$i_x$	characteristic current	A
$J$	current density	A/mm <sup>2</sup>
$k_2$	factor for slot leakage calculation in double-layer windings	-
$k_{Cu}$	slot copper space factor	-
$k_e$	excess loss constant	-
$k_{Fe}$	iron space factor	-
$k_h$	hysteresis loss constant	-
$k_w$	winding factor	-
$k_{wp}$	winding factor of the operational harmonic	-
$k_{wv}$	winding factor of the $v^{\text{th}}$ harmonic	-
$l$	length	m
$L_{ew}$	end-winding leakage inductance	H
$L_m$	magnetizing inductance	H
$L_{md}$	magnetizing inductance along the d-axis	H
$L_{mq}$	magnetizing inductance along the q-axis	H
$L_s$	synchronous inductance	H
$L_{sd}$	synchronous inductance along the d-axis	H

---

$L_{sq}$	synchronous inductance along the q-axis, skew leakage inductance	H
$L_{s\sigma}$	stator leakage inductance	H
$L_{tt}$	tooth tip leakage inductance	H
$L_u$	slot leakage inductance	H
$l_w$	winding length	m
$L_\delta$	air-gap leakage inductance	H
$m$	number of phases, mass	-, kg
$n_{par}$	number of parallel branches	-
$N_s$	number of coil turns in phase	-
$p$	number of pole pairs	-
$P$	power, losses	W
$P_{Cu}$	copper losses, Joule losses	W
$P_{Eddy}$	eddy current losses	W
$P_{Exc}$	excess losses	W
$P_{Fe}$	iron losses	W
$P_{Hyst}$	hysteresis losses	W
$Q$	charge	C
$q$	number of slots per pole and phase	-
$Q_s$	number of stator slots	-
$r_1$	outer radius	m
$r_2$	inner radius	m
$r_{Cu}$	radius of copper wire	m
$R_s$	stator phase winding resistance	$\Omega$
$S_{Cus}$	slot copper area	$m^2$
$S_r$	rotor area	$m^2$
$T$	electromagnetic torque, temperature	Nm, °C, K
$t$	time	s
$T_{oil}$	oil friction torque	Nm
$u_s$	stator voltage	V, RMS
$u_{sd}$	voltage along the d-axis	A
$u_{sq}$	voltage along the q-axis	A
$v$	velocity	m/s
$z_Q$	number of conductors around tooth	-
$\alpha$	convection coefficient	W/( $m^2K$ )
$\gamma$	current angle	rad, °
$\delta$	air gap, load angle	m, rad, °
$\delta_e$	effective air gap	m
$\lambda$	thermal conductivity	W/(mK)
$\lambda_{ew}$	end-winding leakage permeance factor	-
$\lambda_{tt}$	tooth tip leakage permeance factor	-
$\lambda_u$	slot leakage permeance factor	-
$\nu$	harmonic order	-
$\sigma$	conductivity	S/m
$\sigma_{sq}$	skew leakage factor	-

---

$\sigma_\delta$	air-gap leakage factor	-
$\varphi$	phase shift angle	rad, °
$\Psi_{PM}$	permanent magnet flux linkage	Vs
$\Psi_s$	stator flux linkage	Vs
$\Omega$	mechanical angular frequency	rad/s
$\omega_s$	electric angular frequency	rad/s
$l'$	effective core length	m

### Subscripts

a	axial
Cu	copper
d	direct axis
e	effective
ew	end winding
Fe	iron
m	magnetizing
par	parallel
ph	phase
PM	permanent magnet
q	quadrature axis
r	radial
r	rotor
s	stator, synchronous
sq	skew
$\sigma$	stator leakage
tt	tooth tip
u	slot
wp	fundamental harmonic
wv	$v^{\text{th}}$ harmonic
$\delta$	air gap

### Abbreviations

AC	Alternating current
BLDC	Brushless direct current machine
DC	Direct current
DTC	Direct torque control
EESM	Electrically excited synchronous machine
FEA	Finite element analysis
FEM	Finite element method
FW	Field weakening
HEV	Hybrid electric vehicle
ICE	Internal combustion engine

IM	Induction machine
LCM	Least common multiple
LPTN	Lumped-parameter thermal network
MTPA	Maximum torque per ampere
MTPV	Maximum torque per volt
NdFeB	Neodymium iron boron
p.u.	per unit
PM	Permanent magnet
PMaSynRM	Permanent magnet assisted synchronous reluctance machine
PMSM	Permanent magnet synchronous machine
QF	Quality factor
SRM	Switched reluctance machine
SynRM	Synchronous reluctance machine
TCPMSM	Tooth-coil permanent magnet synchronous machine
THD	Total harmonic distortion

## 1 Introduction

The growing demands for high energy efficiency and reduction of emissions are driving to increase the use of renewable energy sources. Emissions reduction is a high-priority issue, and improvements in different kinds of traction applications play a key role in it. Traction applications are one of the main sources of air pollution and a major consumer of fossil energy resources (Saber and Venayagamoorthy 2011). Furthermore, because of the increasing oil price, the development of traction applications is heading towards cleaner propulsion with electric machines in vehicles and working machines (Emadi et al. 2008). As the electric machine has a high efficiency (usually around 85–95 % at power levels used in small electric vehicles such as passenger cars), the energy consumption can be significantly decreased compared with vehicles powered by an internal combustion engine (ICE) alone, which has its practical peak efficiency around 40 % (Lukic and Emadi 2004). These benefits have led to the development of various hybrid electric vehicles (HEVs), fuel cell vehicles, and full electric vehicles.

Considering fuel savings, the field of heavy off-road working machines seems to offer the most promising opportunities. Previous works such as (Immonen 2013) promise savings of up to 40–50 % in fuel consumption; the results have been obtained by simulations, in which the model has been compared with an actual working cycle published by a working machine manufacturer. These prospects are also supported by the fact that manufacturers are launching their hybridized machines in the market.

The electrical machine provides significant improvements to the use of HEVs or hybrid working machines, as the ICEs in such applications are largely overdimensioned from the average power point of view (Zeraoulia et al. 2006), (Montonen et al. 2016) Usually, an ICE is designed according to its peak power, which is needed only occasionally, and less attention is paid to the time for which the very high performance is actually required (Montonen et al. 2012). Electrical machines can be designed using the measured driving cycle or a duty cycle based on the average power with its negative and positive peaks. Hence, according to the driving cycle, the electrical machine and other components of the HEV or the hybrid working machine can be selected based on the average power. Consequently, the size of the ICE can be significantly reduced, and it can be used mainly in its optimal point. This means that with the help of hybridization, the size of the ICE can be reduced by half or even more from its original size.

The price of oil has significantly increased after the oil crisis in the 1970s. However, the oil price also seems to be highly dependent on the global economic and political situation. At the moment, the oil price is historically low, which naturally has some adverse effects on the development of new energy-saving technologies. It is, however, generally believed that the role of electric systems in vehicles will significantly increase in the future.

In many cases, a hybrid system has great potential to improve energy efficiency and thereby reduce emissions. It remains to be seen which driver will be stronger, the price of oil or the price of emissions.

## 1.1 Overview of motor types used in traction applications

In principle, all electrical machine types available can be used in traction applications (Boldea et al. 2014), (Zeraoulia et al. 2006), (De Santiago et al. 2012), (Finken et al. 2008). Electrical rotating machines can be divided into machines, which either have a mechanical commutator or not. The only machines that have a commutator are traditional direct current (DC) machines. Machines without a commutator, again, are alternating current (AC) machines or some special machines, such as switched reluctance machines or brushless DC machines, which have a permanent magnet (PM) rotor and resemble permanent magnet synchronous machines by construction. All the types of electrical rotating-field machines that can be used in traction applications are shown in Fig. 1.1. The brushless DC machine (BLDC) is given a branch of its own. In practice, a PMSM and a BLDC may be similar, and it is only the control principle that determines the group to which a machine belongs.

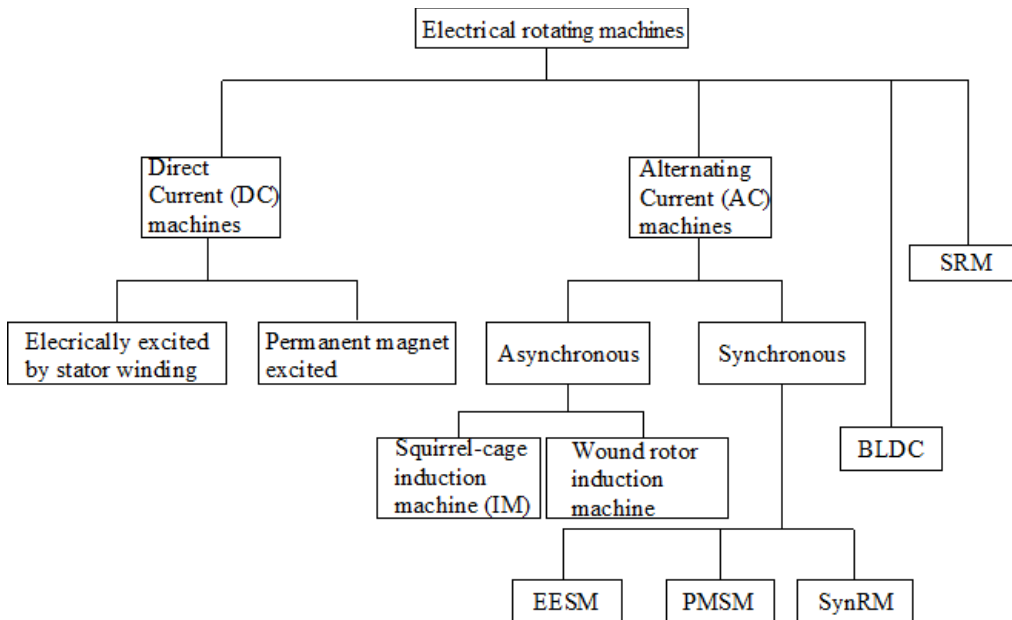


Fig. 1.1. Family of electrical rotating machines used in traction applications. EESM: electrically excited synchronous machine, PMSM: permanent magnet synchronous machine, SynRM: synchronous reluctance machine, BLDC: brushless DC machine, and SRM: switched reluctance machine (adapted from Pyrhönen et al. 2014).

The most common AC industrial machine type in the world is the asynchronous squirrel-cage induction machine, which thus represents the most mature technology and has the lowest production costs (Pellegrino et al. 2012). The induction machine (IM) provides high torque to meet the demands for hill climbing or acceleration; however, its constant power speed range (CPSR) is narrow as IMs usually can reach a maximum rotational

speed of two to three times the base speed. The constant power range of IMs is limited by the torque-producing capability in the field weakening. The control methods of induction machines are commonly known, but their accurate control is difficult in the vicinity of zero speed. The problem with IMs is that they always need a gear because IMs are mainly used in higher-speed applications owing to their low number of applicable pole pairs. This can be explained by the fact that the power factor of an IM is the lower, the higher is the number of poles; the magnetizing inductance is inversely proportional to the square of the number of pole pairs.

Even though IMs are widely used in traction applications because of their advantageous characteristics and low manufacturing costs, the trend in traction applications is to use different variations of PMSM (Wang et al. 2011), (Reddy et al. 2012) (Galioto et al. 2015), (Dorrel et al. 2011) which have numerous beneficial features for this purpose. PMSMs can produce high torque at low speeds and have high efficiency and power capability over a wide speed range. PMSMs also have the least limitations on machine dimensions compared with the other machine types. Furthermore, they have good properties to operate in a direct drive system without gear/transmission (Rilla 2012). Maintenance of brushes or slip rings is not needed, because they are not applied in the PMSMs. The drawback of a PMSM is the high price of the PM material, especially, if high-remanence rare-earth permanent magnets are used (Petrov 2015). Moreover, difficulties related to the use of field weakening may somewhat limit the use of PMSMs. However, PMSMs have more advantages than disadvantages, and they have the most promising future to be used as traction machines.

The synchronous reluctance machine (SynRM) uses the reluctance torque in its torque production. Reluctance torque is based on the inductance difference of the rotor (Haataja 2003). The SynRM is an AC machine, which has sinusoidally distributed windings in the stator like every other AC machine. This machine type has not been widely used in traction applications because of its low peak torque and low power density. However, its characteristics can be significantly enhanced by using permanent magnets in the rotor. In that case, the machine is called a permanent-magnet-assisted synchronous reluctance machine (PMSynRM), which produces torque as a result of rotor asymmetry; the main torque component and the torque produced by the PMs thus inherently improve the torque quality and power factor of the machine. Further, the SynRM is an inexpensive and simple rotor construction. Nevertheless, the integration of magnets into the rotor core makes it more expensive depending on the amount and type of the magnets used. Further, the SynRM has high efficiency, and for example Asea Brown Boveri (ABB) is starting the manufacturing of SynRMs for industrial uses. The use of PMSynRMs in variable-speed applications such as traction has been studied extensively for instance by (Guglielmi et al. 2013), (Bianchi et al. 2014), and (Barcaro et al. 2012).

The switched reluctance machine (SRM) was introduced in 1838 (Miller 1993). Despite its long history, the machine has not found its place in the industry. The SRM is a completely different machine than the synchronous reluctance machine, even though its torque production is also based on the anisotropy of the rotor. The SRM has salient poles

both in the stator and the rotor and tooth-coil windings in the stator (Miller 2002). The SRM requires intelligent power electronics, which explains why it was not commonly used in its early days. The manufacturing costs of SRMs are low because the rotor does not need permanent magnets or windings as it is made from iron laminations. The SRM has good fault tolerance, and because of its simple rotor construction, it withstands high temperatures (Bilgin et al. 2012). The SRM has efficiency and power density comparable with those of the IM. The disadvantages of the SRM are the high noise caused by the sequential excitation of the stator poles and difficulties to control the machine. The torque quality of the SRM is also poor compared for instance with that of the IM. Moreover, the magnetic circuit of the SRM is very highly saturated, which makes the electromagnetic modelling of the machine difficult without a finite element analysis (Wu et al. 2003).

Traditional electrically excited synchronous machines (EESM) have not been widely used in EVs even though they are capable of adjusting their magnetizing flux density in the air gap, thereby having good field-weakening capacity. Regulation of the magnetic flux linkage leads even to the fact that the EESM can reach very high-speed operation because of the flux linkage control. The EESM usually has good efficiency and also simple control. A disadvantage of the EESM is that the slip rings and brushes require maintenance. A further problem with small EESMs is the additional rotor copper losses, which significantly degrade the machine efficiency. Nowadays, hybrid excitation machines have gained interest. In these machines, the advantageous properties of EESM and PMSM are combined (Di Barba et al. 2015), (Kamiev 2013).

The brushless DC motor has PMs on the rotor surface, and it works like the AC PMSM but with a trapezoidal back-electromotive force (EMF). In the AC PMSM, the back-EMF is, in principle, sinusoidal. A well-designed BLDC machine drive has a high torque density and a low torque ripple. A basic BLDC machine has integral slot windings in the stator with two slots per pole and phase, and it has been used in traction applications (Miller 1989).

The use of DC machines is not uncommon in EVs either. It has a simple manufacture, robust control, and relatively high reliability. It is also inexpensive and does not need complicated power electronics for connection to the battery; a simple four-quadrant PWM chopper suffices for the purpose. Position or speed sensors are not needed in DC machines. A separately excited DC machine can be magnetized in two ways: either by electrical excitation by the stator winding or by permanent magnets in the stator. The disadvantages of the DC machine are maintenance of the brushes, wear of the commutator, low power density, and low efficiency compared with AC machines. The simplicity of the electrical drive is perhaps the key factor why the DC machine has been used in EVs.

In traction applications, a high low-speed torque and a wide field weakening area are emphasized. In most cases, an electric machine needs a gear to adapt the motor speed to the traction wheel speed. In particular, working machines may need a very high torque at

---

the start, and therefore, combining an electrical machine with a gear is an important aspect.

## 1.2 Requirements of heavy-duty off-road working machines

Heavy off-road working machines have to be capable of operating both at a high speed with a low torque and at a high torque with a low speed. A typical example is an agricultural tractor used for instance both for cultivating or ploughing at low speeds and very high torques, and on road for transporting light loads up to 50 km/h speeds.

The masses of tractors vary from several thousands of kilograms to tens of thousands of kilograms. Let us consider a 9000 kg 4×4 farming tractor, which is a common tractor in large-scale farming. The traction force for instance in a dry clay field can be calculated by

$$F = cmg, \quad (1.1)$$

where  $c$  is the difference of the circumferential force factor and the rolling resistance factor,  $m$  is the tractor efficient mass, and  $g$  is the gravitational constant. Traction power can be calculated by knowing the velocity  $v$  at which the tractor is moving in a dry clay field by equation

$$P = Fv. \quad (1.2)$$

If the velocity is 2 m/s and the traction force 31 kN (Ahokas 2013), the required traction power is 62 kW. This serves as a guideline on the prototype design, as the motor power must normally be 1.5–2 times the traction power. Naturally, the gear ratio must also be in a correct range. Thus, a tractor could be equipped with four of the electrical motors presented in this dissertation.

Typical speed ratios may vary in the range of 1:20 or even 1:30. Traditionally, in the ICE traction, the engine power is delivered to the wheels through a mechanical drive train providing a plurality of gear ratios, which ensures, in principle, a constant power drive for the whole speed range. Figure 1.2 illustrates the principle of an ICE drive with a six-step gear. The torque-producing capability of a typical electrical machine with its constant flux and field weakening ranges is shown for comparison.

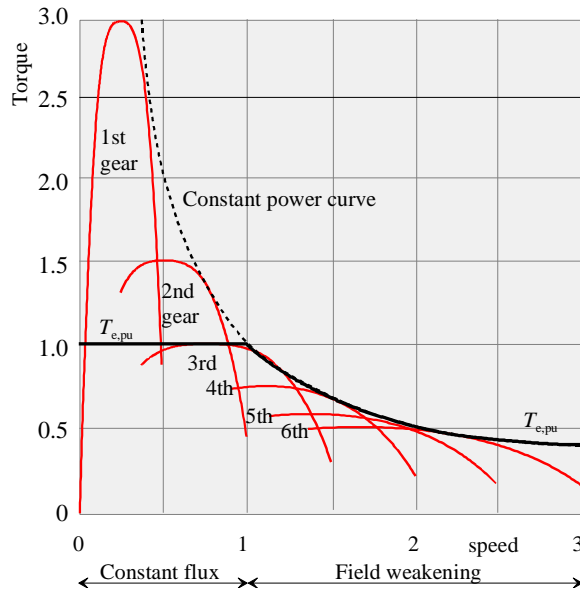


Fig. 1.2. Internal combustion engine with a six-step-gear. The torque envelope curve follows a constant per-unit power  $P = 1$ . The  $T_e$  curve illustrates the typical constant torque-producing capability of an electrical machine as a function of speed when the rated per-unit power and speed are  $T_e = 1$  and  $\Omega = 1$ .

As Figure 1.2 shows, at low speeds, the competition between the ICE and the electrical motor is tough for the electrical machine as the help of a shiftable gear is missing. However, contrary to the ICE, the electrical machine has high overloadability if only the motor winding and insulation temperatures remain at an acceptable level. In fact, in on-road applications, an electric motor can compete with the ICE gearbox curve as the overloading at low speeds is intermittent. However, if we consider an off-road application, the torque and speed ranges illustrated in Figure 1.2 are far from adequate. The per-unit starting torque 3 must be multiplied for instance by a factor of four to achieve a torque range of  $12:0.5 = 24:1$  for the whole operating range.

In principle, we have three alternatives to reach such a torque-speed range: 1) We need a high-speed electric machine and a high-gear-ratio reduction gear to adjust the wheel speed, 2) we need a large electric machine that can produce the starting torque needed and can go deep in the field weakening, or 3) we need to integrate a normal-speed-range electric motor with a gearbox. In Chapter 2, these three options are studied from the viewpoint of a PMSM.

### 1.3 Practical motivation and objectives of the doctoral dissertation

The motivation of this doctoral dissertation was to define the boundaries of electrical drives in very heavy traction applications and to determine the best possible integrated

design for a heavy off-road machine traction. The focus is on the integration of a shiftable planetary gear and a permanent magnet motor into a compact form. In the dissertation, a combination of oil-immersion, oil-dropping, and oil-splashing cooling is studied. The gear change mechanism is designed because of the lack of commercially available components. A totally new mechanical way to construct the rotor is tested.

According to a market analysis made in the project, the proposed integrated motor-gear design was identified to have remarkable business potential. This motivated the work to establish a superior electric motor drive system so that the product could also be ready for sale.

#### 1.4 Outline of the doctoral dissertation

This doctoral dissertation studies the design of a traction motor combining a tooth-coil-wound permanent magnet electrical machine and a two-step planetary gearbox into a very compact package. The design is intended to be used especially in off-road hybrid working machines.

The structure and contributions of this dissertation are summarized as follows:

**Chapter 1** introduces the research topic of the doctoral dissertation. The study starts with a short presentation of different electrical motors and their benefits and drawbacks in relation to electric traction. The chapter presents the outline and motivation of the work. Finally, the chapter provides the scientific contributions of the dissertation and lists the author's most important publications relevant to the dissertation.

**Chapter 2** gives design guidelines for the electrical machine and shows the theory of the permanent magnet synchronous machine with tooth-coil windings and embedded magnets.

**Chapter 3** presents the design process of the prototype machine. The machine structure is described in detail, and a performance analysis is made by analytical methods and a finite element method.

**Chapter 4** addresses the design of the linear magnetic actuator and provides the details of the gear changing control system.

**Chapter 5** introduces the measurement setup and verifies the calculated results by tests in the laboratory.

**Chapter 6** draws conclusions on the work, discusses the key contributions of the work, and identifies topics of future work.

## 1.5 Scientific contributions

The main scientific contribution of the doctoral dissertation is a systematic and multidisciplinary analysis of the design of an integrated traction system. The main part of the work provides a thorough analysis of the properties and performance of an 18-tooth-coil 14-pole permanent-magnet synchronous machine, which, despite its good properties, has received limited attention in the literature. A comparison of various 18-slot tooth-coil machines is performed, and a cost factor is developed to select the most appropriate stator-tooth-rotor-pole combination for a certain traction drive.

One of the important properties of a traction motor is that its cross-saturation behaviour is at an acceptable level. Therefore, the cross-saturation properties of an 18/14 machine were investigated. It was found that the cross-saturation phenomenon does not degrade the machine torque and flux linkages as severely as in other 18-slot machines under study. This is due to the large difference between the numbers of rotor poles and stator slots.

The benefits and advantages of the traditionally harmful leakage terms in the design of traction motors are shown. In traction motors, the stator leakage must be selected according to the needs of the drive system.

The performance of the designed motor was validated by a virtual simulator. The need for gear change was clearly demonstrated. The study also gives guidelines and emphasizes the importance of the combined design of mechanical, thermal, and electromagnetic design of the traction motor. The dissertation also proposes a method for evaluating the dimensions of an electric traction motor.

In the course of the doctoral study, also a linear magnetic actuator that allows a rotating shaft was designed for a gear change application.

## 1.6 List of publications

Some of the results of the doctoral dissertation are published in the following papers:

1. Journal articles

- Kamiev K., Montonen J., Ragawendra M. P., Pyrhönen J., Tapia J., and Niemelä M., “Design Principles of Permanent Magnet Synchronous Machines for Parallel Hybrid and Traction Applications,” *IEEE Transaction on Industrial Electronics*, vol. 60, no. 11, 2013, pp. 4881–4890.
- Montonen J. and Pyrhönen J., “Performance Analysis of Tooth-Coil Permanent Magnet Traction Motors with Embedded Magnets and Saliency,” *International Review on Electrical Engineering*, vol. 11, no. 1, 2016, pp. 9–19.
- Lindh P., Montonen J., Immonen P., Pyrhönen J., Tapia J., “Design of a Traction Motor with Tooth-Coil Windings and Embedded Magnets,” *IEEE Transactions on Industrial Electronics*, vol. 61 no. 8, August, 2014, pp. 4306–4314.

- Montonen J., Nokka J., Pyrhönen J., “Virtual Wheel Loader Simulation – Defining the Performance of Drive-Train Components,” *International Review on Modeling and Simulation*, vol. 9, no. 3, 2016, pp. 208–216.
- Montonen J., Nerg J., Pyrhönen J., “Torque Analysis of Tooth-Coil Wound Permanent Magnet Machines with Embedded Magnets Considering Cross Saturation,” *International Review on Electrical Engineering*, vol. 11, no. 1, 2016
- Montonen J., Nerg J., Sinkko S., Nummelin T., Lindh P., and Pyrhönen J., “Designing an Integrated-Gear Traction Motor for Off-Road Applications,” in review.

## 2. Conference papers

- Montonen J., Montonen J.-H., Immonen P., Murashko K., Ponomarev P., Lindh T., Lindh P., Laurila L., Pyrhönen J., Tarkiainen A., and Rouvinen A., “Electric Drive Dimensioning for a Hybrid Working Machine by Using Virtual Prototyping,” in *Proc. of the 20th International Conference on Electrical Machines (ICEM)*, Marseille, France, 2–5 September 2012, pp. 921–927.
- Montonen J., Lindh P., and Pyrhönen J., “Design Process of Traction Motor having Tooth-Coil Windings,” in *Proc. of the 20th International Conference on Electrical Machines (ICEM)*, Marseille, France, 2–5 September 2012, pp. 1264–1268.
- Sinkko S., Montonen J., Gerami Tehrani M., Pyrhönen J., Sopanen J., and Nummelin T., “Integrated Hub-Motor Drive Train for Off-Road Vehicles,” in *Proc. EPE’14 ECCE*, Lappeenranta, Finland, 26–28 August 2014.
- Montonen J., Sinkko S., Lindh P., and Pyrhönen J., “Design of a Traction Motor with Two-Step Gearbox for High-Torque Applications,” in *Proc. of the 21th International Conference on Electrical Machines (ICEM)*, Berlin, Germany, 2–5 September 2014, pp. 1069–1075.
- Montonen J., Lindh P., Pyrhönen J., “Impact of Slot Key in the Performance of Tooth-Coil Traction Motor,” in *Proc. EPE’15 ECCE*, Geneva, Switzerland, 8–10 September 2015, pp. 1–8.

The results of the work have led to the following patent application:

Montonen J., Sinkko S., Nummelin T., Pyrhönen J., “A magnetic actuator and a gear system comprising the same,” European patent application no. 15183901.6

This patent application is related to a new actuator for gear shifting.

Other papers published with the author's partial contribution during the writing period of this doctoral dissertation are listed below:

- P. Lindh, Y. Alexandrova, J. Pyrhönen, and J. Montonen, "Design Process of Traction Motor for Hybrid Bus Applications," in *the 14<sup>th</sup> International Symposium "Topical Problems in the Field of Electrical and Power Engineering"* 13–18 January 2014, Pärnu, Estonia.
- Ahonen T., Tamminen J., and Montonen J., "Comparison of electric motor types for realizing an energy efficient pumping system," in *Proc. EPE'14 ECCE*, Lappeenranta, Finland, 26–28 August 2014.
- Repo A.-K., Montonen, J., Sizonenko V., Saransaari P., Lindh P., and Pyrhönen J., "Energy Efficiency of Induction Motors in Crane Applications," in *the 21<sup>th</sup> International Conference on Electrical Machines (ICEM)*, Berlin, Germany, 2–9 September 2014.
- Pyrhönen J., Montonen J., Lindh P., Vauterin J., and Otto M., "Replacing Copper with New Carbon Nanomaterials in Electrical Machine Windings," *International Review on Electrical Engineering*, vol. 10, no. 1, 2015, pp. 12–21.
- Pyrhönen J., Vauterin J., Montonen J., and Lindh P., "At the Cusp of the Next Electric Motor Revolution: Replacing Copper with Carbon Nanomaterials," in *Proc. EEMODS 2015*, Helsinki, Finland, 15–17 September 2015.

The integrated motor gear system is also described in the patent application:

Sinkko, S., Nummelin, T., Suuronen, A., Pyrhönen, J., "An Electrical Motor Construction Provided with a Planetary Gear System," US Patent US2016201763 (A1)

## 1.7 Summary of Chapter 1

The speed and torque requirements for driving heavy-duty off-road machinery were addressed. Some societal aspects with respect to electrically driven machinery were discussed. Starting from these considerations, the research objectives were formulated as 1) definition of the boundaries of electrical drives for off-road heavy duty machines, 2) integration of a shiftable planetary gearbox and a PMSM in order to have a very compact design, and 3) design of a gear change mechanism. The scientific contributions were listed and the author's publication list was given.

---

## 2 Permanent magnet synchronous motor with embedded magnets and tooth-coil windings

The traditional electric machine design relies largely on experimental knowledge about machine parameters based on data gathered from actual machines. Thermal performance characteristics of the machine can be determined with certain guidelines such as cooling arrangement, machine type, and size. The data given in machine design textbooks are normally based on continuous-duty industrial machines. However, the loading of traction machines may vary so much that traditional design rules may not be applicable.

Therefore, with permanent magnet traction machines, different design criteria and an additional set of design tools is required. Analytical equations provide relatively accurate and reliable knowledge of the parameters of the electrical machine. However, they assume that the parameters remain constant. This will result in some inaccuracies because of the nonlinear properties of iron; analytically, these inaccuracies are difficult to consider in detail. The finite element analysis (FEA) offers a solution to this problem; a static FEA takes into account the nonlinear effects in iron, and by the FEA it is possible to solve the flux linkage surfaces for the machine. Then, a loss analysis must be performed with the time-stepping transient analysis.

Accurate knowledge of the machine thermal behaviour is needed in the performance analysis because of the nature of the neodymium-iron-boron PM material and varying load conditions. In varying load conditions, the machine thermal behaviour can be estimated by a transient lumped-parameter thermal model. The use of the model requires knowledge of the power loss generation inside the machine based on the measurements or finite element analysis and understanding of the heat transfer mechanisms.

This chapter presents an analysis and guidelines of the electrical dimensioning of a tooth-coil (concentrated fractional slot non-overlapping) -wound permanent magnet traction machine with embedded magnets. A brief introduction to control strategy and evaluation of loss distribution in electrical machines is also given.

### 2.1 Mathematical model of a permanent magnet synchronous machine

The interior PM machine produces excitation torque caused by the PM interaction with the quadrature-axis current and reluctance torque enabled by the rotor saliency. The reluctance torque component can significantly improve the torque capability, especially below the rated speed. In principle, a rotor surface magnet machine does not have inductance difference at all, and therefore, there is no reluctance torque available (Pellegrino et al. 2012). The field weakening can be difficult with such a machine, and the current available must be used to produce a negative d-axis current component, which does not produce torque with rotor surface magnet machines.

The vector diagram of the salient pole PMSM is presented in Fig. 2.1. The following analysis is made for per-unit (p.u.) quantities. The equations of PMSM are defined directly by using this vector diagram.

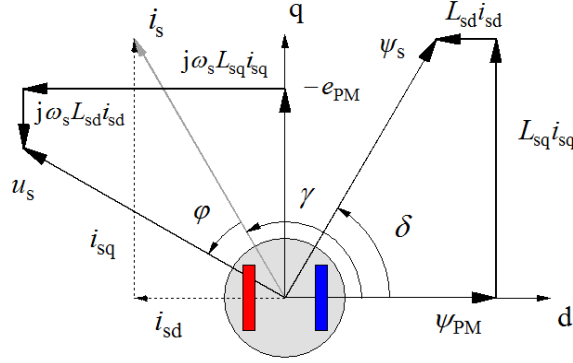


Fig. 2.1. Vector diagram to illustrate the mathematical model of the PMSM.  $\gamma$  is the angle between the d-axis and the current vector (current vector angle),  $\delta$  is the load angle,  $\varphi$  is the phase shift angle,  $i_{sd}$  and  $i_{sq}$  are the d- and q-axis currents, respectively,  $i_s$  is the stator current,  $u_s$  is the stator voltage,  $e_{PM}$  is the permanent-magnet-induced voltage,  $\psi_{PM}$  and  $\psi_s$  are the permanent magnet flux linkage and the stator flux linkage, respectively,  $L_{sd}$  and  $L_{sq}$  are the d- and q-axis synchronous inductance components, and  $\omega_s$  is the stator angular frequency. Stator resistance  $R_s$  is zero in this case.

The torque and power of a permanent magnet machine can be written using the cross-field principle as

$$T = \psi_{PM} i_{sq} + (L_{sd} - L_{sq}) i_{sd} i_{sq}, \quad (2.1)$$

$$P = \Omega (\psi_{PM} i_{sq} + (L_{sd} - L_{sq}) i_{sd} i_{sq}). \quad (2.2)$$

The dq axis voltage equations are

$$u_{sd} = R_s i_{sd} - \omega_s L_{sq} i_{sq}, \quad (2.3)$$

$$u_{sq} = R_s i_{sq} + \omega_s \psi_{PM} + \omega_s L_{sd} i_{sd}, \quad (2.4)$$

where

$i_{sd}, i_{sq}$	d- and q-axis stator currents,
$u_{sd}, u_{sq}$	d- and q-axis stator voltages,
$L_{sd}, L_{sq}$	d- and q-axis synchronous inductances,
$\psi_{PM}$	flux linkage caused by permanent magnet excitation,
$R_s$	stator resistance,
$P$	output power,
$T$	electromagnetic torque,
$\Omega$	mechanical angular velocity, and
$\omega_s$	electrical angular frequency.

The stator current components can be written as

$$i_{sd} = i_s \cos \gamma , \quad (2.5)$$

$$i_{sq} = i_s \sin \gamma . \quad (2.6)$$

Now, we return to the three different options to solve the problem of propulsion in an off-road heavy-duty working machine. The options are 1) a high-speed electric machine and a high-gear-ratio reduction gear to adjust the wheel speed, 2) a large electric machine that can produce the starting torque needed and that can go deep into the field weakening, or 3) integration of a normal speed range electric motor with a gearbox.

A PMSM can be designed to operate in a wide speed range by selecting its per-unit characteristic current  $i_{x,pu}$  depending on the permanent magnet flux linkage  $\psi_{PM,pu}$  and the synchronous inductance  $L_{s,pu}$  close to unity

$$i_{x,pu} = \frac{\psi_{PM,pu}}{L_{s,pu}} . \quad (2.7)$$

If  $i_x = 1$ , the theoretical speed range of the machine is infinite as its stator flux linkage can be driven to zero with the rated current. In practice, the mechanics does not allow that. In principle, such a motor should be capable of meeting the targets of cases 1) and 2). Despite this kind of selection, the practical solution might have difficulties in providing the required practical torque range.

If the synchronous inductance per-unit value  $L_{s,pu}$  of a PMSM is selected high, the motor can be overloaded only at the lowest speeds, and its torque capabilities already at moderate speeds close to the rated speed are limited based on the load angle  $\delta$  equation and the voltage limit

$$P_{pu} = \frac{e_{PM,pu} u_{s,pu}}{\omega_{s,pu} L_{s,pu}} \sin \delta , \quad (2.8)$$

where  $e_{PM,pu}$  is the permanent-magnet-induced voltage,  $u_{s,pu}$  is the supply voltage, and  $\omega_{s,pu}$  is the angular frequency per-unit value. With high  $L_{s,pu}$ , the field weakening starts well before the rated voltage no-load speed if  $\psi_{PM,pu} = 1$ .

The synchronous inductances consist of the magnetizing inductance  $L_{m,dq}$  and the stator leakage inductance  $L_{s\sigma}$

$$L_{s,dq} = L_{s\sigma} + L_{m,dq} . \quad (2.9)$$

If the magnetizing inductance is large, the machine is prone to armature-reaction-caused

saturation unless a significant negative d-axis current  $i_d$  is used. If the machine does not have saliency, the maximum torque per ampere is reached with  $i_d = 0$ . In such a case, the absolute value of air-gap flux linkage increases as a function of q-axis current

$$\psi_m = \sqrt{\psi_{PM}^2 + (i_q L_{mq})^2}. \quad (2.10)$$

If we assume a typical distributed winding machine case for instance with  $\psi_{PM,pu} = 1$ ,  $L_{md,pu} = 0.7$ , and  $L_{s,pu} = 0.85$  and neglect saturation, the air-gap flux linkage increases even to  $\psi_{m,pu} = 1.72$  and  $\psi_{s,pu} = 1.97$  with  $i_{q,pu} = 2$  in initial acceleration. The field weakening of this drive starts at 51 % of the no-load speed. Such a flux linkage value would inevitably saturate the machine, and in reality, the increase in the air-gap flux linkage remains clearly lower. Nevertheless, the motor speed range with a high current should be limited. At the speed  $\Omega_{pu} = 3$ , the stator flux linkage at no load should only be  $\psi_{s0,pu} \approx 0.2$  to leave space for the q-axis armature reaction and to keep  $\psi_{s,pu} = 0.33$  under the rated load. Thus, we need the demagnetizing current

$$i_{d,pu} = -\frac{\psi_{PM,pu} - \psi_{s0,pu}}{L_{d,pu}} = 0.941. \quad (2.11)$$

The current reserve for the torque producing current should be

$$i_{q,pu} = \sqrt{1 - i_{d,pu}^2} = 0.338, \quad (2.12)$$

which is just enough to produce the torque  $T_{e,pu} = 0.33$  for the rated power at  $\Omega_{pu} = 3$ . This example shows that a normal PMSM should be close to its limits to produce a torque range of 6:1 (2:0.33) within its speed range from 0 to 3 per unit. If the motor can be temporarily overloaded up to  $T_{e,pu} = 3$  at the lowest speeds, we can increase the torque range to 9:1. This is still far from the desired torque range needed for heavy off-road machines as it was shown in the introduction.

The problems related to the above example are obviously the very high armature-reaction-caused saturation, high Joule losses at low speeds, and difficulties to reach the required top speed. There also seems to be a need to increase the synchronous inductance further and change the ratio of magnetizing inductance and leakage inductance. A tooth-coil PMSM might provide a solution.

In TCPMSMs, the leakage inductance  $L_{s\sigma}$  may be significantly larger than the magnetizing inductance  $L_m$ . In such a case, saturation is not as obvious as in the integral slot winding PMSMs discussed above. Therefore, in a traction machine with a wide speed range, the synchronous inductance should preferably consist mainly of leakage inductance that does not saturate the main flux magnetic circuit. Among different motor types, a tooth-coil PMSM should thus be preferred (Finken et al. 2008), (Nerg et al. 2014),

and (El-Refaie 2010).

A suitable TCPMSM can meet the demands of typical electric vehicle traction but may be in difficulties with the torque-speed demands of heavy working machine load cycles. This machine type offers several alternatives to tune the ratio of the leakage inductance and the magnetizing inductance to reach a favourable field weakening range (Montonen and Pyrhönen 2016). Table 2.1 shows that there are alternatives in which the air-gap leakage inductance

$$L_{\delta} = \sigma_{\delta} L_m \quad (2.13)$$

can be small or even tens of times the magnetizing inductance. In tooth-coil machines the air-gap leakage is the dominating part of leakage inductance.

The leakage inductance components have previously been analysed analytically for instance by (Ponomarev 2013), (Ponomarev et al. 2013), and (Pyrhönen et al. 2008). The equations are given below. The leakage inductance is the sum of the air gap  $L_{\delta}$ , the end-winding  $L_{ew}$ , the slot  $L_u$ , the tooth-tip  $L_{tt}$ , and the skew leakage  $L_{sq}$

$$L_{st} = L_{\delta} + L_{ew} + L_u + L_{tt} + L_{sq}, \quad (2.14)$$

where

$$L_{\delta} = \sigma_{\delta} L_m = \sum_{\substack{\nu=1 \\ \nu \neq p}}^{\nu=\infty} \left( p \frac{k_{w\nu}}{\nu k_{wp}} \right)^2 L_m, \quad (2.15)$$

$$L_{ew} = \frac{4m}{Q_s} \mu_0 q l_w N_s^2 \lambda_{ew}, \quad (2.16)$$

$$L_u = \frac{4m}{Q_s} \mu_0 l' N_s^2 \lambda_u, \quad (2.17)$$

$$L_{tt} = \frac{4m}{Q_s} \mu_0 l' N_s^2 k_2 \lambda_{tt}, \quad (2.18)$$

$$L_{sq} = \sigma_{sq} L_m, \quad (2.19)$$

where  $\sigma_{\delta}$  is the air-gap leakage factor,  $k_{w\nu}$  is the winding factor of the  $\nu^{\text{th}}$  spatial harmonic,  $k_{wp}$  is the winding factor of the operating harmonic,  $Q_s$  is the number of stator slots,  $q$  is the number of slots per pole and phase,  $l_w$  is the end winding length,  $\lambda_{ew}$  is the end-winding

leakage permeance factor,  $\lambda_u$  is the slot leakage permeance factor,  $\lambda_{tt}$  is the tooth tip leakage permeance factor,  $k_2$  is the factor that takes into account the presence of different phases in a same slot, and  $\sigma_{sq}$  is the skew leakage factor.

The air-gap leakage component results directly from the number of slots per pole and phase chosen and the magnetizing inductance. The other components can be increased or decreased in various ways of design.

In the case of a heavy working machine, the working speed range should be very large. In this case, the maximum speed should be for instance 20–30 times the maximum-torque speed. From the perspective of the reduction gear, this may be a disadvantage. The reasoning above easily excludes alternatives 1) and 2) and suggests integrating the electrical machine with a shiftable gear to increase the torque and speed ratios. Both approaches 1) and 2) may face certain difficulties; either the motor is too large (about three times the one with integrated gear) or its speed range is challenging for the reduction gear.

In an integrated solution, the planetary gear offers a natural choice. It is possible to build an electrical machine around a strong enough planetary gearbox to achieve the shortest possible drive system. A TCPMSM is also an obvious selection for this kind of integration as it may be easily implemented as a thin rim around the gearbox and use the limited space in the wheel hub in an efficient way.

To reach a practical solution we found a commercial gearbox with gear ratios 3.64:1 or 1:1 and designed a TCPMSM around it. If we limit the electrical machine torque to  $T_{e,pu} = 2$  at speeds below  $\omega_{s,pu} = 1/2$  and if the machine can reach  $\omega_{s,pu} = 3$  per-unit maximum speed and produce  $T_{e,pu} = 0.33$ , we end up in a torque range of 22, which should suffice for a heavy off-road working machine. The gear ratio of the planetary gear was not thoroughly optimized, but the torque range of 22 matches fairly well the assessment of the torque needs in Section 1.2. A thorough analysis of the optimal gear ratio requires exact information of the application where the integrated design is to be used. However, the gear ratios of planetary gears cannot typically be much wider than the one selected here.

Figure 2.2 illustrates the target torque as a function of the rotational speed curves of the integrated design at the direct 1:1 gear ratio and the reduction 3.64:1 gear ratio. The torque curves are calculated by using the current at the thermal limit of the machine.

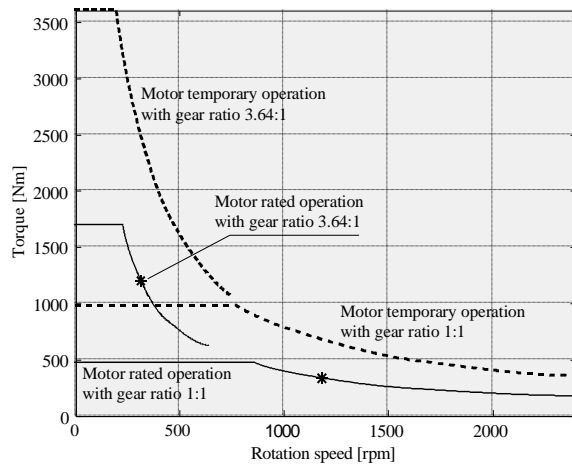


Fig. 2.2. Operating regions to be achieved by using the motor with an integrated two-step planetary gear switchable between gear ratios 3.64:1 and 1:1. The stars \* indicate the electrical machine design points. The chart assumes 50 % overload capacity in the constant flux area.

## 2.2 Electromagnetic design

High torque density is needed in heavy-duty off-road working machines. It can be achieved by using a tooth-coil PMSM with a high-quality neodymium iron boron (NdFeB) permanent magnet material. The  $BH$  curve, which gives the important magnetic properties of the permanent magnet for the selected N38UH permanent magnet, is shown in Fig. 2.3. This N38UH magnet has a remanent flux density value typically in the range of 1.22–1.26 T at room temperature (20 °C). The normal coercive force is in the range of 900–950 kA/m, and the maximum operating temperature is 180 °C. In principle, this means that the permanent magnet tolerates more heat in the case of PMSMs than the insulation of the winding copper wire. However, at so high temperatures the PM material is prone to the risk of permanent demagnetization in the occurrence of a terminal short circuit.

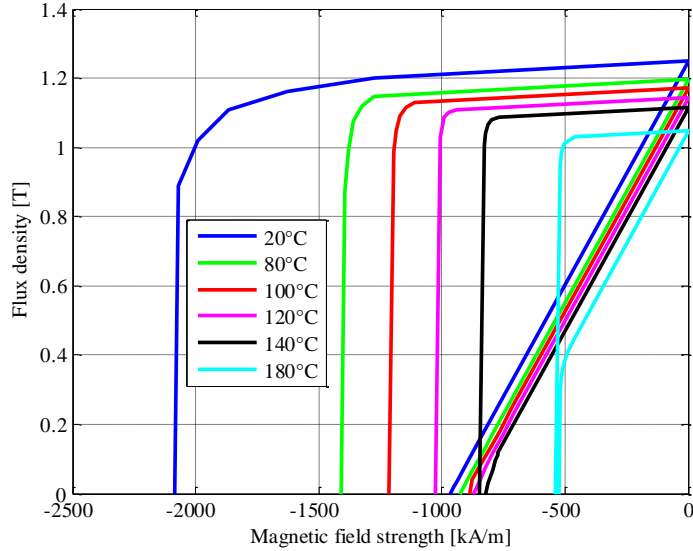


Fig. 2.3.  $BH$  curve of the NdFeB N38UH permanent magnet applied in the study (Eclipse Magnetics 2016).

Tooth-coil windings have current linkage distributions with a much higher spatial harmonic content than traditional distributed windings. This higher harmonic content can cause high rotor losses, high torque ripple, noise, and unbalanced radial forces. The electromagnetic properties of the windings of an electrical machine are characterized by the number of slots per pole and phase

$$q = \frac{Q_s}{2pm}, \quad (2.20)$$

where  $Q_s$  is the number of stator slots,  $p$  the number of rotor pole pairs, and  $m$  the number of stator phases in the machine.

Figure 2.4 illustrates the behaviour of the winding factor as a function of  $q$ . On the left side of the blue line there are the designs that have more rotor poles than stator slots. Correspondingly, the designs that have more stator slots than rotor poles are located on the right. Figure 2.5 depicts the leakage factor  $\sigma_\delta$  as a function of the number of slots per pole and phase.

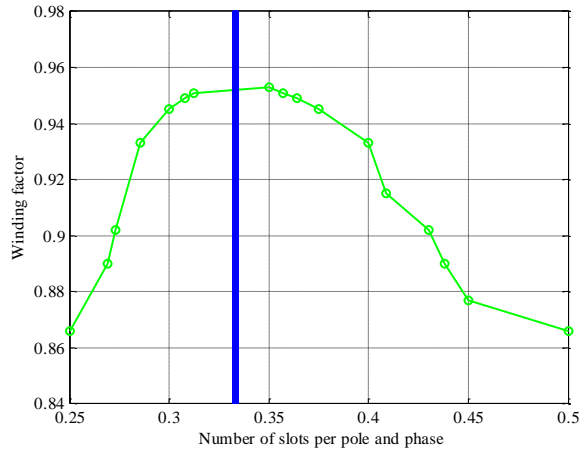


Fig. 2.4. Operating harmonic winding factor as a function of the number of slots per pole and phase. The highest practical value  $k_w = 0.951$  is reached at  $q = 5/14$  or  $q = 5/16$ . The blue line lies at  $Q_s/(2p) = 1$ , which is a prohibited design and would lead to high noise and cogging torque.

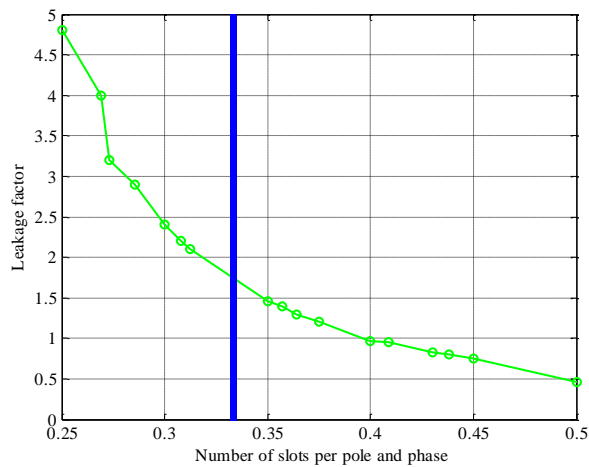


Fig. 2.5. Air-gap leakage factor as a function of the number of slots per pole and phase. The smaller  $q$  is, the larger are the values of the leakage factor  $\sigma_8$ . The blue line lies at  $Q_s/(2p) = 1$  (e.g. 12 slots 12 poles) corresponding to  $q = 1/3$ , which is a prohibited design.

As can be seen in the figures above, depending on the application, it is always a question of balance between the winding factor and the air-gap leakage factor. There is no optimum between the high winding factor and the leakage factor. Table 2.1 shows parameter selection for double-layer tooth-coil-wound PMSMs with various pole and slot combinations. The table provides information about the number of slots per pole and

phase  $q$ , the air-gap leakage factor  $\sigma_\delta$ , the operating harmonic winding factor  $k_w$ , and the least common multiple of  $Q_s$  and  $p$  (LCM). A high LCM is an indication of a possibly good torque quality. The influence of slot and pole combinations on torque quality has been discussed for example in (Zhu et al. 2014). Only the designs that have  $q \leq 0.5$  are listed in the table, and the design chosen for study is given in bold. Table 2.1 also shows the quality factor  $QF$ , which ranks the machines based on different boundaries according to the four previously presented factors. The  $QF$  is calculated by multiplying the four numbers  $a$ – $d$  defined as

$$QF = a \cdot b \cdot c \cdot d, \quad (2.21)$$

where

$$a = \frac{q}{0.5}, \quad b = \frac{1}{\sigma_\delta}, \quad c = \frac{k_w}{0.953}, \quad d = \frac{\text{LCM}}{336}.$$

The factors  $a$ – $d$  are calculated by dividing each machine value by the best possible table value to get the relative value of each factor. The highest torque is found by  $q = 0.5$  (Salminen et al. 2005), and therefore,  $a = 2q$ . The leakage term  $b$  is calculated in this case to favour a low leakage because the machine has to produce a large torque in the constant flux area, and on the other hand, it does not need a large rotational speed range because of the integrated gear. In the case of a very large field weakening area, the factor  $b$  should be selected to facilitate a large air gap leakage inductance. The factor  $c$  favours a high operating harmonic winding factor to minimize the Joule losses and  $d$  a high least common multiple of  $Q_s$  and  $p$  to produce as high inherent torque quality as possible. As it can be seen in Table 2.1, the 18/14 machine has the best  $QF$  with these criteria, and is thus selected for prototyping.

In the case of a very large field weakening area, the factor  $b$  in the above-mentioned  $QF$  should be selected to favour a large air gap leakage inductance. For example, an 18/20 machine has an air gap leakage value of  $\sigma_\delta = 2.4$ , which results in a very high air gap leakage, thereby enabling a high synchronous inductance.

Table 2.1. Parameters for various slot and pole combinations for double-layer tooth-coil-wound PMSMs.

$Q$	$2p$	4	6	8	10	12	14	16	18	20
6	$q$	0.5		0.25	0.2		0.142	0.125		0.1
	$\sigma_s$	0.46		4.8	26		53	22		36
	$k_w$	0.866		0.866	0.5		0.5	0.866		0.866
	LCM	12		12	30		42	48		54
	$QF$	0.071		0.036	0.089		0.001	0.001		0.001
9	$q$		0.5	0.375	0.3	0.25	0.214	0.188		0.15
	$\sigma_s$		0.46	1.2	2.4	4.8	0.46	71		112
	$k_w$		0.866	0.945	0.945	0.866	0.617	0.328		0.328
	LCM		18	72	90	36	126	144		90
	$QF$		0.104	0.132	0.066	0.01	0.225	0.001		0.001
12	$q$			0.5	0.4		0.286	0.25		0.2
	$\sigma_s$			0.46	0.96		2.9	4.8		26
	$k_w$			0.866	0.933		0.933	0.866		0.5
	LCM			24	60		84	48		60
	$QF$			0.14	0.145		0.048	0.033		0.001
15	$q$				0.5		0.357	0.313		0.25
	$\sigma_s$				0.46		1.4	2.1		26
	$k_w$				0.866		0.951	0.951		0.5
	LCM				30		210	240		60
	$QF$				0.175		0.318	0.212		0.005
18	$q$					0.5	<b>0.43</b>	0.375		0.3
	$\sigma_s$					0.46	<b>0.83</b>	1.2		2.4
	$k_w$					0.866	<b>0.902</b>	0.945		0.945
	LCM					36	<b>126</b>	144		180
	$QF$					0.21	<b>0.368</b>	0.265		0.142
21	$q$						0.5	0.438		0.35
	$\sigma_s$						0.46	0.8		1.5
	$k_w$						0.866	0.89		0.953
	LCM						42	336		180
	$QF$						0.246	1.02		0.291
24	$q$							0.5		0.35
	$\sigma_s$							0.46		1.5
	$k_w$							0.866		0.953
	LCM							48		210
	$QF$							0.282		0.145

All tooth-coil-wound machines (in Figs. 2.4 and 2.5) that have an odd number of stator slots are omitted from the analysis as they can have unbalanced radial forces. The limit for the air-gap leakage factor is put to  $\sigma_s = 1.2$  so that the machine torque capability in the constant flux linkage area does not suffer too much. All the machines that are based on the 3/2 base machine are also neglected as the leakage factor  $\sigma_s = 0.46$  is low for high-speed operation. Moreover, its winding factor is poor, which results in significant Joule losses. Its torque quality is low because the LCM is low. The PMSMs with over  $2p = 20$  poles are also neglected because of difficulties in the mechanical manufacturability in the requested size.

### 2.3 Synchronous inductance and performance analysis

The importance of synchronous inductance analysis cannot be overvalued in the design of electrical machines. Especially, the effect of d-axis synchronous inductance is decisive in salient pole machines as it basically defines the operating speed range of an electrical machine and, on the other hand, limits the maximum torque as shown in the modified load angle equation for a salient pole PMSM

$$T = \frac{mp}{\omega_s^2} \left( \frac{(U_s - R_s I_s) E_{PM}}{L_{md} + L_{s\sigma}} \sin \delta_s + \frac{(U_s - R_s I_s)^2 (L_{md} - L_{mq})^2}{2(L_{md} L_{mq} + L_{md} L_{s\sigma} + L_{mq} L_{s\sigma} + L_{s\sigma}^2)} \sin 2\delta_s \right). \quad (2.22)$$

The maximum speed range can be extended with the help of leakage inductance, especially in tooth-coil-wound machines, where the magnetizing inductances are typically small but air-gap leakage inductances can be large. In the industrial electrical machines this is totally different, as the leakage is usually minimized because a large leakage weakens the power factor of the machine. In traction machines instead, where the load is continuously changing, it is not advisable to look operation only in one point but in the whole speed range. It is found that the effect of large enough leakage is really important and beneficial especially in the field weakening region as it can increase the operating range in tooth-coil-wound machines. Figure 2.6 compares torque production of three machine designs as a function of increasing leakage inductance. In the same figure, the machine operation under current vector control in the rated point with the rated load is shown to demonstrate the performance in the field weakening region. The benefits of the leakage inductance in TCPMSMs can be seen by the considerably increased speed range. The drawback is the reduced torque production in the low-speed-high-torque situation. A high leakage inductance does not harm the machine in the rated operation very much as can be seen from Fig. 2.6 b.

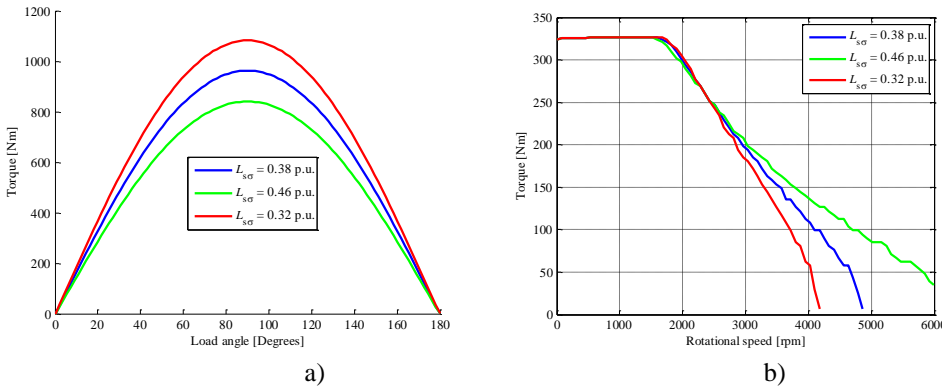


Fig. 2.6 Torque production capability curves a) and machine operation in the rated point under the converter control b). The parameters of the motor are  $E_{PM,pu} = 0.9$ ,  $L_{md,pu} = 0.17$ ,  $L_{mq,pu} = 0.22$ ,  $R_{s,pu} = 0.02$ . The phase voltage is 230 V, the rotational speed  $1200 \text{ min}^{-1}$ , and the number of phases  $m = 3$ . The pole pair number  $p$  is 7. The green torque curve is the one from the prototype.

This means that the leakage inductance can be used to adjust the amount of the total synchronous inductance

$$L_{sd} = L_{md} + L_{s\sigma}, \quad (2.23)$$

$$L_{sq} = L_{mq} + L_{s\sigma}. \quad (2.24)$$

As can be seen in Eq. (2.22), the torque has a strong dependence on the synchronous inductances. Again, if the leakage inductance can be used to increase the field weakening range, it will, on the other hand, decrease the maximum available torque. As can be seen, the stator voltage is the second power term in the latter part of the torque equation. Therefore, it is beneficial to increase the voltage to speed ratio, especially in traction applications. This leaves us the option to have a higher d-axis magnetizing inductance and thus, a higher leakage inductance. Of course, the smaller the d-axis synchronous inductance is, the better are the acceleration properties of the traction machine.

The magnetizing inductance can be written similarly for both the d- and q-axes by changing the effective air-gap term  $\delta_{de}$  in

$$L_{md} = \frac{mD_s}{\pi p^2 \delta_{de}} \mu_0 l' (k_w N_s)^2, \quad (2.25)$$

where  $p$  is the number of pole pairs,  $m$  is the number of phases,  $\mu_0$  is the permeability in a vacuum,  $l'$  is the effective length,  $D_s$  is the air-gap diameter,  $N_s$  is the number of coil turns, and  $k_w$  is the winding factor of the working harmonic. Usually, the q-axis magnetizing inductance needs some numerical method such as finite element analysis to validate the calculations as it is difficult to calculate analytically.

Based on the analytical calculations and Eq. (2.22), the load angle curve was built; see Fig. 2.7. It is compared with the curve calculated by the FEA.

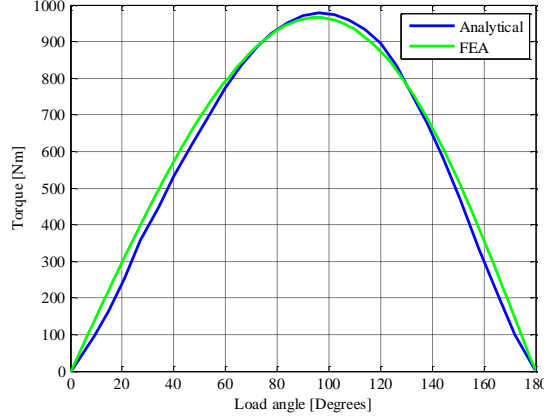


Fig. 2.7. Load angle curves calculated analytically and by the FEA for the PMSM. The machine has its maximum value around 96–97° and the rated torque at 26°.

## 2.4 Machine loss calculation

In permanent magnet synchronous machines there are five different loss components. On the stator side there are copper losses and iron losses. Some iron losses are also present in the rotor. The rotor also has permanent magnet eddy current losses and mechanical and friction losses caused by the rotating movement. In some cases, also PM hysteresis losses may be present. Moreover, when a converter is applied, there are converter switching losses. All other losses are summed up and are referred to as additional losses. Copper losses in the stator windings can be calculated directly from the winding resistance and current

$$P_{Cu} = mR_s I_s^2, \quad (2.26)$$

where  $m$  is the number of phases,  $R_s$  is the phase winding resistance, and  $I_s$  is the stator current. Iron losses in the stator and the rotor can be calculated with the same equations. The total iron losses can be divided into hysteresis, eddy current, and excess losses, which are calculated as follows

$$P_{Fe} = P_{Hyst} + P_{Eddy} + P_{Exc}, \quad (2.27)$$

where

$$P_{Hyst} = k_h \hat{B}f, \quad (2.28)$$

$$P_{Eddy} = \frac{\pi^2 \sigma d^2 (\hat{B}f)^2}{6} \quad (2.29)$$

$$P_{\text{Exc}} = k_e \left( \hat{B} f \right)^{\frac{3}{2}}, \quad (2.30)$$

where  $f$  is the frequency,  $\sigma$  is the conductivity of the material,  $d$  is the lamination sheet thickness,  $\hat{B}$  is the maximum flux density,  $k_h$  is the hysteresis loss constant,  $k_e$  is the excess loss constant, and  $k_{\text{Fe}}$  is the iron space factor (Bertotti 1988), (Pippuri 2010), (Pyrhönen et al. 2014). The calculation of mechanical and friction losses is presented in Chapter 3 when the overall machine prototype is analysed as this machine needs a special equation for the mechanical losses because of the direct oil cooling.

Figure 2.8 presents the stator and rotor iron losses and permanent magnet eddy current losses calculated by the FEA at different speeds.

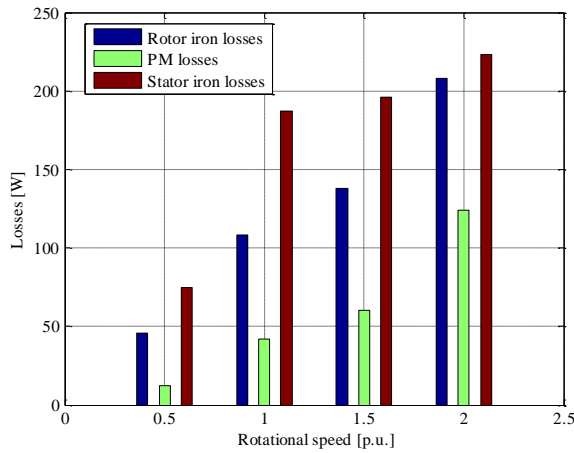


Fig. 2.8. Speed-dependent losses of the motor under study, based on the FEA.

## 2.5 Control principles of the traction salient pole PMSM

In vehicle applications, the PMSM drives use the stator current vector control rather than the direct torque control as the focus is on the current control (Nalepa and Orłowska-Kowalska 2012). Direct torque control (DTC) can also be adapted to indirectly provide the different control modes. In this section, the three current control algorithms that maximize the torque production in different operating states are presented. The algorithms are the maximum torque per ampere, the field weakening, and the maximum torque per voltage.

### 2.5.1 Maximum torque per ampere control (MTPA)

At speeds below the rated rotational speed, the maximum torque per ampere (MTPA) control method is used. The objective of the method is to minimize the current to achieve the maximum torque. Only one current component pair produces the maximum torque,

and it can be found by finding the derivative of the torque equation as a function of current angle and by setting it to zero

$$\frac{dT}{d\gamma} = \frac{3p}{2} \left( -\psi_{PM} i_s \cos \gamma + (L_{sq} - L_{sd}) i_s^2 \cos 2\gamma \right) = 0. \quad (2.31)$$

Here, we see that the reluctance torque component has importance only with a significant inductance difference. The optimal current components for the MTPA algorithm after substituting  $\gamma$  can now be written in the form

$$i_{sd} = \frac{\psi_{PM} - \sqrt{\psi_{PM}^2 + 8(L_{sq} - L_{sd})^2 i_s^2}}{4(L_{sq} - L_{sd})}, \quad (2.32)$$

$$i_{sq} = \sqrt{i_s^2 - i_{sd}^2}. \quad (2.33)$$

The current references are obtained in previous Eqs. (2.32) and (2.33).

### 2.5.2 Field weakening control

After the MTPA control when the speed is close to its rated value and the voltage is at its limit, it is no more possible to supply more voltage. Then, the field weakening (FW) control must take place. The target of the control method is to weaken the stator flux linkage level of the PMSM to enable a higher speed. In the field weakening, the torque production capability of the drive is limited but the output power can be kept constant depending on the field weakening capability of the motor and the current capacity of the converter. The equations for the current components can be calculated by defining them under the voltage constraint (Morimoto et al. 1990) as follows

$$i_{sd} = \frac{L_{sd} \psi_{PM} + \sqrt{(L_{sd} \psi_{PM})^2 + (L_{sq}^2 - L_{sd}^2) \left( \psi_{PM}^2 + L_{sq}^2 i_s^2 - \left( \frac{u_s}{\omega} \right)^2 \right)}}{(L_{sq}^2 - L_{sd}^2)}, \quad (2.34)$$

$$i_{sq} = \sqrt{i_s^2 - i_{sd}^2}. \quad (2.35)$$

When the speed is increasing, the internal induced voltage is proportional to the rotating speed of the machine, and therefore, the stator flux linkage has to decrease. Depending on the strategy, the FW control can keep the total resultant stator current constant at its rated value. Such a selection maintains the motor temperature at its rated value. Depending on the current and cooling resources of the drive system, it is also possible to increase the current from its rated value also in the FW to produce power above the rated level. The stator resistance is neglected in these equations as the traction machines usually have 0.01–0.03 p.u. stator resistance, which does not have a significant effect on anything.

The control of machines having a high stator resistance and a high level of magnetic saturation has been reported for example in (Jo et al. 2008), (Tursini et al. 2010).

When the stator flux linkage level is reduced and the current angle  $\gamma$  is controlled, the magnitude of the stator current stays at its rated value. When the speed increases further, the control aims towards the end of the FW control, and in some special situations the output characteristics can be improved by changing the control method to the maximum torque per volt, which is presented in brief in the next section.

### 2.5.3 Maximum torque per volt control (MTPV)

The stator current must be controlled in the case of limited stator voltage operation. The target of this method is that for a given torque demand, the voltage is limited. This condition occurs when the characteristic current (Eq. (2.7)) of the machine is smaller than 1 p.u., meaning that the d-axis per-unit inductance is higher than the PM flux linkage per unit value. Taking the first derivative of the torque equation with respect to  $dT/di_d$  and using Eqs. (2.3) and (2.4), the stator current vector producing the maximum amount of torque under the voltage constraint can be derived (Illioudis and Margaritis 2010). The equations for the current components with the MTPV method are

$$i_{sd} = -\frac{\psi_{PM}}{L_{sd}} - \Delta i_{sd}, \quad (2.36)$$

$$i_{sq} = \frac{\sqrt{\left(\frac{U_s}{\omega}\right)^2 - (L_{sd}\Delta i_{sd})^2}}{L_{sq}}, \quad (2.37)$$

where

$$\Delta i_{sd} = \frac{-\frac{L_{sq}}{L_{sd}}\psi_{PM} + \sqrt{\left(\frac{L_{sq}}{L_{sd}}\psi_{PM}\right)^2 + 8\left[\left(\frac{L_{sq}}{L_{sd}} - 1\right)\left(\frac{u_s}{\omega}\right)\right]^2}}{L_{sq}}. \quad (2.38)$$

The equations are valid only in the MTPV control. The MTPV control is used only on special occasions at the highest speeds if the machine design is applicable for its use. In the MTPV region, the current is always smaller than the rated current, and the voltage amplitude is at its rated value, which is equal to the voltage limit. Figure 2.9 demonstrates the principles of the previously presented control strategies.

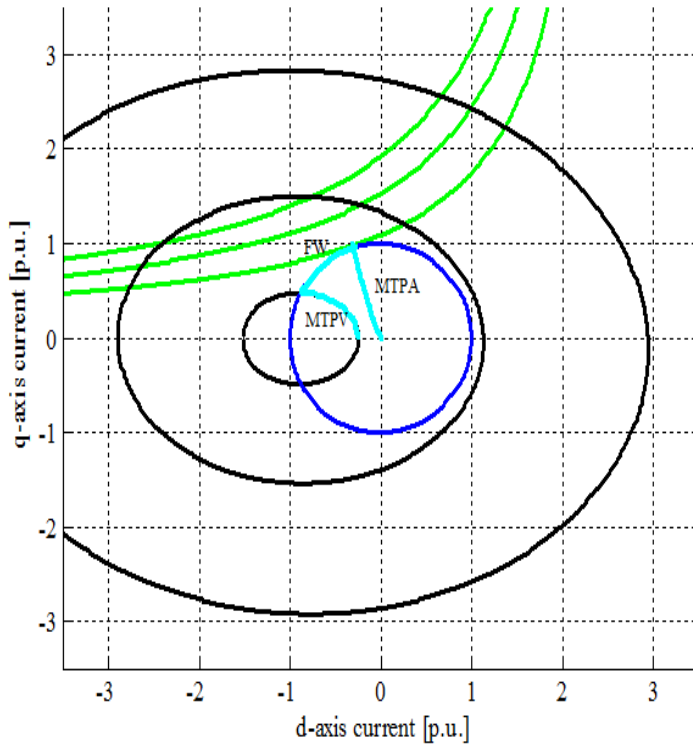


Fig. 2.9. Current control in different control strategies. The cyan curve has three different control modes (MTPA, FW, MTPV). The current limit is indicated by a blue circle ( $i_s = 1$  p.u.), and the ellipses show the voltage limits at different speeds ( $\omega_s = 0.5, 1, \text{ or } 2$ ) when operating with the rated permanent magnet flux linkage  $\psi_{PM} = 0.45$  p.u. The smaller the ellipse at a higher speed is, the more current must be used to decrease the stator flux linkage level. At a certain speed the operation must take place both inside the ellipse and the current limit circle. The green trajectories represent constant torques. The lowest curve represents operation at the rated torque. The MTPA curve meets the trajectory in the point when field weakening starts at the rated torque. The upper curves represent high-current excess per-unit torques of 1.25 and 1.5, respectively.

## 2.6 Summary of Chapter 2

The chapter focused on the TCPMSM. Its mathematical model was explained in brief assuming that the reader has sufficient background knowledge of the machine type. The decision to choose of the TCPMSM instead of some other PMSM type was discussed. The TCPMSM has at least two important features in traction applications: its speed range can be adjusted by suitable selection of synchronous inductance and according to its general suitability for mechanical integration. The electromagnetic design of the TCPMSM together with the control principles was described.

### 3 Integrated solution

It has been shown in the introduction of this work that some kind of a mechanical gear is needed in heavy-duty working machines. A reduction gear is needed to achieve high torque, for instance when cultivating or loading the bucket, or in the start-up; on the other hand, a direct gear is needed when high speed is required for instance to move the machine on the road. This chapter presents the construction and a novel solution for the prototype machine.

Figure 3.1 presents a schematic and a realistic figure of the tooth-coil-wound permanent magnet synchronous machine (TCPMSM) with an integrated two-step planetary gearbox inside the rotor.

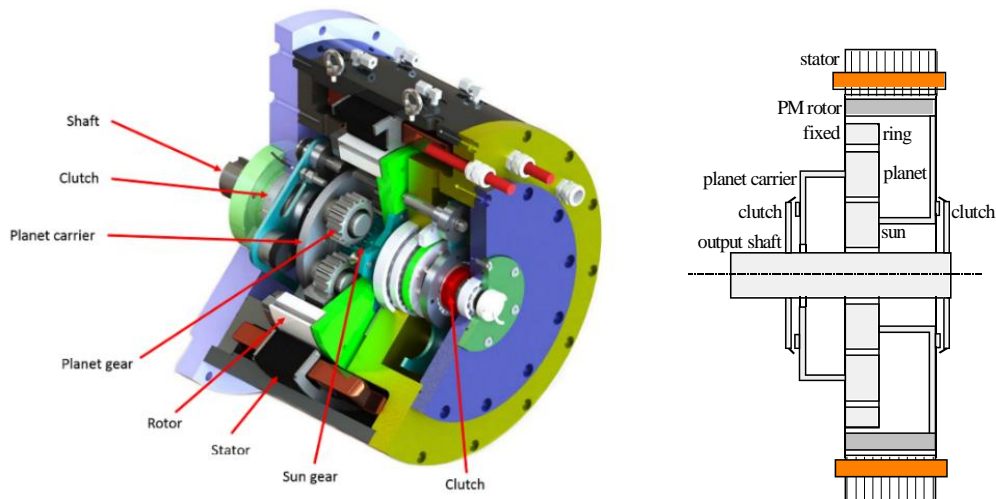


Fig. 3.1. TCPMSM with an integrated two-step planetary gearbox and its simplified schematic.

The rotor of the electric machine is directly connected to the sun gear of the planetary gear system. The green plate in the figure illustrates the connection between the rotor and the sun gear. If the right-hand dog clutch is engaged, the motor output is directly connected to the output shaft. If the left-hand dog clutch is engaged, the torque is taken via the planet carrier and a speed reduction, depending on the teeth number of the sun, planet, and ring cogwheels. The gear ratio is the division between the teeth number of the sun gear and the sum of the teeth numbers of the sun gear and the ring gear. Typical values that can be easily achieved are from 1:2 to 1:10 (Lynwander 1983). In the case of the prototype, the reduction is 1:3.64.

The planetary gear also dictates the maximum speed of the motor. In this case, according to the manufacturer, the fairly large planetary gear tolerates about  $2400 \text{ min}^{-1}$  at the sun.

Based on this, the rated speed of the electric motor was selected to be half of this speed to reach a base speed area of 0–1200  $\text{min}^{-1}$  and a field weakening area with a constant power output of 1200–2400  $\text{min}^{-1}$ .

The above-mentioned example of an agricultural tractor showed that one of the toughest tasks is ploughing at 2 m/s with 31 kN, resulting in 62 kW of power. The top speed of a normal agricultural tractor is 50 km/h, which corresponds to 13.9 m/s. The integrated design motor runs at 2400  $\text{min}^{-1}$  at this top speed with the direct gear. At the rated motor speed, the tractor speed is 6.95 m/s. With the 1:3.64 reduction gear, the tractor speed is 1.9 m/s. Therefore, with the reduction gear, the ploughing speed goes slightly into the field weakening. Four 40 kW units should cope with the task.

### 3.1 Electromagnetic design

The design procedure of the electric machine design can be found for instance in (Pyrhönen et al. 2014). The important boundaries for the design are usually

- Rated output power
- Rated voltage
- Rated rotational speed
- Number of phases
- Winding type
- Desired tangential stress  $\sigma_{F_{\text{tan}}}$ , which indicates the cooling type required
- Maximum torque and speed (typical for traction applications)
- Size limitations for the machine dimensions; diameters and length (typical for traction applications)
- Maximum voltage and current of the inverter

All the machines can be designed mainly by knowing all the characteristics listed above. Typically, in traction applications as in the case of this doctoral dissertation, there are mechanical and dimensional limitations that have to be known at the start of the electromagnetic design. The design process is outlined in the flow chart of Fig. 3.2. The guidelines of the traction motor design process have been given by the author previously in (Montonen et al. 2014) and (Montonen et al. 2012).

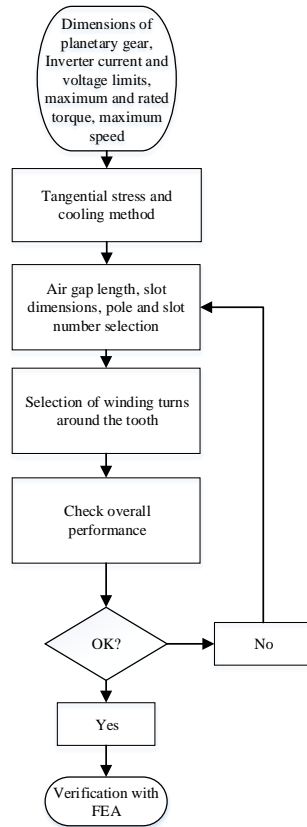


Fig. 3.2. Flow chart of the design process.

The mesh used in the FEM model is presented in Fig. 3.3. Because of the symmetry, only half of the machine was modelled. By dividing the model into smaller parts, it was also possible to significantly reduce the calculation time. The mesh nodes are smaller near the air gap, where the most important effects take place.

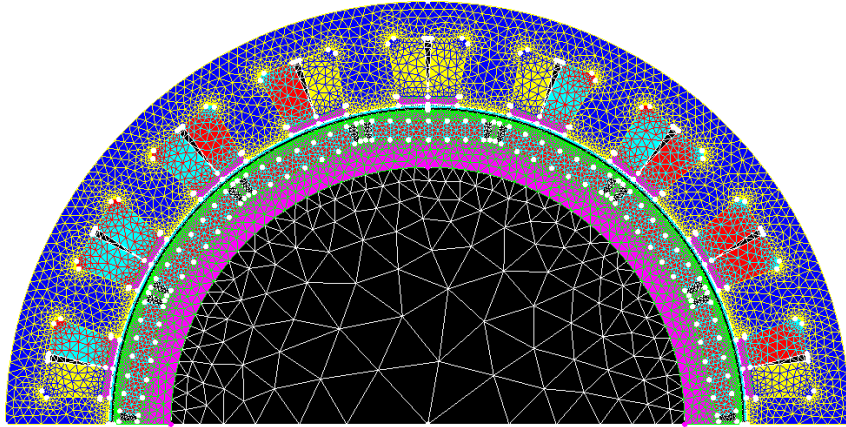


Fig. 3.3. Mesh of the FEM model applied.

Fig. 3.4 presents the flux density contour plot of the machine. It is noteworthy that the values of the flux density are in the region of 2.1–2.3 T on the q-axis. The flux density values in the stator yoke and teeth are in the range of 1.0–1.6 T, which is a typical value for electrical machines (Pyrhönen et al., 2014).

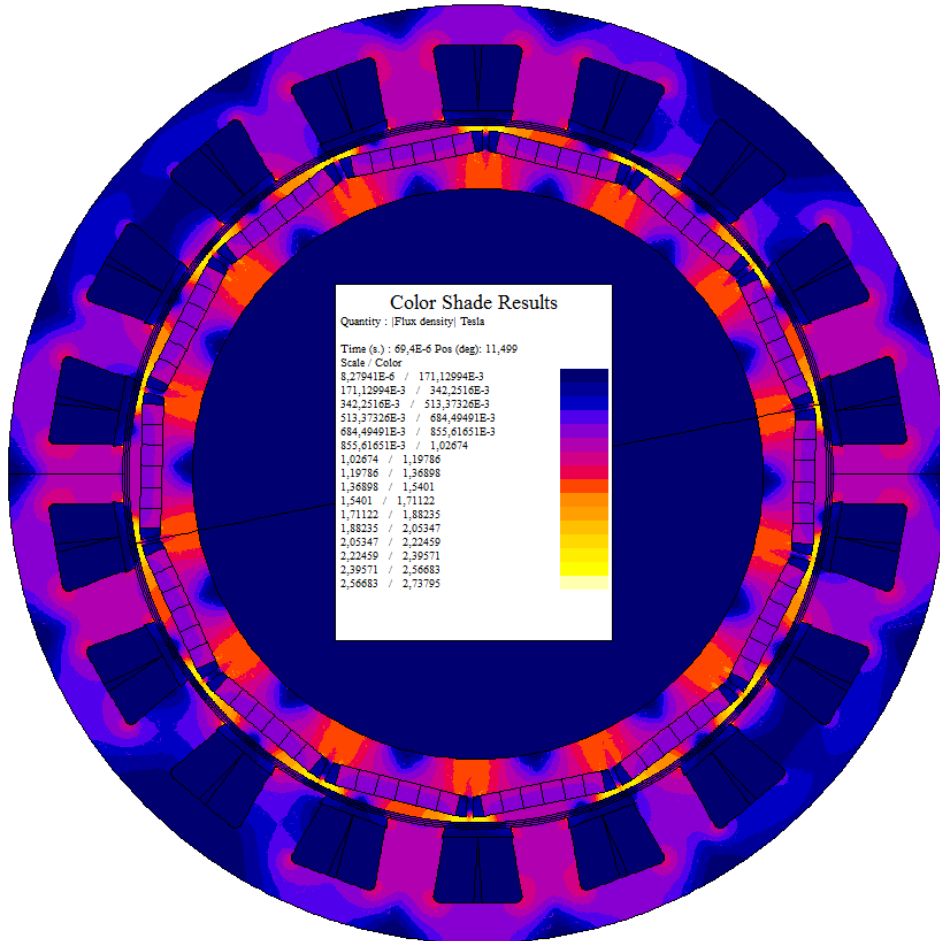


Fig. 3.4. Flux density plot of the 18/14 machine in the rated operating point.

The FEA-calculated normal components of the flux density waveforms in the air gap at no load at the rated speed and at the rated load for the design under study are presented in Fig. 3.5.

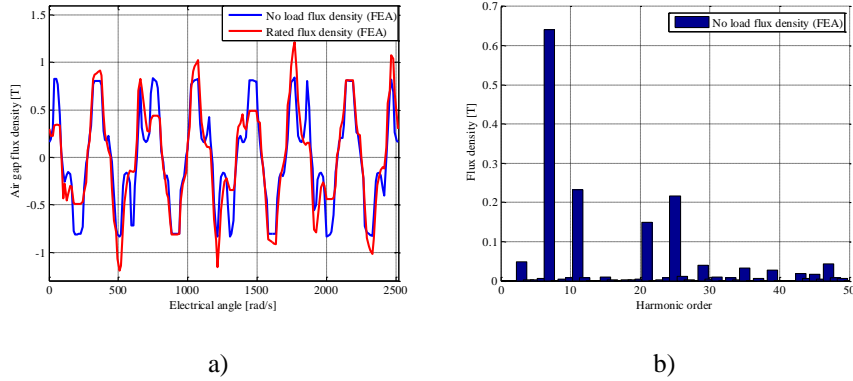


Fig. 3.5. Waveform analysis of the flux density normal components; a) comparison of the air-gap flux density curves at no load (blue) and at the rated load (red) and b) harmonic spectra at no load. The seventh, that is, the working harmonic of the machine is clearly dominating.

Because of the open slots of the machine, stator slot wedges are needed to hold windings in their places. A study was made to get information of material properties most appropriate for the slot wedges. The options were to use non-magnetic glass fibre or semi-magnetic material with a relative permeability of  $\mu_r = 3$ . Fig. 3.6 compares the air-gap flux density waveforms for non-magnetic and semi-magnetic slot key materials.

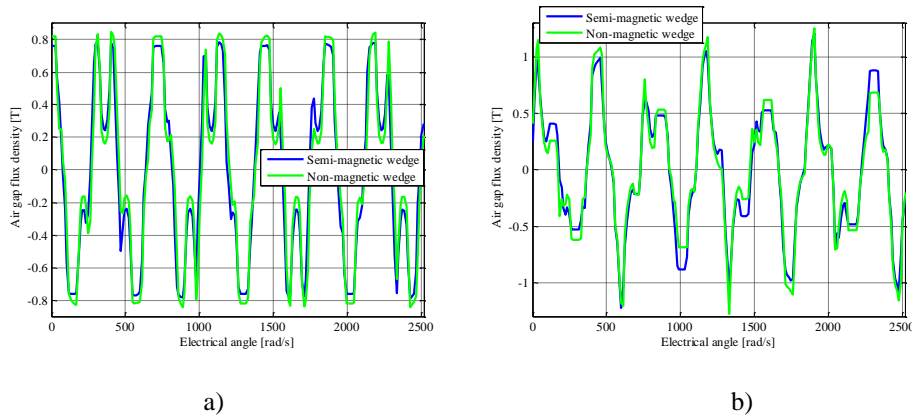


Fig. 3.6. Waveform analysis of the flux density normal component; a) comparison of the air-gap flux density curves at no load b) and at the rated load.

By using the semi-magnetic slot wedge, the highest peaks of the flux density wave are smoothed, as a result of which the current will also be smoother. Therefore, semi-magnetic slot keys are selected instead of glass fibre ones.

It is important to ensure that the current density  $J$  remains at an acceptable level in the slot. The total copper cross-sectional area in the slot can be estimated by

$$S_{\text{Cus}} = \frac{r_{\text{Cu}}^2 z_Q \pi n_{\text{par}}}{k_{\text{Cu}}}, \quad (3.1)$$

where  $r_{\text{Cu}}$  is the wire radius, in this case copper,  $z_Q$  is the number of turns around one tooth,  $n_{\text{par}}$  is the number of parallel branches, and  $k_{\text{Cu}}$  is the slot fill factor, which is normally in the range of 0.55 for round wires.

Compared with traditional industrial motors with integral slot windings, the prototype motor has a large slot, which guarantees a low current density value in the rated operation of the motor. According to (Pyrhönen et al 2014), for instance typical slot pitches of industrial induction motors vary between 7 and 45 mm. In this case, the slot pitch is 58 mm. The current density value of 4 A/mm<sup>2</sup> used here is so low that the machine can, in practice, be overloaded by 150 % continuously below the rated operating speed.

The slot dimensions are presented in Fig. 3.7.

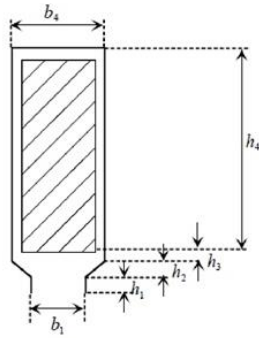


Fig. 3.7. Slot dimensions in the prototype:  $b_1 = 31$  mm,  $b_4 = 40$  mm,  $h_1 = h_2 = 2$  mm,  $h_3 = 0.7$  mm, and  $h_4 = 30$  mm. This will result in a total slot height of 34.7 mm. A large slot guarantees a low current density.

### 3.1.1 Winding configuration

The machine winding was chosen to be a two-layer tooth-coil winding to achieve the shortest possible end windings. Next, an overall comparison of the four most suitable 18-slot machines is made; on average, the 18-slot machines seem to be the best choice for this application. The selected candidates were chosen based on the calculated quality factor (overall, the 18-slot machine seemed to have the best  $QF$  in this case). The machines selected for the analysis are 18/12 (3/2), 18/14, 18/16, and 18/20 ones. The 18/12 machine operates with the base machine 3/2 fundamental, and the machine produces traditional three-phase machine harmonics. The 18/14 machine is the base machine itself and therefore operates with the seventh harmonic. This machine also produces the same harmonic ordinals as traditional three-phase machines. The base machine of the 18/16 machine is a 9/8 machine operating with the fourth air-gap

harmonic. The base machine of the 18/20 machine is a 9/10 one, operating again with the fifth harmonic. Therefore, the machine produces similar air gap harmonics as a traditional three-phase machine. All harmonics, except for the operating one, do not participate in torque production. These harmonics, which do not produce torque induce additional voltage in the windings and contribute to the leakage inductance increasing the armature reaction. This is harmful as they might lead to saturation in the iron core and an increase in the rotor iron and PM losses.

Table 3.1. Comparison of the significant current linkage harmonics and their moving directions and per-unit frequencies seen at the rotor surface of machines under study.

3/2	$v$	+1	-5	7	-11	13	-17	19	-23
	$f$	0	6	6	12	12	18	18	24
18/14	$v$	+1	-5	7	-11	13	-17	19	-23
	$f$	0.86	1.7	0	2.57	0.86	3.43	1.71	4.29
9/8	$v$	+1	-2	+4	-5	7	-8	10	13
	$f$	0.75	1.5	0	2.25	0.75	3	1.5	2.25
9/10	$v$	+1	-5	7	-11	13	-17	19	-23
	$f$	1.2	0	2.4	1.2	3.6	2.4	4.8	3.6

The induced voltage waveforms of the machines are compared in Fig. 3.8 at the rated speed of  $1200 \text{ min}^{-1}$  at  $20^\circ \text{C}$  temperature.

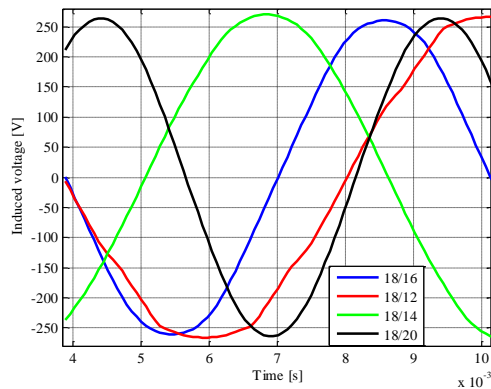


Fig. 3.8. Induced voltage waveforms of the machine alternatives in the no-load condition at a  $1200 \text{ min}^{-1}$  rotational speed. The 18/14 machine provides the best voltage waveform purity, but all alternatives are good, except maybe the 3/2 (18/12) machine, which is known for its problems.

The curves in Fig. 3.8 also indirectly indicate that a large LCM is preferred in order to have a low torque ripple. The induced voltages are almost at the same level, but the most sinusoidal waveform is found in the 18/14 design. High air-gap leakage factors were the main reason to avoid 18/16 and 18/20 PMSMs because a high leakage sacrifices the peak torque in the constant flux linkage area. The deep field weakening range is not so significant in this application, and therefore, a fairly low synchronous inductance is preferred. The 18/12 machine (3/2 base machine with  $q = 0.5$ ) produces a high torque but also a high torque ripple, and should thus be skewed.

The grounds for selecting the 18/14 machine are the following: 1) It has been shown that machines with a high  $q$  have usually an adequate torque producing capability (Salminen et al. 2005). The value of  $q = 0.43$  is close to the limiting value of  $q = 0.5$ , beyond which we have distributed windings. However, the value of  $q = 1/2$  produces poor torque quality. 2) The air-gap leakage factor with  $q = 0.43$  is moderate,  $\sigma_\delta = 0.83$  resulting in a moderate stator leakage inductance (Ponomarev 2013). This is now desirable as the field weakening range is not wide because a gearbox has to be used. 3) The winding factor of the operating harmonic ( $\nu = 7$ ) is also acceptably high,  $k_w = 0.902$ , resulting in low Joule losses. 4) The 18/14 machine configuration has a high LCM resulting in almost purely sinusoidal induced voltage and smooth torque. A higher LCM would yield an even lower waveform of the cogging torque, but it results in higher-frequency torque fluctuation. Based on these factors, the 18/14 machine is kept as a good starting point for the integrated design. The winding configuration is presented in Fig 3.9.

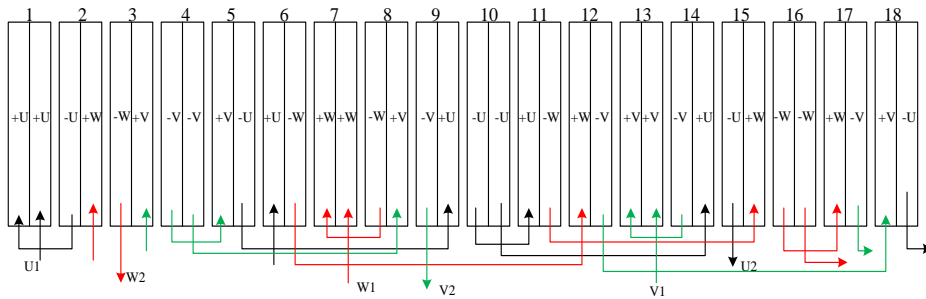
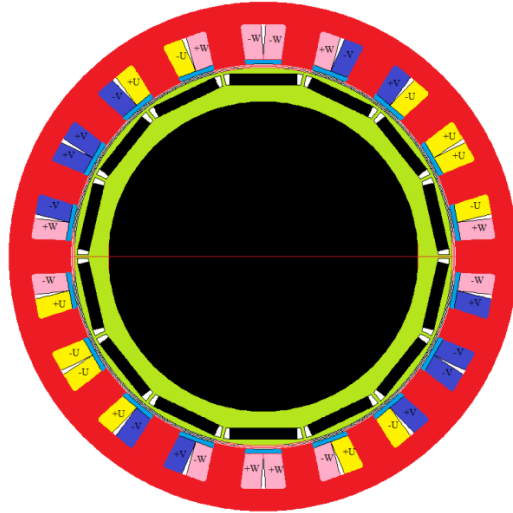
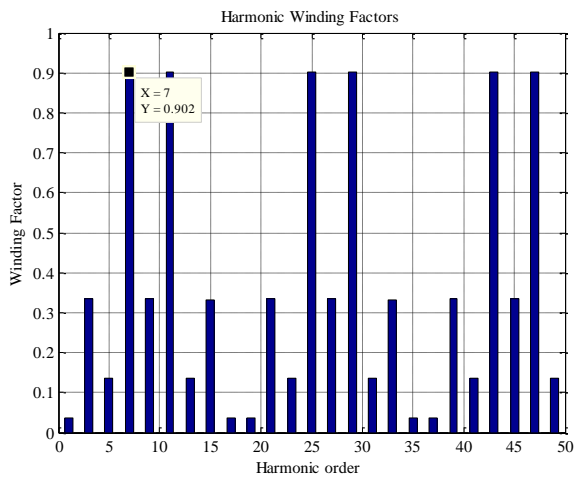


Figure 3.9. Winding arrangement of the designed prototype machine.

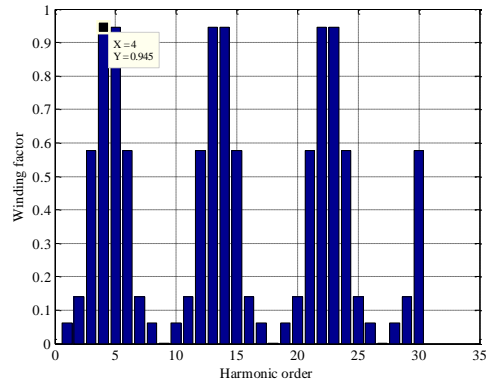
Despite its good properties, the 18/14 machine has received little attention in the literature compared with other types of machine. Previously, the 18/14 machine has been analysed for instance in (Dutta et al. 2013). The geometry, winding structure, and harmonic analysis of the machine are presented in Fig. 3.10.



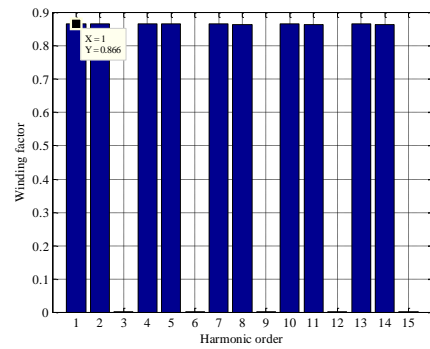
a)



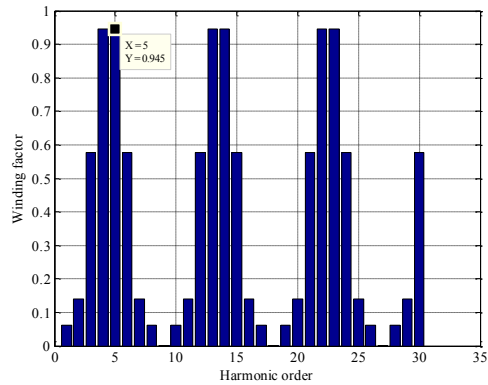
b)



c)



d)



e)

Fig. 3.10. a) Geometry and winding structure of the 18/14 machine and b) harmonic analysis of the winding function. The operational harmonic of the machine is the 7<sup>th</sup> one. The same winding could also operate with a 22-pole rotor and have  $\nu = 11$  as the operating harmonic. c) Harmonic analysis of the winding function of 18/16, d) 18/12 (3/2 base machine), and e) 18/20 (9/10 base machine) machines.

A small fundamental winding factor  $k_{w1} = 0.04$  also occurs. The low value of the fundamental is a benefit of this machine as it results in low rotor losses caused by the fast rotating armature fundamental. The stator with this winding arrangement could also work with the 11<sup>th</sup> harmonic to make an 18/22 machine. However, increasing the pole pair number from 7 to 11 would result in an increased frequency and thereby higher iron losses, and also permanent magnet eddy current losses.

Based on the analysis and the  $QF$ , the 18/14 machine will be studied in the following. Its overall properties for this traction drive task seem the most appropriate.

### 3.2 Saturation and cross-saturation

Normal saturation is calculated for each axis individually. Fig. 3.11 presents the flux linkages and inductances of the motor as all the current is supplied to one axis only to obtain the flux linkage from the selected axis. The plots are obtained by linearization of differential inductances by using Eqs. (3.2) and (3.3). The step used in the calculation is  $\Delta i_{d,q} = 10$  A.

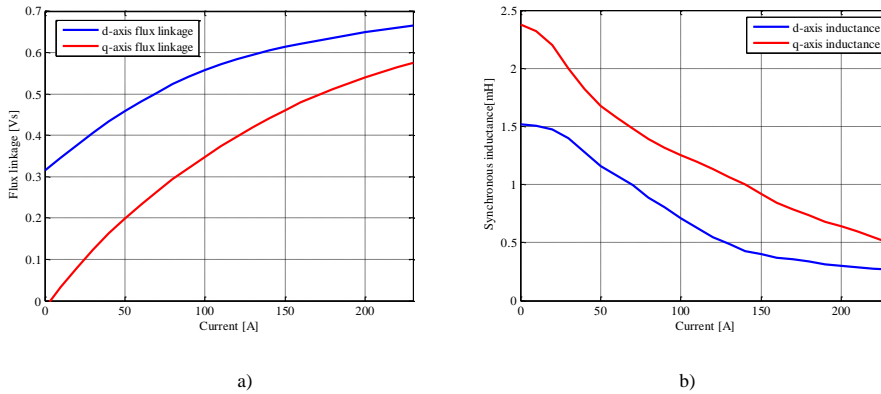


Fig. 3.11. a) Flux linkages and b) synchronous incremental inductances of the 18/14 machine as a function of peak stator current. The current step used in the calculation is  $\Delta i_{d,q} = 10$  A.

The flux linkages and synchronous inductances were obtained from the static FEA when the coils were supplied by direct currents and the rotor was locked either in the q-axis or d-axis position. Incremental synchronous inductances for both axes are shown in Fig. 3.12, respectively. The incremental synchronous inductances can be determined numerically in locked-rotor positions as follows by using the differential flux linkage method (Stumberger et al. 2003), (Qi et al. 2009)

$$L_d(i_d, i_q) = \frac{\partial \psi_d(i_d, i_q)}{\partial i_d} \approx \frac{\Delta \psi_d(i_d, i_q)}{\Delta i_d}, \quad (3.2)$$

$$L_q(i_d, i_q) = \frac{\partial \psi_q(i_d, i_q)}{\partial i_q} \approx \frac{\Delta \psi_q(i_d, i_q)}{\Delta i_q}. \quad (3.3)$$

As Fig. 3.12 illustrates, the incremental synchronous inductances are strongly dependent on the axis currents. At no load, the machine is fairly non-salient,  $L_d \approx L_q$ . Saliency can be observed based on different saturations; furthermore, a fairly strong cross-saturation phenomenon can be observed. The d-axis incremental synchronous inductance remains relatively stable as a function of q-axis current with  $i_d = 0$ . The cross-saturation reduces  $L_d$  from 1.5 mH at no load to about 1.2 mH at the 200 A q-axis current with  $i_d = 0$ .

The q-axis incremental synchronous inductance has strong self-saturation at low values of  $i_q$ , which is natural as the magnet retaining ring starts to saturate under the q-axis armature reaction.  $L_q$  is fairly insensitive to negative d-axis currents, and therefore, the cross-saturation does not significantly affect the machine control.

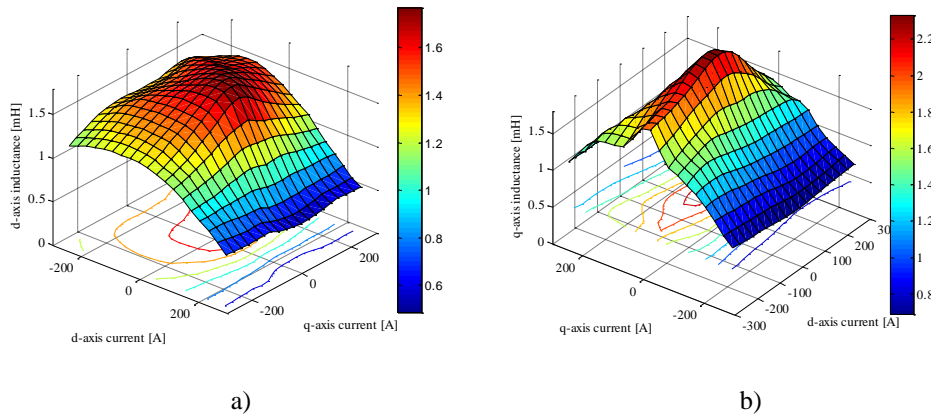


Fig. 3.12. Incremental synchronous inductances of the motor as a function of d- and q-axis currents, a) d-axis inductance, and b) q-axis inductance.

All the positive direct-axis currents are causing heavy saturation. The armature reaction caused by a high quadrature-axis current component amplitude also saturates the machine heavily. In normal operation, magnetizing positive d-axis current is not used, but high q-axis current values occur when high torque is produced. The q-axis inductance varies more than the d-axis inductance as a function of currents, because the permanent magnets affect the q-axis inductance only by cross-saturation (e.g. torque).

The machine saturation must be taken into account to reach high accuracy, also in the driving cycle analysis, and hence, an analysis with rated-point equivalent circuit parameters would lead to somewhat erroneous results and should be avoided when the control logic is designed. These inductance maps can be embedded by look-up tables in

the memory of controllers. In that way, a good overall torque quality can be reached in every operating state, and hence, optimal control logic can be used to drive the machine.

### 3.3 Torque quality

Different techniques to minimize cogging torque and torque ripple have been presented in the literature (Li et al. 2009), (Bianchi et al. 2002), (Petrov et al. 2014), (Wang et al. 2013), (Alberti et al. 2014) and (Azar et al. 2012). Next, the cogging torque and torque ripple of the 18-slot 14-pole machine are analysed. Their waveforms and harmonic analysis are shown in Figs. 3.13 and 3.14 both over one electrical cycle.

From the cogging torque spectrum, it can be seen that the most crucial component is the tooth harmonic component, which is the 18<sup>th</sup> one in this machine. The machine produces less than 0.1 % cogging torque, which is negligible. If desired, the cogging, and thereby the torque ripple, can be further decreased by decreasing the slot openings, increasing the air-gap length, or skewing the slots. Open slots and semi-magnetic wedges are used in the prototype machine to enable easy winding work. Naturally, manufacturing imperfections can also lead to an increasing cogging torque (Gasparin et al. 2009).

The no-load voltage and its harmonic spectrum are presented in Fig. 3.15. The total harmonic distortion (THD) estimates the sinusoidal waveform of the no-load PM-induced voltage. It can be expressed as

$$\text{THD} = \frac{\sqrt{\sum_{v=2}^{\infty} E_v^2}}{E_1}, \quad (3.4)$$

where  $E_1$  is the RMS or peak voltage of the fundamental harmonic, and  $E_v$  is the RMS or peak voltage of the  $v^{\text{th}}$  harmonic.

The no-load voltage THD of the motor is less than 2 %, consisting mostly of the 6<sup>th</sup>, 12<sup>th</sup>, and 18<sup>th</sup> harmonics. This is a major benefit of the 18/14 optimized construction. Stresses caused to the drive train are practically free of torque ripple caused by the motor itself.

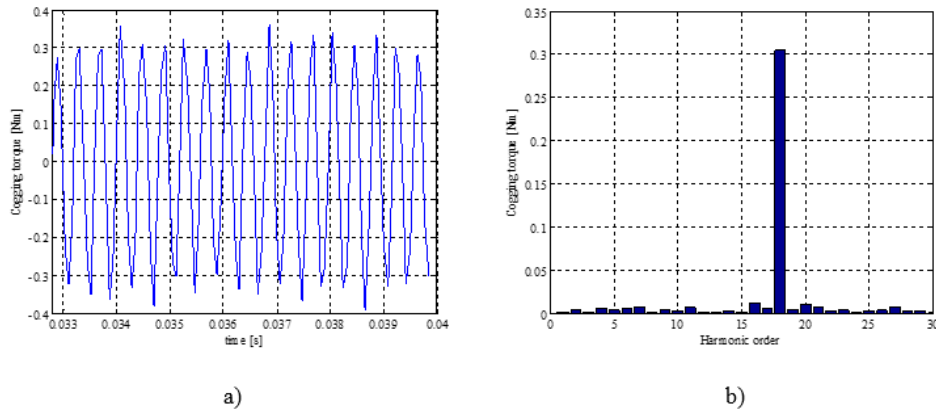


Fig. 3.13. Cogging torque; a) waveform and b) harmonic spectrum. The cogging torque compared with the rated torque of the machine is less than 0.1 % of the rated torque of the machine.

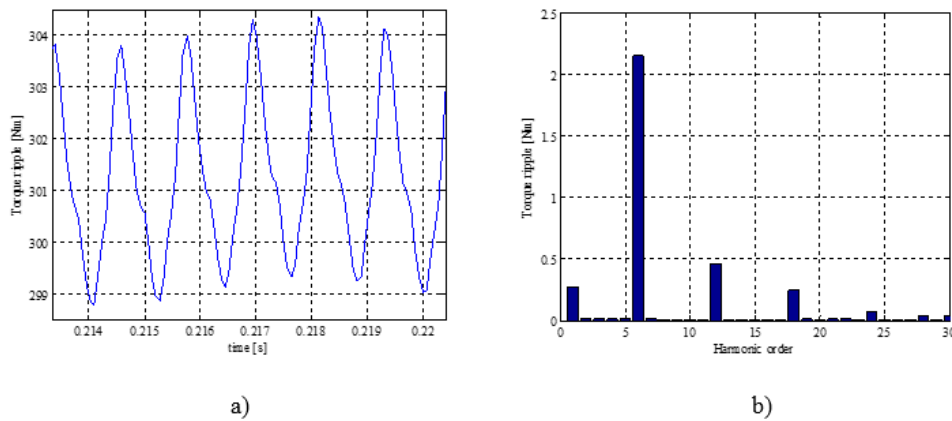


Fig. 3.14. Torque ripple at the rated speed and torque (1.7 % peak to peak); a) waveform and b) harmonic spectrum.

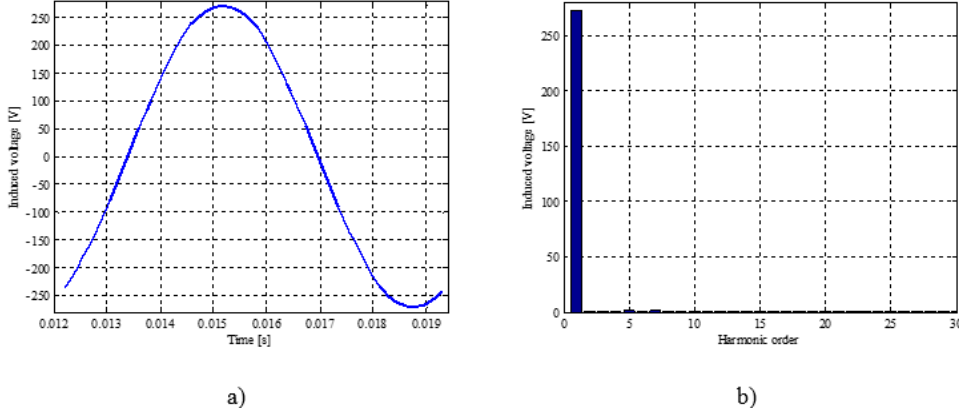


Fig. 3.15. Calculated permanent-magnet-induced voltage at the rated speed at 20 °C; a) waveform and b) harmonic spectrum, the FEA results. THD = 2 %. The induced voltage corresponds to the peak value of 287 V (203 VRMS).

Iron saturation causes harmonic content, which is usually present in tooth-coil machines and thereby influences the behaviour of the inductances (Barcaro et al. 2012), (Yamazaki et al. 2014). Saturation is the natural explanation as the harmonic analysis of the synchronous inductances and flux linkages includes the 6<sup>th</sup> and 12<sup>th</sup> harmonics (Chen et al. 2015). Those components directly affect the torque as it can be seen in the second term of the torque equation

$$T = \frac{3}{2} p \{ \psi_{PM}(\theta) i_q + (L_d(\theta) - L_q(\theta)) i_q i_d \} + T_{cog}. \quad (3.5)$$

The 18<sup>th</sup> harmonic to the torque ripple comes directly from the cogging torque.

### 3.4 Short-circuit test

It is important to control the surviving capability during the short-circuit condition when the machine is designed for traction applications (Choi and Jahns 2013), (Welchko et al. 2003). During symmetrical short-circuit operation, the steady-state values of currents can be calculated by introducing zero values for voltage components and setting the time derivatives in the voltage equations to zero

$$u_{sd} = R_s i_{sd} + L_d \frac{di_{sd}}{dt} - \omega_s L_{sq} i_{sq}, \quad (3.6)$$

$$u_{sq} = R_s i_{sq} + L_q \frac{di_{sq}}{dt} + \omega_s \psi_{PM} + \omega_s L_{sd} i_{sd}. \quad (3.7)$$

If a normal three-phase salient pole PMSM is shorted at standstill and then rotated, the machine axis sustained currents can be calculated from Eqs. (3.6) and (3.7) and substituted into the torque equation to obtain the equation for the short-circuit situation torque

$$i_d = -\frac{\omega_s^2 L_q \psi_{PM}}{\omega_s^2 L_d L_q + R_s^2}, \quad (3.8)$$

$$i_q = -\frac{R_s \omega_s \psi_{PM}}{\omega_s^2 L_d L_q + R_s^2}, \quad (3.9)$$

$$T = \frac{3}{2} p R_s \psi_{PM}^2 \left( \frac{-\omega_s}{\omega_s^2 L_d^2 + R_s^2} + (L_d - L_q) \frac{\omega_s^3 L_q}{(\omega_s^2 L_d L_q + R_s^2)^2} \right). \quad (3.10)$$

The peak torque condition is achieved at the speed

$$\omega_s = \frac{R_s}{\sqrt{L_d L_q}}. \quad (3.11)$$

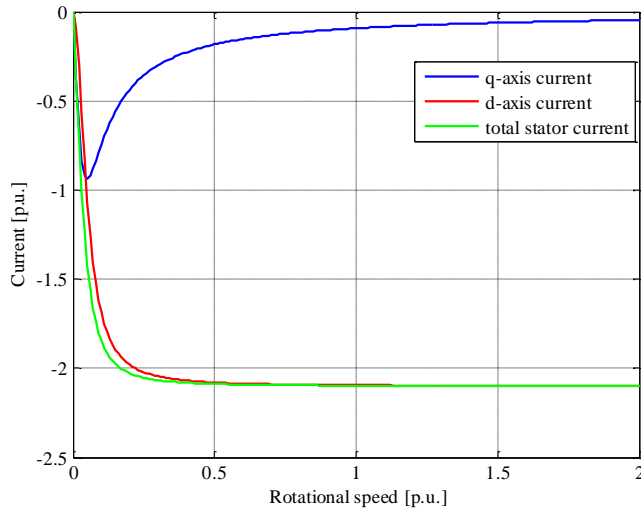


Fig. 3.16. Normalized d- and q-axis currents and the total stator current in the three-phase short-circuit case.

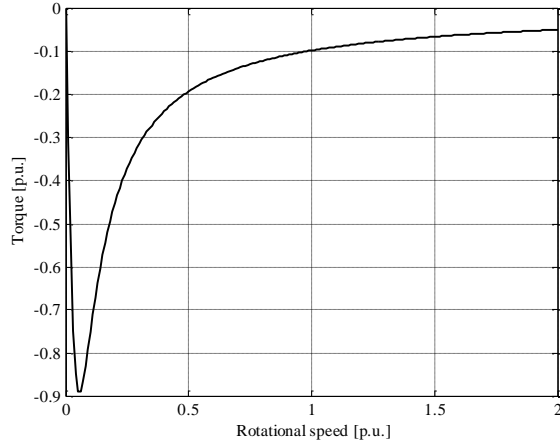


Fig. 3.17. Normalized peak torque in the three-phase short-circuit case. The peak torque value is  $-0.89$  p.u. in the worst case.

FEA-calculated sustained three-phase short-circuit currents are shown in Fig. 3.18 a. The RMS value is 91 A and the peak value 128 A. The synchronous inductance calculated with the induced voltage and this sustained short-circuit current at 140 Hz results in  $L_d = 2.55$  mH. The rated phase voltage and current are 230 V and 67 A, respectively. Therefore, the per-unit synchronous inductance in this short-circuit test is 0.65 pu. This corresponds well to the value given in Fig. 2.6. Figure 3.18 b illustrates the lowest flux density value in a permanent magnet in the worst case.

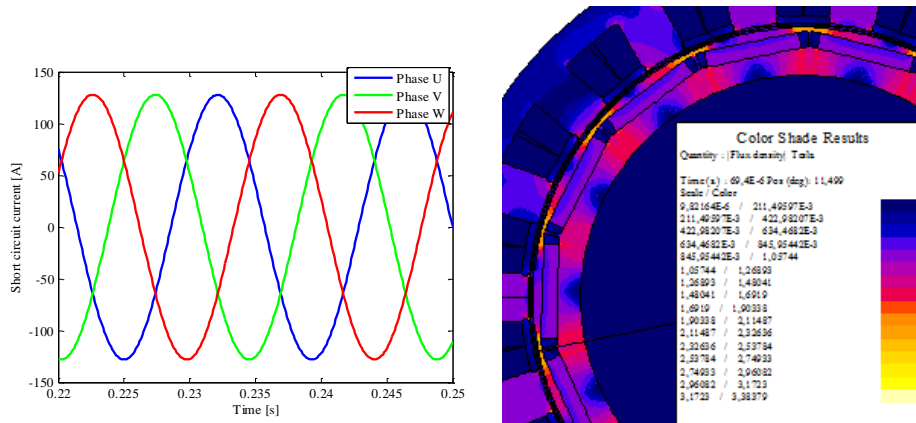


Fig. 3.18. a) Currents in a sustained three-phase short-circuit. The peak current is 128 A and RMS 91 A. b) Flux densities in the magnets in a sudden short-circuit in the worst case. The minimum flux density observed in a magnet remains at about 0.4 T.

### 3.5 Control of the prototype machine

The behaviour of the prototype machine with the methods presented in Chapter 2 is studied and verified. As the PM flux density is so large because of the torque required in this case, the MTPV control is not applied at all. The machine is driven to its voltage limit according to the MTPA, and after that, the FW takes place. Fig. 3.19 presents the prototype in the d-q axis current diagram. One curve takes the saturation into account, and the other assumes the machine parameters constant.

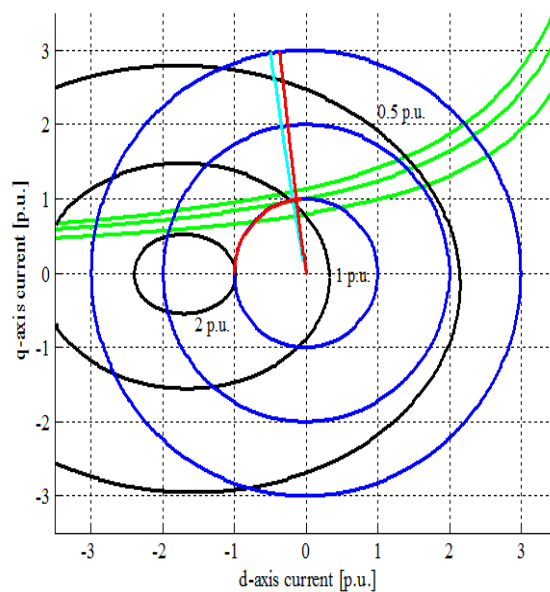


Fig. 3.19. Control of the prototype machine. The red curve represents the case with the saturation included, and the cyan curve the theoretical curve using only the rated parameters.

### 3.6 Mechanical design

For practical reasons, the prototype motor employs direct oil cooling. The planetary gear requires lubrication, which makes the use of the already present manual transmission oil the most cost-effective solution in this case. Indirect water cooling was considered effective enough at higher speeds because of internal oil splashing. Given the potential application of the motor, it was deemed that the cooling of the stator coils has to be secured at lower speeds. It is, after all, in those “the tractor stuck in a muddy field” situations where the maximum torque is needed, and thus, the maximum heat may be generated in the motor.

In this oil cooling concept, the oil is circulated outside the motor for cooling. The cooled oil is pumped back to the motor through eight holes (four on both sides of the stator) in

the upper parts of the frame. The entry points are located so that the coils above the oil level receive fresh oil.

The rotor has a special mechanical structure (Fig. 3.20.); the rotor stack does not have a frame inside it, but the stack is pressed against a plate-like rotor body with long screws and an end plate. The basic idea behind the structure is that the screws and friction within the lamination together provide a core rigid enough to support itself. Preliminary tests on the rotor of the prototype motor have yielded promising results.

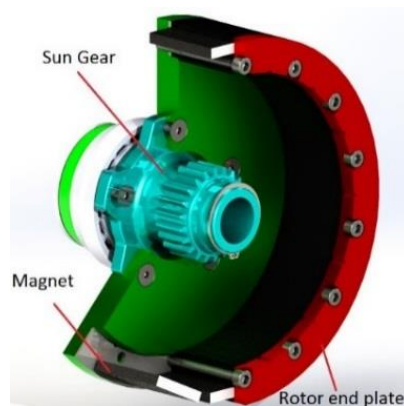


Fig. 3.20. Rotor mechanics.

The mechanical strength of the rotor laminations was calculated; the stress contour is shown in Fig. 3.21. In the stress study at the rated rotational speed of the rotor, the radial force caused by the centrifugal force of the magnets in the point where the magnets are glued to the rotor has to be taken into account. The figure presents the von Mises stress levels obtained by a calculation (Solidworks) in a situation where the maximum torque of approx. 1000 Nm is driven at the rated rotational speed of 1200 min<sup>-1</sup>. A similar evaluation was performed at the maximum speed. The value of the magnetic steel stress is in the range of 320 MPa. The yield strength is 450 MPa.

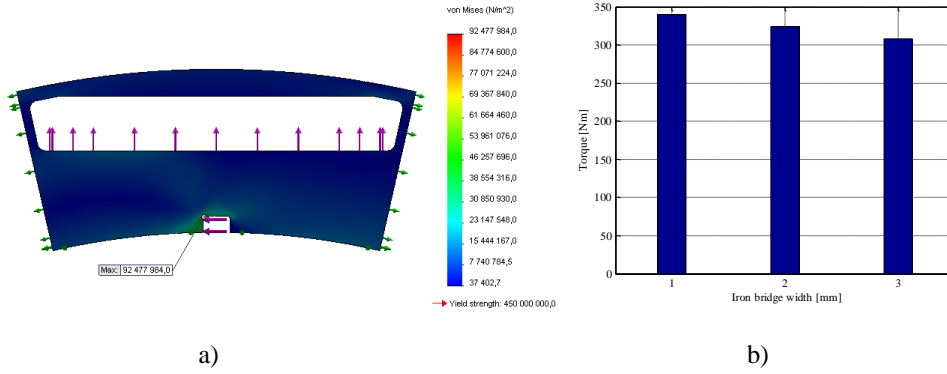


Fig. 3.21. a) Von Mises stress levels at the rotor at maximum torque at the rated speed of  $1200 \text{ min}^{-1}$  and b) electromagnetic torque with the same q-axis current and different widths of iron bridges on the q-axis of the rotor.

The stress values remain at acceptable levels in all cases. The mechanical strength of the rotor against torque and centrifugal forces is thus confirmed. As the rotor has no other frame than the laminated yoke, the tangential shear (caused by motion) between the laminations was prevented by strong split pins and screws shown in Fig. 3.20. Figure 3.21 also shows that the thickness of the iron spokes retaining the rim has a significant effect on the performance of the motor. Obviously, wide bridges increase the permanent magnet leakage flux but strengthen the rotor mechanically. Finally, 2 mm wide iron bridges were manufactured.

### 3.7 Thermal design

A thermal design analysis was performed during the design process. However, it was made without the planetary gearbox as the system would have been too complex to model with it. In this concept, three cooling methods are used. First, oil is dropped on the top of the stator, then, the machine is partly immersed in oil, and finally, when the rotor is rotating, the cooling oil is splashed to the end windings and other parts. This has worked well in the laboratory.

All the heat transfer cases can, at least to a certain degree, be handled by a lumped-parameter thermal model. This means that the partial differential equations can be replaced by a system of linear equations. All the structural parts of electrical machine are of cylindrical form, which enables the use of simplified T-equivalent blocks (Nerg et al. 2008), (Mellor et al. 1991), (Incropera and DeWitt, 1985), and (Rostami et al. 2013). The thermal resistances for conduction and convection can be calculated as follows:

$$R_{\text{cond}} = \frac{l}{\lambda A}, \quad (3.12)$$

$$R_{\text{conv}} = \frac{1}{\alpha A}, \quad (3.13)$$

where  $l$  is the length of the body in the heat flow direction,  $\lambda$  is the thermal conductivity,  $\alpha$  the convection coefficient, and  $A$  is the cross-sectional area. The parameters for the T-equivalent lumped-parameter thermal model can be calculated as presented in Table 3.2. In the table,  $r_1$  is the outer radius,  $r_2$  is the inner radius,  $\lambda_a$  and  $\lambda_r$  are the thermal conductivities in the axial and radial directions, respectively. Figure 3.22 shows how the resistances are connected in the T-elements.

Table 3.2. Parameter calculation of the T-equivalent model for a cylindrical component.

$R$	Axial direction	Radial direction
$R_1$	$\frac{l}{2\pi\lambda_a(r_1^2 - r_2^2)}$	$\frac{1}{4\pi\lambda_r l} \left[ 1 - \frac{2r_2^2 \ln\left(\frac{r_1}{r_2}\right)}{(r_1^2 - r_2^2)} \right]$
$R_2$	$\frac{l}{2\pi\lambda_a(r_1^2 - r_2^2)}$	$\frac{1}{4\pi\lambda_r l} \left[ \frac{2r_1^2 \ln\left(\frac{r_1}{r_2}\right)}{(r_1^2 - r_2^2)} - 1 \right]$
$R_3$	$\frac{-l}{6\pi\lambda_a(r_1^2 - r_2^2)}$	$\frac{-1}{8\pi\lambda_r l(r_1^2 - r_2^2)} \left[ r_1^2 + r_2^2 - \frac{4r_1^2 r_2^2 \ln\left(\frac{r_1}{r_2}\right)}{(r_1^2 - r_2^2)} \right]$

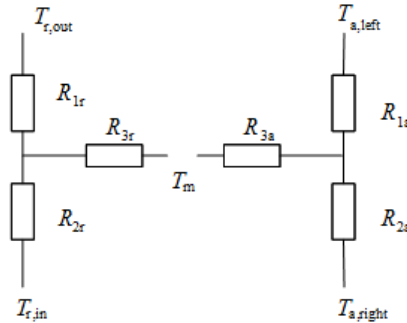


Fig. 3.22 T-element blocks consisting of three thermal resistances both in the axial and radial directions.  $T_m$  denotes the average temperature.

In the steady-state analysis, the temperature rise vector in each node of the thermal network relative to the reference temperature can be calculated by the matrix equation

$$\Delta \mathbf{T} = \mathbf{G}^{-1} \mathbf{P}, \quad (3.14)$$

where  $\mathbf{G}$  is thermal conductance matrix, and  $\mathbf{P}$  is the power loss vector containing the losses in each node. The thermal conductance matrix is defined by the thermal resistances as

$$\mathbf{G} = \begin{bmatrix} \sum_{i=1}^n \frac{1}{R_{1,i}} & -\frac{1}{R_{1,2}} & \cdots & -\frac{1}{R_{1,n}} \\ -\frac{1}{R_{2,1}} & \sum_{i=1}^n \frac{1}{R_{2,i}} & \cdots & -\frac{1}{R_{2,n}} \\ \vdots & \vdots & \ddots & \vdots \\ -\frac{1}{R_{n,1}} & -\frac{1}{R_{n,2}} & \cdots & \sum_{i=1}^n \frac{1}{R_{n,i}} \end{bmatrix}. \quad (3.15)$$

In this oil cooling concept, the oil is circulated outside the motor for filtering and cooling. The cooled oil is pumped back to the motor through eight nozzles (four on both sides of the stator) in the upper parts of the frame. The entry points are placed so that the coils above the oil level receive fresh oil. The worst-case value of oil friction can be evaluated by a sentence assuming the whole air gap filled with oil

$$T_{\text{oil}} = \xi \mu \frac{r S_r v}{\delta} = \xi \mu \frac{r S_r 2\pi r \Omega}{\delta}. \quad (3.16)$$

Here,  $r$  is the radius measured from the rotor centre line to the middle of the air gap,  $S_r$  is the rotor surface area facing the air gap,  $v$  is the velocity of the rotor surface,  $\Omega$  is the rotor mechanical angular velocity,  $\delta$  is the air-gap length, and  $\mu$  is the dynamic viscosity of oil (Stachowiak and Batchelor, 2005). In our case, the machine air gap is only partly filled with oil, and therefore, an appropriate proportion  $\xi \in [0,1]$  of this value will be the practical result. The dimensioning of the planetary gear cogwheels dictates the desired viscosity level. In this case, the surface pressures of the cogwheels remain low, and therefore, for instance automatic transmission gear oil can be used inside the integrated design resulting in acceptable friction losses.

In the calculation, three different oils at the temperature of 100 °C are analysed. This temperature was selected as the manufacturers only give the oil properties at 100 °C. Oils are collected from the website of the oil company Teboil and the datasheets are found in (Konetex 2014). The oil types compared are EP 75W-90 synthetic transmission oil, Hypoid 80W-140 semi-synthetic transmission oil, and Fluid E, which is semi-synthetic automatic transmission oil.

In the case of totally oil-immersed rotor, the results for viscous loss as a function of air-gap length are shown in Fig. 3.23.

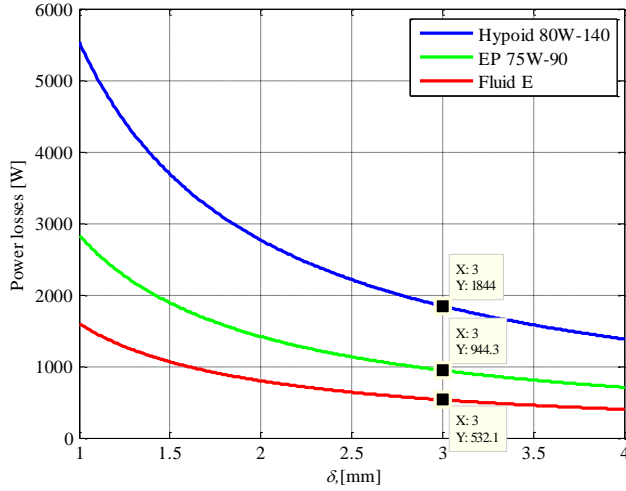


Fig. 3.23. Maximum viscous losses as a function of air-gap length based on Eq. (3.16).

The air-gap length is chosen to be 3 mm because the oil viscous losses are then reasonably low, and it does not excessively degrade the machine electromagnetic efficiency. It can be seen that increasing the air gap any further does not considerably reduce the losses, but more permanent magnets are needed to achieve the same flux density to the air gap, which, in turn, decreases the torque production of the machine. However, the oil friction losses are lower because only one-third of the machine is filled with the lubricating and cooling oil. Estimation of the total mechanical losses at the rated speed is around 300–400 W and 1200–1400 W at the maximum speed.

If bulk magnets are used the permanent magnet losses can be high as a result of eddy currents. Fig. 3.24 shows the amount of eddy current losses in permanent magnets as a function of the number of magnet slices.

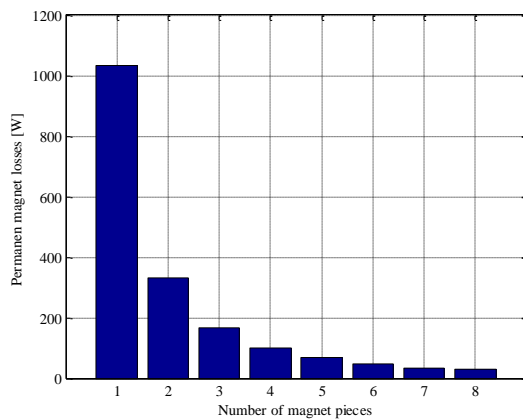


Fig. 3.24. Permanent magnet losses caused by eddy currents as a function of the number of

permanent magnet slices.

The steel lamination retaining the magnets is so thin that some flux density fluctuations take place in the magnets, and therefore, the magnets are manufactured of six galvanically separated slices to limit the PM losses. Bulk magnets cannot be used as they would produce more than 1 kW of PM eddy current losses despite the steel bridge over the magnets. Using six isolated slices reduced the total PM losses to less than 50 W. It can be seen that six magnet slices seem to suffice as the additional reduction in the losses with more than six slices is marginal. Furthermore, it is also possible to use fewer pieces of magnets as the oil cooling ensures heat removal from the machine. Because of oil splashing cooling, the rotor in this machine is actually cooler than the stator because part of the rotor is all the time inside the oil. For further information on direct oil cooling, the reader is referred for instance to (Ponomarev 2013), (Ponomarev et al. 2012).

In the prototype, Shell Spirax (similar to Teboil Fluid E) automatic transmission oil is used for cooling and to lubricate the parts of the planetary gearbox. The most important characteristics are given in Appendix A. Correspondingly, in Table 3.3, the amount and distribution of losses are shown as the LPTN model needs them for the input.

Table 3.3. Losses in the motor in the rated operation calculated analytically and by the 2D FEA.

Loss type	Computed Analytically	Calculated with FEA
Copper [W]	991	991
Stator iron [W]	180	186
Rotor iron [W]	100	103
Magnet loss [W]	50	48
Mechanical [W]	400	-

As it was shown above, the usage of oil causes friction losses, which are minimized by using a low stack length and a large air gap. In that way, Eq. (3.16) gives the highest possible amount of losses. Oil cooling causes more problems if the rotational speed of the motor is high. Therefore, it should only be used in cases where the speed is relatively low and the torque density is high at the same time. The frictional loss of the rotor is directly proportional to the radius and mechanical angular velocity  $r\Omega$ , that is, the peripheral speed. The lubrication of the planetary gear also needs a suitable rotational speed for the cogwheels. Foaming of the oil is also problematic for the lubrication of planetary gearbox.

Fig. 3.25 shows the used lumped-parameter thermal network of the motor.

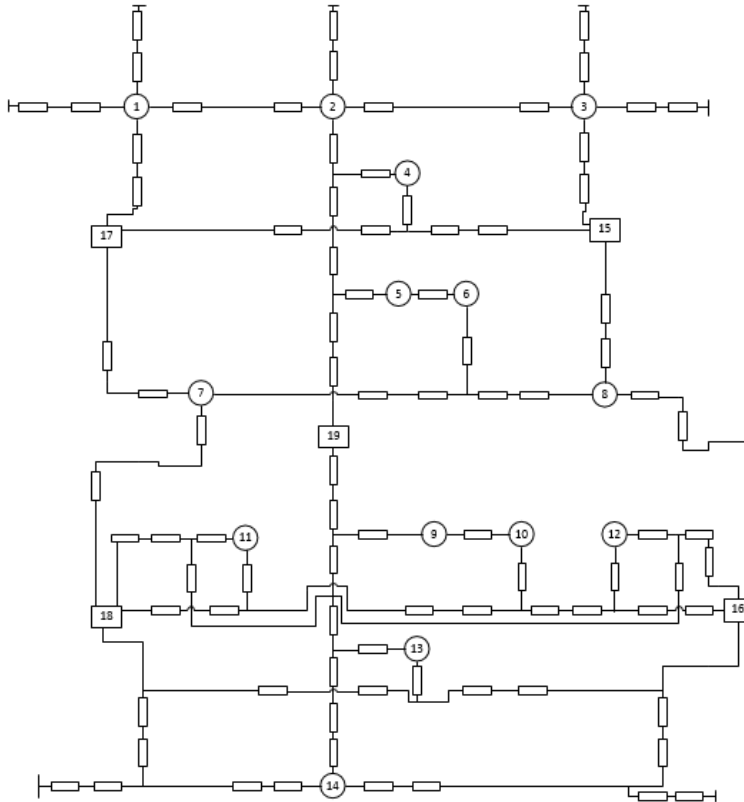


Fig. 3.25. Lumped-parameter thermal network (LPTN) of the PMSM. The rectangular nodes are placed in the cooling matrix as the oil flow is considered in those locations inside the electric machine.

The numbered nodes are as follows

1. Frame left end
2. Frame above stator
3. Frame right end
4. Stator yoke
5. Stator teeth
6. Windings in the stator slot
7. End windings on the left side
8. End windings on the right side
9. Rotor iron
10. Permanent magnets
11. End ring on the left side
12. End ring on the right side
13. Rotor yoke
14. Shaft

15. Area above the right-side end winding
16. Area below the right-side end winding
17. Area above the left-side end winding
18. Area below the left-side end winding
19. Air gap

Fig. 3.26 presents the results when cooling by partial oil immersion is adopted. The lubrication and cooling oil level inside the motor at rest wets 1/2 of the rotor diameter. The temperatures are valid for a situation where the motor is operating at its rated torque at the rated speed and the incoming temperature of the cooling oil is 60 °C. It can be seen that the machine design does not suffer from too high temperatures of permanent magnets or any other active parts.

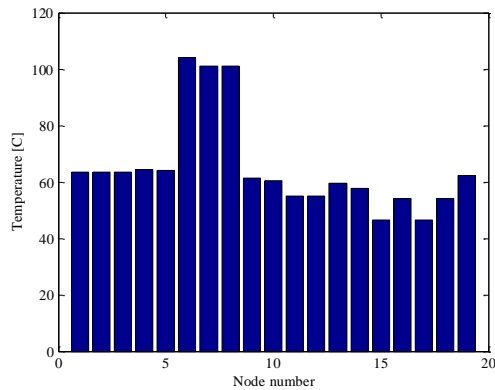


Fig. 3.26. LPTN results for the oil-cooled PMSM. The highest temperatures can be found at windings in the stator slot (6), end windings on the left side (7) and the end windings on the right side (8). The permanent magnets (10) remain at a very moderate temperature of about 60 °C.

### 3.8 Manufacturing a prototype

Based on the analytical and field computations, a prototype machine was manufactured. The main performance parameters are given in Table 3.4, and the main dimensions of the active magnetic parts of the machine are given in Table 3.5.

Table 3.4. Operating parameters of the machine.

<b>Parameter</b>	<b>Value</b>
Rated speed [ $\text{min}^{-1}$ ]	1200
Rated frequency [Hz]	140
Rated line-to-line voltage [V]	400
Rated phase voltage [V]	230
Rated current [A]	67
Rated apparent power [kVA]	45
Rated power factor	0.92
Rated-point efficiency	0.957
Rated mechanical power [kW]	40.8
Rated torque [Nm]	324
Maximum torque [Nm] at 240 A	976
Tangential stress [kPa]	24
Stator resistance [ $\Omega$ , p.u.]	0.0768, 0.02
Induced voltage [V, p.u.]	203, 0.88

Table 3.5. Main magnetic dimensions and winding characteristics of the machine.

Parameter	Value
Stator slots	18
Poles	14
Number of slots per pole and phase	0.43
Length of the stator stack [mm]	75
Length of the rotor stack [mm]	80
Stator outer diameter [mm]	444
Stator inner diameter [mm]	336
Rotor inner diameter [mm]	280
Air-gap length [mm]	3
Number of coil turns in a phase	138
Effective coil turns in a half slot	23
Working harmonic winding factor	0.902
Dimensions of permanent magnet [mm]	$59.5 \times 9.7 \times 13.1$

The target was to achieve as short end windings as possible, Fig. 3.27. The total length of the machine stator including end windings is approx. 130 mm, and the length of the stator stack 75 mm.



Fig. 3.27. Two-layer tooth-coil winding is the shortest possible option to wind the stator of an electrical machine. The winding is compact and slot wedges are used to close the open slots, at the same time guaranteeing that the windings are kept properly in the slots.

The prototype stator is illustrated in Fig. 3.28 and the rotor in Fig. 3.29. The figure shows the very short end windings in the stator, the Pt-100 temperature sensors, and the semi-magnetic slot wedges, which were added to increase the main flux of the machine and to reduce the rotor losses. As it can be seen, the electric motor itself is compact, but the mechanical parts need more space. However, the overall system length is reduced considerably compared with an electric motor and a separate two-step planetary gearbox combination by integrating these two.



Fig. 3.28. Stator after the winding process. Very short end windings are obtained. The slots are closed by semi-magnetic slot wedges.

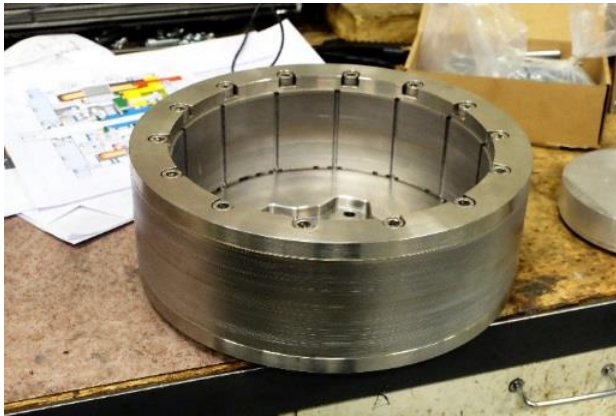


Fig. 3.29. Rotor construction under manufacturing. The smooth air-gap surface guarantees low oil friction losses.

The machine with the mobile cables of the inverter is presented in Fig. 3.30. The overall mass of the prototype is 295 kg, and the mass of the electrical machine only is around 85 kg.



Fig. 3.30. Photograph of the prototype motor.

### 3.9 Summary of Chapter 3

The integrated design of the TCPMSM with a two-stage planetary gearbox was elaborated on. The PMSM rotor is driving the sun. Two clutches are needed to operate gear shifting. The PMSM rotor is either driving the output shaft directly or the planet carrier is connected to the shaft. Two gear ratios 1:1 and 3.64:1 are available. The selection of the gear ratio was based on a commercially available gear, but the gear ratios also meet the required speed–torque range fairly well.

The electromagnetic design of the PMSM was also explicated based on the boundary conditions set by the mechanics and the drive speed–torque needs. The analysis shows that an 18/14 machine is optimal for the given application. Its field weakening range is suitable for this application and its torque quality is very high.

As there is gear-lubricating oil in the chamber, it is used also for the cooling of the machine. Oil is filtered and cooled outside the machine, and it is sprayed on the topmost end windings of the PMSM. The heat transfer was analysed by a lumped parameter model. The viscous losses may be significant, but the analysis shows that a large enough air gap and a moderate peripheral speed of the motor result in an acceptable loss level.

## 4 Additional equipment

This chapter presents the additional equipment needed in the operations of the integrated gear PMSM drive system. The first one is the gear change actuator. This chapter also provides the basic guidelines on the control system that synchronizes the speeds in the gear changing process. The gear change program is built on the MID070S platform and by using the software Guitu and Canto by the Finnish company Exertus (Exertus 2016).

### 4.1 Linear electromagnetic actuator

The dog clutches used in the system need only a small force for operation, mainly for accelerating the clutch moving part. The movement track is also short. In this very case, the moving dog clutch half has to travel a distance of 8 mm. Therefore, an electromagnetic actuator was considered. A desired property of the actuator might also be self-detention at both operating ends to make sure that the dog clutch does not move unintentionally if its control current is lost.

The lack of suitable commercially available equipment for changing gear led to design a special actuator for the purposes of this study. The idea for the gear change mechanism comes from loudspeakers. The “voice coil” actuator has the same operating principle as a loudspeaker voice coil. From here onwards, it is referred to as a linear electromagnetic actuator.

The Lorenz force equation

$$d\mathbf{F} = dQ(\mathbf{E} + \mathbf{v} \times \mathbf{B}) \quad (4.1)$$

explains the operating principle of the voice coil actuator. In Eq. (4.1),  $\mathbf{F}$  is the force vector,  $Q$  is the charge,  $\mathbf{E}$  is the electric field strength vector,  $\mathbf{v}$  is the velocity vector of the moving charge, and  $\mathbf{B}$  is the magnetic flux density vector. Both the electric field and the magnetic field exert a force on a moving charge. In practice, the sentence can be simplified into the form used in the operation of the voice coil as the force caused by the electric field is insignificant in this case:

$$d\mathbf{F} \approx dQ(\mathbf{v} \times \mathbf{B}). \quad (4.2)$$

It is possible to write

$$dQ\mathbf{v} = I d\mathbf{l}, \quad (4.3)$$

where  $I$  is the current and  $d\mathbf{l}$  is the differential conductor length carrying the current. Now, the Lorenz force equation can be written in the form

$$\mathbf{F} = \mathbf{B}I\mathbf{l}. \quad (4.4)$$

This equation shows that a current-carrying conductor that is located in a magnetic field is affected by a force. If the magnetic flux density  $\mathbf{B}$  is produced for instance by a permanent magnet, a counter-acting force will be exerted on it while the current conductor experiences the Lorentz force.

In the linear magnetic actuator of this study, we use this counteracting force. Permanent magnets are glued on the surface of a dog clutch, which is the mover in this application. In the stationary iron part there are a number of coil turns. When current is supplied, the mover starts to make a linear movement produced by the force. In the linear magnetic actuator, as constant radial flux as possible is provided through the coil to avoid eddy current losses in solid parts.

In Fig. 4.1, simplified cross-sectional illustrations of the ring-shaped concentric linear magnetic actuator parts are shown. The figure presents two options: It is possible to arrange the system geometry so that the reluctance force holds the moving part in its end position, or a small holding current can be used to keep the clutch stationary.

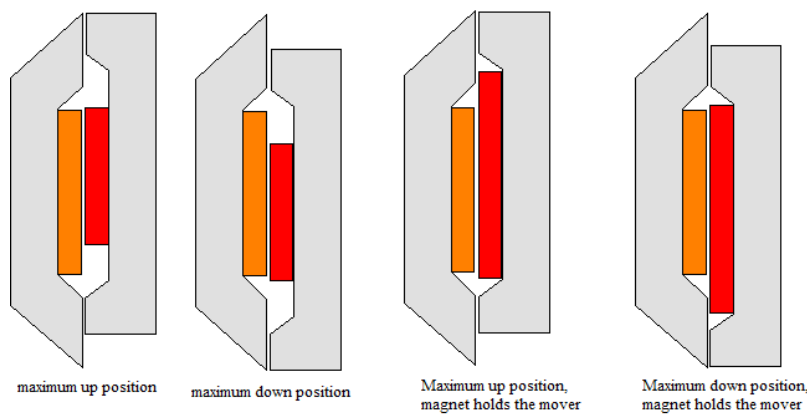


Fig. 4.1. Voice coil clutch actuator. In each figure, the stationary iron part with the coil is located on the left, whereas on the right side there is the moving part containing the permanent magnets.

The design shown in Fig. 4.1 is extraordinary in that the clutch, when engaged, transmits the torque of the motor and is, at the same time, rotating at the same speed as the shaft. It is possible to design this kind of a rotating low-loss clutch linear actuator when the whole magnet surface is uniform. No significant eddy current losses are produced by rotation when uniform magnetization through the magnet is obtained.

With this kind of a configuration, relatively high forces and linear movements can be obtained by parts that are also rotating at the same time. This seems not possible with commercially available devices, and thus, this could be the solution also for many other applications.

Fig. 4.2 presents the overall construction of the voice coil actuator.



Fig. 4.2. 3D model of the actuator that works on the voice coil principle.

In Fig. 4.2, the green section is the moving clutch part with surface-mounted magnets. The purple section is the stationary iron part, which has the coil on its inner surface.

A magnetostatic FEA is made to verify the analytical calculation. In Fig. 4.3, the equivalent magnetic flux lines and the flux density surface are shown at no load supplied with zero current. The mover is in its end position. The overall distance that the clutch has to move is 8 mm.

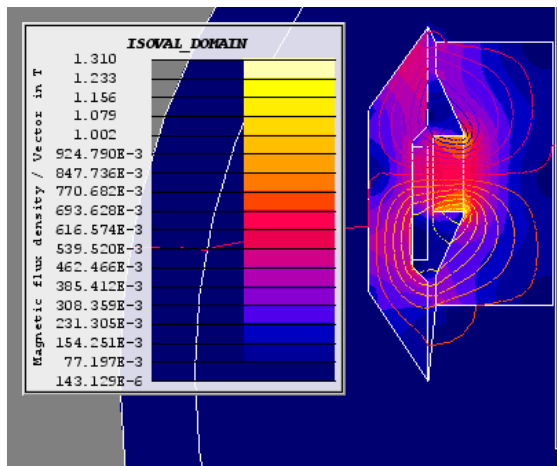


Fig. 4.3. Magnetic flux lines and the flux density surface when the coil is supplied with zero current. The reluctance differences at the ends provide the self-retaining property without holding current.

In this case, the permanent magnet produces reluctance force, and the mover is held in this position if no negative current is supplied. The magnetic flux density waveform in the middle of the air gap is shown in Fig. 4.4.

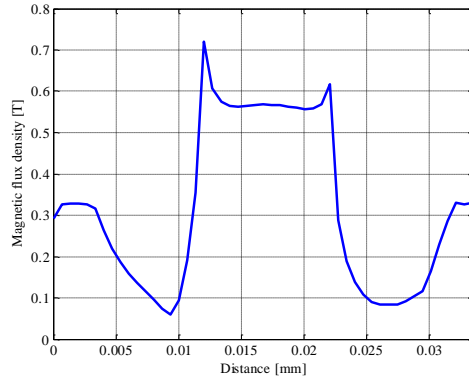


Fig. 4.4. No-load flux density waveform in the middle of the air gap along the length of the actuator corresponding to the position shown in Fig. 4.3.

The total force of the linear magnetic actuator is approx. 120 N, and the reluctance force in the end positions is 35 N. This suffices to hold to mover at both ends, but 10 % of the total current is reserved for holding to ensure the holding performance in all conditions.

## 4.2 Rotor position sensing

Many sensorless methods have been developed for PMSM control (Song et al. 2016). There are back-EMF methods (Cui et al. 2015), which cannot be used accurately in the lowest speed area and also signal injection-based methods (Cupertino et al. 2011), which work in a low-speed area but suffer from cross-saturation and secondary saliency problems. Therefore, mechanical sensors such as encoders and resolvers are the most commonly used position sensors in traction drive applications.

It is important to know the rotor position in the system especially in a low-speed large-torque situation. In that case, the converter must know the position of the magnetic d-axis accurately as the machine has to deliver very high torques. In this case, the resolver was adopted.

This prototype motor system also needs another speed sensor to match the speeds between the rotor and the output shaft. This sensor is mounted on the shaft.

## 4.3 Overall system control

In this machine, the control of the gear change is a highly important issue. The electrical machine itself is controlled by an inverter with the algorithms presented in Chapter 2. The overall control logic is illustrated in Fig. 4.5.

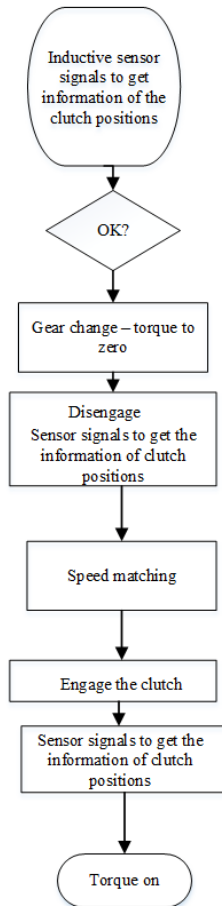


Fig. 4.5. Overall control logic of the integrated hub gear motor.

In Fig. 4.5, the control logic is shown. The process from top to bottom consists of the following steps: Sensor signals of the clutch positions are supplied to the MID070S mother board. If the reduction gear is to be engaged, the torque of the motor is first driven to zero. Then, the direct gear is disengaged with the maximum current through the voice coil PWM supply unit, and the sensor gives the position signal telling that the clutch is in the 'open' state. After that, the control logic reads the rotational speed of the reduction gear, and the motor inverter matches the speed of the motor to the desired speed. Obviously, there has to be a speed difference (approx.  $10\text{--}20\text{ min}^{-1}$ ) so that the teeth of the clutch and the sun gear can correctly mesh with one another. Next, the reduction clutch is engaged. Again, the maximum current is supplied to the actuator through the PWM unit. When the position sensor indicates that the reduction clutch is in the 'closed' state, the PWM unit supplies 10 % of the maximum current to ensure that the clutch will definitely be closed in all special cases. Then, torque is applied to the motor. The very

same procedure is also performed when the direct gear is changed. Figure 4.6 shows the behaviour of the currents in the operating states of the gear changing process.

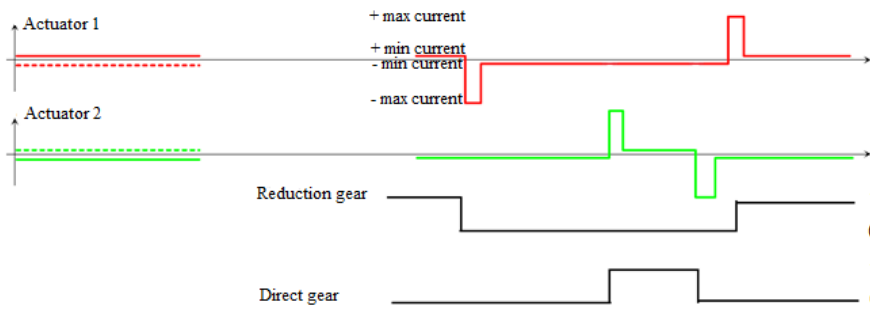


Fig. 4.6. Principle of the gear changing process.

#### 4.4 Summary of Chapter 4

The integrated gear motor design relies on smooth operation of two mechanical dog clutches. Electromagnetic actuators can be used to engage and disengage the dog clutches, which need low forces for operation. To this end, accurate speed control is needed to synchronize the mechanical parts before operating a clutch. To operate the clutches, fast actuators are required. As suitable commercial actuators were not available, an electromagnetic actuator design was developed for the purpose and reported in this chapter. The control principles of the actuators were discussed in brief.

## 5 Measurements

This chapter presents the experimental results and verifies the properties and performance of the prototype motor. The schematic of the measurement bench arrangements is given in Fig. 5.1. It includes a cooling circuit, a data acquisition system, and mechanical and electrical power transmissions.

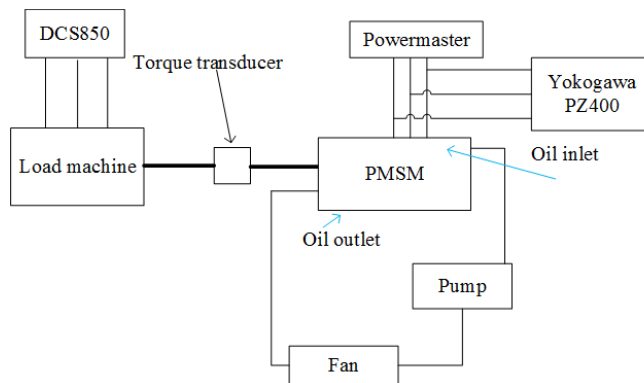


Fig. 5.1. Schematic of the measurement setup.

A photograph of the measurement setup is shown in Fig. 5.2. The test PMSM with an integrated two-speed planetary gearbox is driven as a motor and supplied by a Visedo 250 kW Powermaster frequency converter. A large 480 kW,  $1590 \text{ min}^{-1}$  DC machine, used as a load, was controlled by an ABB DCS850 converter.

The oil circulation unit uses a 550 W pump, and the cooling unit for the oil uses a 750 W induction machine to rotate the fan. The oil level in the measurements was adjusted so that half of the standing motor was filled with oil. The oil flow rate during operation was set to 3–5 l/min. The traditional input–output measurement method was applied in the experimental tests.

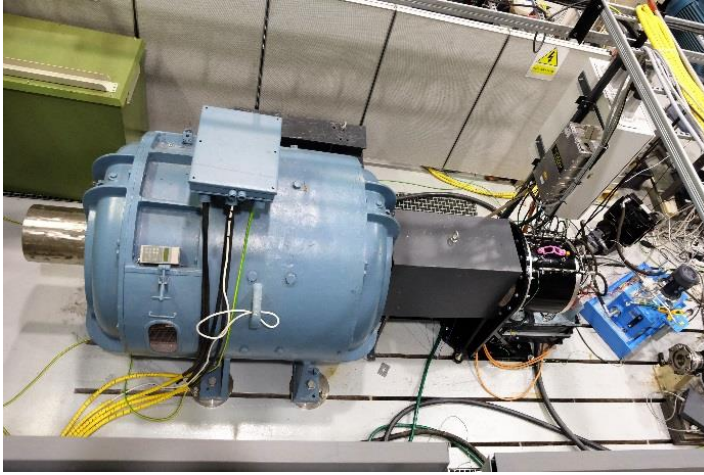


Fig. 5.2. Test setup in the laboratory. The large blue DC machine on the left is used to load the integrated PMSM (black machine on the right). The oil-cooling laboratory system is seen on the right.

Figure 5.3 presents the permanent-magnet-induced voltage at the rated speed of  $1200 \text{ min}^{-1}$  at room temperature ( $20 \text{ }^\circ\text{C}$ ) when the PMSM was driven at no load as a generator. As can be seen, the back-emf waveform is purely sinusoidal because of the extraordinary winding configuration (there are always two coils of one phase next to each other and one coil apart, Figs. 3.10 and 3.11). This further promises a very good efficiency; it is somewhat better than the calculated value as the magnet material remanent flux density of  $1.2 \text{ T}$  is slightly better than the magnet used in the calculations.

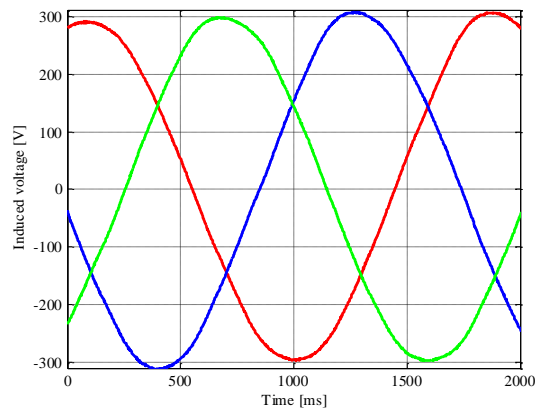


Fig. 5.3. Measured no-load voltage waveform from three phases of the machine at 1 p.u. speed.

In Fig. 5.4, the winding temperatures are shown in three different loading states. Three individual Pt-100 temperature sensors were installed for each phase in the same locations;

both at the D- and N-ends and in the middle of the slot. The differences between the temperatures can be explained by the fact that the sensors of the windings in different phases are located in different places when considering the oil inlet so that the cooling will have an immediate effect.

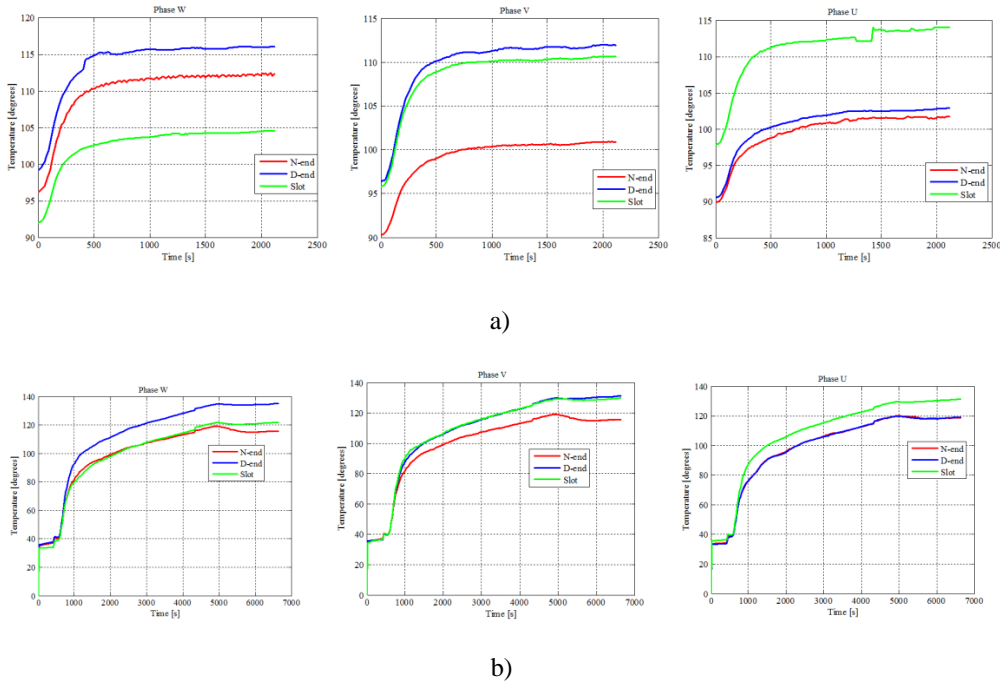


Figure 5.4. Measured temperature in the end winding and in the slot; a) temperature at the rated power at the rated speed of  $1200 \text{ min}^{-1}$ ,  $330 \text{ Nm}$  and b) temperature at the  $1.5 \text{ p.u.}$  torque and at the  $0.4 \text{ p.u.}$  speed. U, W, and V are the phases where the sensors are installed.

The temperature measurements show that there is temperature reserve left in this PMSM at the rated load. It was tested that the machine can be driven continuously at  $50 \text{ kW}$  at its rated speed. Thus, the combination of oil immersion and oil drop cooling suffices to keep the winding temperature below the thermal limit of the insulation in this kind of a heavy-duty application. The temperature of the permanent magnets is not problematic in this case as they are partly below the oil level all the time. This was proven by the thermal analysis in this doctoral dissertation. To sum up, the oil flow is sufficient to keep the winding temperature below the thermal limit.

Naturally, when the application of working machines is considered, ambient temperatures can be even above  $50 \text{ }^\circ\text{C}$ ; on the other hand, conditions can be very cold. One can see from the measured temperatures that there is still clear temperature reserve left. The highest temperatures that can be tolerated by the machine components are around  $155 \text{ }^\circ\text{C}$  as the PM and the insulation are manufactured to tolerate that temperature.

The efficiency map measurement of the motor with the gear installed and with the gear removed was carried out. The difference in these measurements indicates the extra oil friction caused by the non-operating gear system. Figure 5.5 shows the efficiency measurements in both cases and the efficiency difference caused by the gear friction with gear not engaged.

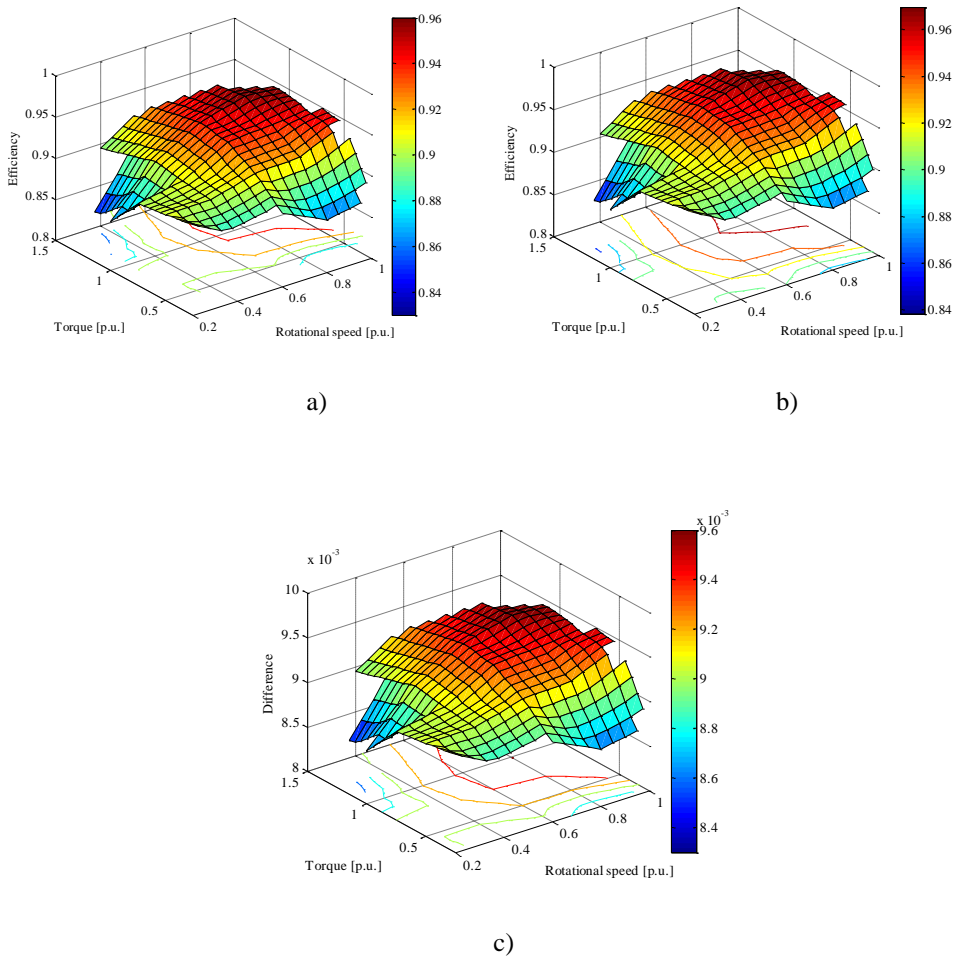


Fig. 5.5. Measured efficiency map a) with the planetary gearbox installed but rotating freely and b) with the planetary gearbox totally removed. c) Efficiency difference caused by the friction loss of the gear (difference of a) and b)).

The gear efficiency is of interest; thus, the efficiency map of the drive system with the gear engaged was measured next. Figure 5.6 illustrates this result, compares the efficiencies of the direct drive (Fig 5.5 a)) and the gear-engaged system (Fig. 5.6 a)), and gives the difference in Figure 5.6 b). As a result, it is possible to decide that the planetary gear in this case reduces the efficiency of the system by about 0.5 % when engaged.

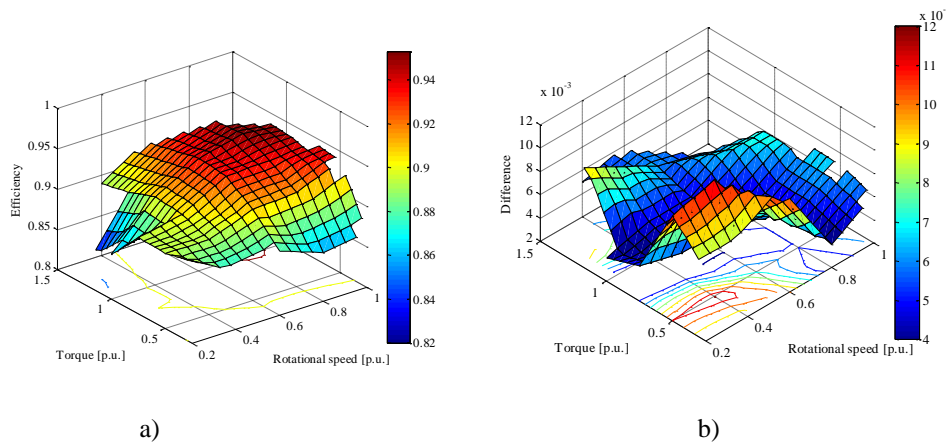


Fig. 5.6 a) Measured efficiency map with power travelling through the gear and b) difference compared with Fig. 5.5 a) (the efficiency reduction caused by the gear transmission)

The loss components from the measurements are collected in Table 5.1. These losses have been measured from the no-load power but cannot be experimentally divided into separate parts. Permanent magnet eddy current losses are negligible at no load. The division between the iron losses and the oil friction losses is made based on the FEA calculation results for the iron losses and assuming that all other losses of the total losses come from oil friction. The chamber is half filled. Using  $\xi = 0.5$  gives oils friction of 266 W. The sum of no load losses is then about 600 W, which is more than the measured no-load loss. It is obvious that the proportion of the wetted rotor surface may be lower than  $\xi = 0.5$ , which could explain the higher calculated loss.

Table 5.1 Power loss components

Losses [W]	Calculated	Measured
Iron losses (incl.PM)	326	-
Oil friction losses	$\xi \times 531 = 266$	-
No-load losses	-	520
Stator Joule losses	991	980

In Table 5.2, the design parameters and the measured parameter values are given. A good correlation between the parameters was achieved. The induced voltage of the prototype was slightly higher because of the PM with a higher remanent flux density than that of the material used in the calculations.

Table 5.2 Comparison of the design and measured parameters.

Parameter	Calculated	Measured
Rated current [A]	67	68
Induced voltage [V]	203	209
Resistance [ $\Omega$ , p.u.]	0.0768	0.078
d-axis synchronous inductance [mH, p.u.]	2.5 0.65	2.5 0.65
Rated torque [Nm]	324	330

The torque as a function of the rotational speed of the machine is given in Fig. 5.7. The figure focuses on the field weakening properties of the machine. At the same time, the figure shows that the required overload capability is achieved.

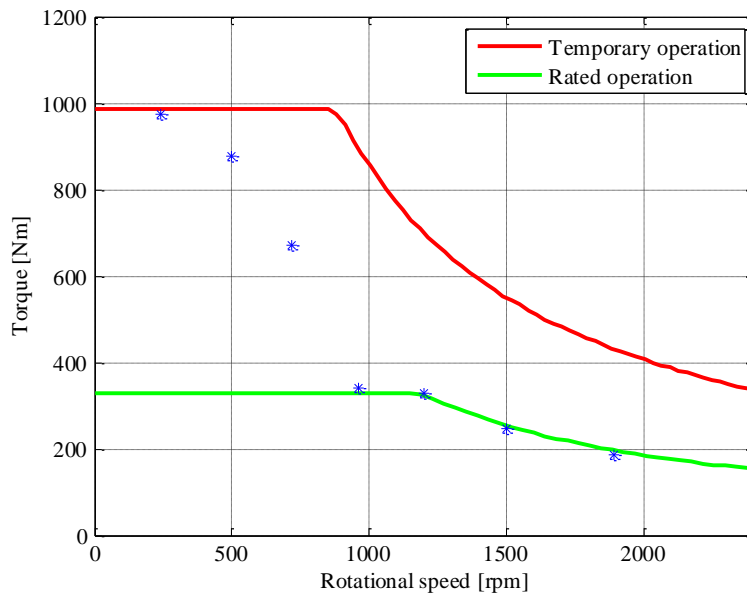


Fig. 5.7. Torque curve as a function of rotational speed. The measured points are indicated by \*.

## 5.1 Summary of Chapter 5

The integrated motor–gear system was tested in the laboratory. The design parameters were confirmed. The cooling effectiveness of the system was verified. The motor efficiency at different operating points is very important from the viewpoint of the overall

energy efficiency of an electric traction system. The 18/14 PMSM design was shown to be very efficient in all operating areas.

Some attempts were made to analyse the efficiency of the planetary gear itself. The measurements show that the gear efficiency is high, and about 1% of power is lost at the maximum in the gear.

## 6 Conclusions

Electric traction systems for heavy machinery were studied. An electric traction motor in off-road vehicles has to meet challenging demands. The motor drive system should be capable of producing very high traction forces in difficult terrain operations at the lowest operating speeds, and maybe the same machine should be capable of travelling 40–50 km/h on the road.

Traditionally, off-road machinery has been driven with an internal combustion engine and a gearbox offering all the required speed ranges for the vehicle with multiple gear ratios. For example, an agricultural tractor can run at 0.4 km/h with the lowest creeping gear at the rated ICE rotating speed and at 40 km/h with the highest gear. The speed range is 1:100. In principle, also the torque range is thus 100:1. In practice, such a torque range is not applicable as the wheel-terrain friction cannot transfer forces produced by the lowest gear in theory. It is aimed only at producing the low operating speed for the tractor because the ICE cannot be driven at speeds lower than the idling speed. The speed range of a typical off-road diesel engine is between 800 min<sup>-1</sup> idling and 2500 min<sup>-1</sup> maximum rotational speed. The practical operating speed varies between 1000 and 2000 min<sup>-1</sup> while the practical operating speed of an electrical motor varies for instance between 0 and 2500 min<sup>-1</sup>. Such a motor does not need a similar gear system as the competing ICE.

A correctly designed and efficiently cooled electrical traction motor can produce its rated torque already at the zero speed guaranteeing its off-road machine also the lowest speed range without excessive gear ratios as in an ICE drive. In this work, the option of using the simplest possible gearbox, a two-step planetary gear, in conjunction with a correctly chosen permanent-magnet synchronous machine for heavy machinery traction applications has been studied.

The work studies first the boundary conditions set on a traction motor drive system. To be able to compete with an ICE drive system with multiple gears, it is obvious that at least these two gear ratios are needed. A planetary gear offers gear ratios typically in the range of 1:4 while 1:10 is a practical minimum. At the beginning of the work it was found that a gear ratio in the range of 1:4 (1:3.63 in practice) is fairly suitable for the case under study. If the electric traction motor can be temporarily overloaded with three times its rated torque and if the same machine can go to twice the rated speed still producing its rated power at 50% of the rated torque, the speed and torque ranges of the drive system will be 1:24, and vice versa. As the electric machine is offering torque from zero speed, these ratios should suffice for off-road machinery drives.

After these intermediate conclusions, it was obvious that an electric motor meeting the required torque and speed ranges should be found. Three times the rated torque during low-speed operation results in nine times the rated Joule losses in the stator winding, and therefore, efficient cooling for the machine is needed.

Thus, the machine was cooled by partly immersing it in lubrication and cooling oil, partly splashing the same oil with the rotating rotor and the gear system, and injecting oil onto the upper end windings of the machine. The oil itself is filtered and cooled outside the motor enabling efficient protection for both the gear and the electric motor.

Special attention was paid to select the right motor type of all possible permanent magnet synchronous machines. As there is always a need to minimize the size of any traction apparatus, the motor should have a plurality of poles to make its yoke as thin as possible thus enabling the lowest possible outer diameter for the gear system. Fortunately, a PMSM does not suffer from a high number of poles similarly as an induction motor does, and its performance can be excellent also in the case of a large number of poles in a low-power small machine.

The traction motor should also have a suitably high synchronous inductance enabling an adequate field weakening range and also heavy overloadability without excessive saturation caused by armature reaction. In this case, a design with a synchronous inductance division 50/50 by magnetizing inductance and leakage inductance was selected. It was also shown that the 18/14 machine delivers a smooth torque in a wide operating range, and it was thus selected as the motor type for the purpose. The operating modes of a PMSM in different operating conditions were re-evaluated during the work: the MTPA, field weakening, and MTPV modes were studied.

The inductance behaviour of the motor was also studied in detail to be able to control the motor in the best possible ways. As there is a need for heavy overloading, the inductance behaviour must be studied in a more thorough way than in the case of an industrial S1 motor.

An analysis of the thermal behaviour of the motor was also one of the important elements of the work. The traditional lumped-parameter method was used here as it was found to be the most reliable approach in addition to the measurement results. There are, however, additional aspects in the analysis of the thermal behaviour as the oil splashing with a semi-filled compartment is one of the most difficult cases to be evaluated accurately.

A lot of iterative design effort was put into the system engineering approach to optimize the motor with the two-step planetary gearbox, cooling, and lubrication systems. The mechanical features enabling the thinnest possible rotor were found with a design approach where the rotor active parts also act as the rotor mechanical parts.

The gearbox system also needs a gear-shifting arrangement. To this end, various actuators starting from stepper motor drives and solenoid arrangements were studied, yet no final solution was found. Finally, a novel actuator based directly on the Lorentz force was constructed. A contactless actuator is capable of engaging and disengaging the dog clutch halves used in the gear shifting. The rotating part of the clutch actuator has permanent

magnets, and the stationary part of the actuator has a voice coil enabling well-controlled eight millimetre movement of the dog clutch mover in both axial directions.

As a result of the research and engineering work, a new integrated design was developed, built, and tested in the laboratory. The 18-slot 14-pole tooth-coil machine designed and manufactured in the study showed to have excellent properties for the purpose. Its torque production capability is high, the torque quality is good, and the oil-cooling performance excellent. The construction was made thin enabling a low overall diameter for the whole traction drive system.

The tests with the gear-shifting system showed that the gear changing can be efficiently handled without pneumatics, hydraulics, or sliding clutch arms. The gear changing mechanism proved to be fast and reliable.

The work covers the main features of designing an integrated traction motor gear system for off-road machinery. The work provides a good basis for future development of a modern electric traction system.

## **6.1 Suggestions for future work**

The doctoral dissertation is mostly based on straightforward engineering work, and maybe lacks in-depth analyses of various issues. There are several topics whose scientific depth could be significantly improved; for instance, the actual behaviour of the motor developed in the dynamic control should be modelled more accurately. The applicability of the incremental inductances in the machine control should be studied in more detail.

There is also a need to deepen the thermal behaviour analysis and the fluid dynamic studies of the motor system. The complicated mechanical structure of the system is a challenging task for anyone willing to fully understand the fluid dynamics of the integrated design.

There are also practical design needs for the system. The cooling solution used in the laboratory setup is far from a practical heavy-duty off-road working machine application, and should be redesigned to have oil circulation so that no additional oil tank is needed. The motor must run all the time with the same amount of oil so that no oil level control is needed.

A combined simulation tool including the electromagnetic, mechanical, and thermal behaviour of the drive system could be developed. A comprehensive virtual design tool is needed. The dynamics of the gear shifting could then be studied in more detail. Furthermore, the present gear shifting process automation requires position sensors for the dog clutch. Novel design ideas are needed to eliminate extra sensors. It might be possible to redesign the actuator so that its position could be estimated from the voltage and current signals of the main coil itself.

The design is now protected with two patent applications (see Section 1.6.). A step further could be to develop the integrated design into an actual innovation and commercialize the ideas presented in this study.

## References

- Ahokas, J., Traktorit ja työkoneet [Tractors and working machines, in Finnish], [Online] <http://www.energia-akatemia.fi/attachments/article/54/TraktoritJaTyokoneet.pdf>, [Accessed 7 September 2016].
- Alberti, L., Barcaro, M., and Bianchi, N., “Design of a Low-Torque-Ripple Fractional-Slot Interior Permanent-Magnet Motor,” *IEEE Transactions on Industry Applications*, vol. 50, no. 3, May–June 2014, pp.1801–1808.
- Azar, Z., Zhu, Z.Q., and Ombach, G., “Influence of Electric Loading and Magnetic Saturation on Cogging Torque, Back-EMF and Torque Ripple of PM Machines,” *IEEE Transactions on Magnetics*, vol. 48, no. 10, Oct. 2012, pp. 2650–2658.
- Barcaro, M., Bianchi, N., and Magnussen, F., “Remarks on Torque Estimation Accuracy in Fractional-Slot Permanent-Magnet Motors,” *IEEE Transactions on Industrial Electronics*, vol. 59, no. 6, 2012. pp. 2565–2572.
- Bertotti, G., “General properties of power losses in soft ferromagnetic materials,” *IEEE Transactions on Magnetics*, vol. 24, no. 1, 1988. pp. 621–630.
- Bianchi, N. and Bolognani, S., “Design techniques for reducing the cogging torque in surface-mounted PM motors,” *IEEE Transactions on Industry Applications*, vol. 38, no. 5, September/October 2002, pp. 1259–1265.
- Bianchi, N., Fornasiero, E., and Soong, W., “Optimal selection of PM flux linkage in a PM assisted synchronous reluctance machine,” in *21st International Conference on Electrical Machines (ICEM)*, 2–5 September 2014, pp. 1341–1347.
- Bilgin, B., Emadi, A., and Krishnamurthy, M., “Design considerations for switched reluctance machines with a higher number of rotor poles,” *IEEE Transactions on Industrial Electronics*, vol. 59, no. 10, Oct. 2012, pp. 3745–3756.
- Boldea, I., Tutelea, L.N., Parsa, L., and Dorrell, D., “Automotive Electric Propulsion Systems With Reduced or No Permanent Magnets: An Overview,” *IEEE Transactions on Industrial Electronics*, vol. 61, no. 10, Oct. 2014, pp. 5696–5711.
- Chen, X., Wang, J., Sen, B., Lazari, P., and Sun, S.A., “High-Fidelity, Computationally Efficient Model for Interior Permanent Magnet Machines Considering the Magnetic Saturation, Spatial Harmonics and Iron Loss Effect,” *IEEE Transactions on Industrial Electronics*, , vol. 62, no. 7, 2015, pp. 4044–4055.
- Choi, G. and Jahns, T. M., “Interior Permanent Magnet Synchronous Machine Rotor Demagnetization Characteristics under Fault Conditions,” in *2013 IEEE Energy Conversion Congress and Exposition*, pp. 2500–2507, 15–19 September 2013, Colorado, Denver, USA.

---

Cui, C., Liu, G., Wang, K., and Song, X., “Sensorless drive for high-speed brushless DC motor based on the virtual neutral voltage,” *IEEE Transactions on Power Electronics*, vol. 30, no. 6, June 2015, pp. 3275–3285.

Cupertino, F., Giangrande, P., Pellegrino, G., and Luigi, S., “End effects in linear tubular motors and compensated position sensorless control based on pulsating voltage injection,” *IEEE Transactions on Industrial Electronics*, vol. 58, no. 2, Feb. 2011, pp. 494–502.

De Santiago, J., Bernhoff, H., Ekergård, B., Eriksson, S., Ferhatovic, S., Waters, R., Leijon, M., “Electrical Motor Drivelines in Commercial All-Electric Vehicles: A Review,” *IEEE Transactions on Vehicular Technology*, vol. 61, no. 2, Feb. 2012. pp. 475–484.

Di Barba, P., Bonislowski, M., Palka, R., “Design of Hybrid Excited Synchronous Machine for Electrical Vehicles,” *IEEE Transactions on Magnetics*, vol. 51, no. 8, August 2015.

Dorrell, D. G., Hsieh, M.-F., Popescu, M., Evans, L., Staton, D. A., and Grout, V., “A review of the design issues and techniques for radial-flux brushless surface and internal rare-earth permanent-magnet motors,” *IEEE Transactions on Industrial Electronics*, vol. 58, no. 9, Sep. 2011, pp. 3741–3757.

Dutta, R., Chong, L., Rahman, M. F., “Design and Experimental Verification of an 18-Slot/14-pole Fractional-Slot Concentrated Winding Interior Permanent Magnet Machine,” *IEEE Transactions on Energy Conversion*, vol. 28, no. 1, March 2013, pp. 181–190.

Eclipse Magnetics, *Sintered Neodymium Iron Boron (NdFeB) Magnets*, [Online], Available from [http://www.eclipsemagnetics.com/media/wysiwyg/brochures/neodymium\\_grades\\_data.pdf](http://www.eclipsemagnetics.com/media/wysiwyg/brochures/neodymium_grades_data.pdf). [Accessed 31 January, 2016].

El-Refaie, A. M., “Fractional-Slot Concentrated-Windings Synchronous Permanent Magnet Machines: Opportunities and Challenges,” *IEEE Transactions on Industrial Electronics*, vol. 57, no. 1, January, 2010, pp. 107–121.

Emadi, A., Lee, Y. J., Rajashakera, K., “Power Electronics and Motor Drives in Electric, Hybrid Electric and Plug-In Hybrid Electric Vehicles,” *IEEE Transactions on Industrial Electronics*, vol. 56, no. 6, June, 2008, pp. 2237–2245.

Exertus, [Online], Available from <http://www.exertus.fi/> [Accessed 15 March, 2016].

Finken, T., Felden, M., and Hameyer, K., “Comparison and Design of Different Electrical Machine Types Regarding Their Applicability in Hybrid Electric Vehicles,” in

*Proceedings of the 2008 international conference on electrical machines*, 6–9 September 2008, Villamoura, Portugal.

Galioto, S. J., Reddy, P. B., El-Refaie, A. M., and Alexander, J. P., “Effect of magnet types on performance of high-speed spoke interior permanent-magnet machines designed for traction applications,” *IEEE Transactions on Industry Applications*, vol. 51, no. 3, May 2015, pp. 2148–2160.

Gasparin, L., Cernigoj, A., Markic, S., and Fiser, R., “Additional Cogging Torque Components in Permanent-Magnet Motors Due to Manufacturing Imperfections,” *IEEE Transactions on Magnetics*, pp. vol. 45, no. 3, March 2009, pp. 1210–1213.

Guglielmi, P., Boazzo, B., Armando, E., Pellegrino, G., and Vagati, A., “Permanent-Magnet Minimization in PM-Assisted Synchronous Reluctance Motors for Wide Speed Range,” *IEEE Transactions on Industry Applications*, vol. 49, no. 1, January/February 2013, pp. 31–41.

Haataja, J. (2003), *A comparative performance study of four-pole induction motors and synchronous reluctance motors in variable speed drives*, Doctoral dissertation, Acta Universitatis Lappeenrantaensis 153, Lappeenranta University of Technology.

Hao, L., Isaac Du, H. Y., Lin, H., and Namuduri, C., “Design and Analysis of PM Fractional Slot Machine Considering the Fault Operation,” *IEEE Transactions on Industry Applications*, vol. 50, no. 1, January/February 2014, pp. 234–243.

Ilioudis, V. C., Margaris, N. I., “Flux Weakening Method for Sensorless PMSM Control Using Torque Decoupling Technique,” *First symposium on Sensorless Control for Electrical Drives*, Thessaloniki, Greece, July 9–10, 2010, Padova, Italy, pp. 32–39

Immonen, P. (2013), *Energy Efficiency of a Diesel-Electric Mobile Working Machine*, Doctoral dissertation, Acta Universitatis Lappeenrantaensis 518, Lappeenranta University of Technology.

Incropera, F. P. and DeWitt, D. P., (1985), *Fundamentals of Heat and Mass Transfer*, 2<sup>nd</sup> ed. New York: Wiley.

Jo, C., Seol, J. Y., and Ha, I. J., “Flux-weakening control of ipm motors with significant effect of magnetic saturation and stator resistance,” *IEEE Transactions on Industrial Electronics*, vol. 55, no. 3, Mar. 2008, pp. 1330–1340.

Kamiev, K., (2013), *Design and testing of an armature-reaction-compensated permanent magnet synchronous generator for island operation*, Doctoral dissertation, Acta Universitatis Lappeenrantaensis 539, Lappeenranta University of Technology.

---

Konetex (2011), *Teboil Fluid E product datasheet*, [Online], Available from [http://www.konetex.ee/failid/galerii\\_pildid/Teboil%20Fluid%20E%20ENG.pdf](http://www.konetex.ee/failid/galerii_pildid/Teboil%20Fluid%20E%20ENG.pdf) [Accessed 31 January 2014].

Li., Zhu, Z., Jiang, S. Z., Zhu, Z. Q., and Chan, C. C., “Analytical Methods for Minimizing Cogging Torque in Permanent-Magnet Machines,” *IEEE Transactions on Magnetics*, vol. 45, no. 4, 2009. pp. 2023–2031.

Lukic, S., and Emadi, A., “Effects of drivetrain hybridization on fuel economy and dynamic performance of parallel hybrid electric vehicles,” *IEEE Transactions on Vehicular Technology*, vol. 53, no. 2, March 2004 pp. 38–389.

Mellor, P. D., Roberts, D., and Turner, D. R., “Lumped parameter thermal model for electrical machines of TEFC design,” in *Proceedings of the IEEE*, B, vol. 138, no. 5 pp. 205–218, Sep. 1991.

Miller, T., “Optimal design of switched reluctance motors,” *IEEE Transactions on Industrial Electronics*, vol. 49, no. 1, Feb. 2002, pp. 15–27.

Miller, T.J.E. (1989), *Brushless Permanent-Magnet and Reluctance Motor Drives*, Oxford: Clarendon Press.

Miller, T.J.E., (1993), *Switched Reluctance Motors and their Control*, Hillsboro, OH and Oxford: Magna Physics Publishing and Clarendon Press.

Montonen J. and Pyrhönen J., “Performance Analysis of Tooth-Coil Permanent Magnet Traction Motors with Embedded Magnets and Saliency,” *International Review on Electrical Engineering*, vol. 11, no. 1, 2016, pp. 9–19.

Montonen J., Montonen J.-H., Immonen P., Murashko K., Ponomarev P., Lindh T., Lindh P., Laurila L., Pyrhönen J., Tarkiainen A., and Rouvinen A., “Electric Drive Dimensioning for a Hybrid Working Machine by Using Virtual Prototyping,” in *Proc. of the 20th International Conference on Electrical Machines (ICEM)*, Marseille, France, 2–5 September 2012, pp. 921–927.

Montonen J., Nokka J., Pyrhönen J., “Virtual Wheel Loader Simulation – Defining the Performance of Drive-Train Components,” *International Review on Modeling and Simulation*, vol. 9, no. 3, 2016, pp. 208–216.

Montonen, J. Lindh, P., and Pyrhönen, J., “Design Process of Traction Motor having Tooth-Coil Windings,” in *20th International Conference on Electrical Machines (ICEM)*, 2–5 September 2012, Marseille, France.

Montonen, J., Sinkko, S., Lindh, P., and Pyrhönen, J., “Design of a Traction Motor with Two-Step Gearbox for High-Torque Applications”, in *21th International Conference on Electrical Machines (ICEM)*, 2–5 September 2014, Berlin, Germany.

Morimoto, S., Takeda, Y., Hirasa, T., and Taniguchi, K., "Expansion of operating limits for permanent magnet motor by current vector control considering inverter capacity," *IEEE Transactions on Industry Applications*, vol. 26, no. 5, Sep./Oct. 1990, pp. 866–871.

Nalepa, R., Orłowska-Kowalska, T., "Optimum Trajectory Control of the Current Vector of a Non-Salient-Pole PMSM in the Field-Weakening Region," *IEEE Transactions on Industrial Electronics*, vol. 59, no. 7, 2012, pp. 2867–2876.

Nerg, J., Rilla, M., and Pyrhönen, J., "Thermal Analysis of Radial-Flux Electrical Machines with a High Power Density," *IEEE Transactions on Industrial Electronics*, vol. 55, no. 10, 2008, pp. 3543–3554.

Nerg, J., Rilla, M., Ruuskanen, V., Pyrhönen, J., and Ruotsalainen, S., "Direct-Driven Interior Magnet Permanent-Magnet Synchronous Motors for a Full Electric Sports Car," *IEEE Transactions on Industrial Electronics*, vol. 61, no. 8, August, 2014, pp. 4286–4294.

Lynwander, P., (1983) *Gear Drive Systems: Design and Application*, New York and Basel: Marcel Dekker, Inc. ISBN 0-8247-1896-8.

Pellegrino, G., Vagati, A., Boazzo, B., and Guglielmi, P., "Comparison of Induction and PM Synchronous Motor Drives for EV Application Including Design Examples," *IEEE Transactions on Industry Applications*, vol. 48, no. 6, November/December 2012, pp. 2322–2332.

Pellegrino, G., Vagati, A., Guglielmi, P., and Boazzo, B., "Performance comparison between surface-mounted and interior pm motor drives for electric vehicle application," *IEEE Transactions on Industrial Electronics*, vol. 59, no. 2, Feb. 2012, pp. 803–811.

Petrov, I. (2015), *Cost Reduction of Permanent Magnet Synchronous Machines*, Doctoral Dissertation, Acta Universitatis Lappeenrantaensis 638, Lappeenranta University of Technology.

Petrov, I., Ponomarev, P., Alexandrova, Y., and Pyrhönen, J., "Unequal Teeth Widths for Torque Ripple Reduction in Permanent Magnet Synchronous Machines With Fractional-Slot Non-Overlapping Windings," *IEEE Transactions on Magnetics*, vol. 51, no. 2, 2015, pp. 1–9.

Pippuri, J. (2010), *Finite Element Analysis of Eddy Current Losses in Steel Laminations of Inverter-Fed Electrical Machines*, Doctoral Dissertation, TKK Dissertations 245, Aalto University.

Ponomarev, P. (2013), *Tooth-Coil Permanent Magnet Synchronous Machine Design for a Special Applications*, Doctoral Dissertation, Acta Universitatis Lappeenrantaensis 531, Lappeenranta University of Technology.

- 
- Ponomarev, P., Polikarpova, M., and Pyrhönen, J., “Thermal Modeling of Directly-Oil Cooled Permanent Magnet Synchronous Machine,” in *ICEM*, 2–5 September 2012, Marseille, France.
- Pyrhönen, J., Jokinen, T., and Hrabovcová, V. (2014), *Design of Rotating Electrical Machines*, Chichester: John Wiley & Sons, Ltd.
- Qi, G., Chen, J. T., Zhu, Z. Q., Howe, D., Zhou, L. B., Gi, C. L., “Influence of Skew and Cross-Coupling on Flux-Weakening Performance of Permanent-Magnet Brushless AC Machines,” *IEEE Transactions on Magnetics*, vol. 45, no. 5, May 2009, pp. 2110–2117.
- Reddy, P. B., El-Refaie, A. M., Huh, K.-K., Tangudu, J. K., and Jahns, T. M., “Comparison of Interior and Surface PM Machines Equipped With Fractional-Slot Concentrated Windings for Hybrid Traction Applications,” *IEEE Transactions on Energy Conversion*, vol. 27, no. 3, 2012, pp. 593–602.
- Rilla, M., (2012), *Design of salient pole PM synchronous machines for a vehicle traction application – Analysis and Implementation*, Doctoral Dissertation, Acta Universitatis Lappeenrantaensis 497, Lappeenranta University of Technology.
- Rostami, N., Feyzi, M. R., Pyrhönen, J., Parviainen, A., and Niemelä, M., “Lumped-Parameter Thermal Model for Axial Flux Permanent Magnet Machines,” *IEEE Transactions on Magnetics*, vol. 49, no. 3, March 2013, pp. 1178–1184.
- Saber, A. Y., Venayagamoorthy, G. K., “Plug-in Vehicles and Renewable Energy Sources for Cost and Emission Reductions,” *IEEE Transactions on Industrial Electronics*, vol. 58, no. 4, April 2011, pp. 1229–1238.
- Salminen, P., Jokinen, T., and Pyrhönen, J., “The Pull-Out Torque of Fractional-slot PM-Motors with Concentrated Winding,” in *Proc. IEE Electric Power Applications*, vol. 152, pp. 1440–1444, 2005.
- Sinkko, S., Montonen, J., Gerami Tehrani, M., Pyrhönen, J., Sopanen, J., and Nummelin, T., “Integrated Hub-Motor Drive train for Off-Road Vehicles,” in *Proc. EPE'14 ECCE*, Lappeenranta, 26–28 August 2014.
- Song, X., Fang, J., Han, B., “High-Precision Rotor Position Detection for High-Speed Surface PMSM Drive Based on Linear Hall-Effect Sensors,” *IEEE Transactions on Power Electronics*, vol. 31, no. 7, July 2016, pp. 4720–4731.
- Stachowiak, G. and Batchelor, A. (2005), *Engineering Tribology*, 3<sup>rd</sup> ed., Burlington: Elsevier Butterworth-Heinemann, pp. 157–180.
- Stumberger, B., Stumberger, G., Dolinar, D., Hamler, A., and Trlep, M., “Evaluation of Saturation and Cross-Magnetization Effects in Interior Permanent-Magnet Synchronous

Motor,” *IEEE Transactions on Industry Applications*, vol. 39, no. 5, September/October 2003, pp. 1264–1271.

Tursini, M., Chiricozzi, E., and Petrella, R., “Feedforward flux-weakening control of surface-mounted permanent-magnet synchronous motors accounting for resistive voltage drop,” *IEEE Transactions on Industrial Electronics*, vol. 57, no. 1, Jan. 2010, pp. 440–448.

Wang, A., Jia, Y., and Soong, W. L., “Comparison of Five Topologies for an Interior Permanent-Magnet Machine for a Hybrid Electric Vehicle,” *IEEE Transactions on Magnetics*, vol. 47, no. 10, 2011, pp. 3606–3609.

Wang, K., Zhu, Z. Q., Ombach, G., and Chlebosz, W. “Average Torque Improvement of Interior Permanent-Magnet Machine Using Third Harmonic in Rotor Shape,” *IEEE Transactions on Industrial Electronics*, vol. 61, no. 9, 2013, pp. 5047–5057.

Welchko, B. A., Jahns, T. M., Soong, W. L., and Nagashima, J. M., “IPM Synchronous Machine Drive Response to Symmetrical and Asymmetrical Short Circuit Faults,” *IEEE Transactions on Energy Conversion*, , vol. 18, no. 2, 2003, pp. 291–298.

Wu, W., Dunlop, J., Collocott, S., and Kalan, B., “Design optimization of a switched reluctance motor by electromagnetic and thermal finite element analysis,” *IEEE Transactions on Magnetics*, vol. 39, no. 5, Sept. 2003, pp. 3334–3336.

Yamazaki, K. and Kumagai, M., “Torque Analysis of Interior Permanent Magnet Synchronous Motors by Considering Cross-Magnetization: Variation in Torque Components With Permanent-Magnet Configurations,” *IEEE Transactions on Industrial Electronics*, vol. 61, no. 7, 2014, pp. 3192–3201.

Zeraoulia, M., Benbouzid, M., and Diallo, D., “Electric motor drive selection issues for HEV propulsion systems: A comparative study,” *IEEE Transactions on Vehicular Technology*, vol. 55, no. 6, Nov. 2006, pp. 1756–1764.

Zhu, Z.Q., Wu, L.J., and Mohd Jamil, M.L., “Influence of Pole and Slot Number Combinations on Cogging Torque in Permanent-Magnet Machines With Static and Rotating Eccentricities,” *IEEE Transactions on Industry Applications*, vol. 50, no. 5, Sept.–Oct. 2014, pp. 3265–3277.

## Appendix A: Cooling oil datasheet

# Shell Spirax S3 AX 80W-90

*High Performance, GL-5 Axle Oil for General Applications*

Spirax S3 AX 80W-90 is a high performance, API GL-5 gear and axle oil for moderate to heavily loaded on and off-road driveline applications requiring SAE 80W-90 oil.

### Applications

- **Automotive Differentials**  
Automotive gear boxes, differentials, and hypoid gear sets in motorcycle, passenger car, commercial vehicles, off-road construction and agricultural equipment.
- **General Gear Sets**  
Ancillary equipment gear sets and some industrial equipment.

Outstanding pitting, scoring and wear protection.

### Specification and Approvals

API Service Classification	GL-5
US Military	MIL-L-2105D
Mercedes-Benz Sheet	Approval 235.6
MAN	342 Typ M2
ZF TE-ML	05A, 07A, 16C, 17B, 19B, 21A

### Performance Features and Benefits

- **Multiple Vehicle Applications**  
High performance fluid for API GL-5 applications that may require SAE 80W-90, 90, or 80W fluids. May be used in some SAE 75W-90 applications where low temperature performance is not needed..
- **Longer oil drain capability**  
Long life additives ensure long-term protection of the gears and high oxidation resistance so providing extended drain capability.
- **Longer transmission life**

### Advice

Advice on applications not covered in this leaflet may be obtained from your Shell Representative.

### Health and Safety

Guidance on Health and Safety are available on the appropriate Material Safety Data Sheet which can be obtained from your Shell representative.

### Protect the environment

Take used oil to an authorised collection point. Do not discharge into drains, soil or water.

### Typical Physical Characteristics

Spirax S3 AX 80W-90			
SAE Viscosity grade		SAE J 306	80W-90
Kinematic Viscosity		ISO 3104	
at 40°C	mm <sup>2</sup> /s		169.0
at 100°C	mm <sup>2</sup> /s		16.8
Density at 15°C	kg/m <sup>3</sup>	ISO 12185	900
Flash Point COC	°C	ISO 2592	220
Pour Point	°C	ISO 3016	-30

These characteristics are typical of current production. Whilst future production will conform to Shell's specification, variations in these characteristics may occur.



## ACTA UNIVERSITATIS LAPPEENRANTAENSIS

697. YANG, XIAOCHEN. Development of a welding production quality control and management system model for China. 2016. Diss.
698. LEMINEN, VILLE. Leak-proof heat sealing of press-formed paperboard trays. 2016. Diss.
699. LAAKSONEN, LAURI. Spectral retinal image processing and analysis for ophthalmology. 2016. Diss.
700. OINONEN, MINNA. Management of customer co-development in business-to-business markets. 2016. Diss.
701. ALATALO, SARA-MAARIA. Hydrothermal carbonization in the synthesis of sustainable porous carbon materials. 2016. Diss.
702. UZHEGOV, NIKITA. Design and material selection of high-speed rotating electrical machines. 2016. Diss.
703. RICHTER, CHRIS. Digital collaborations and entrepreneurship – the role of shareconomy and crowdsourcing in the era of smart city. 2016. Diss.
704. JAFARI, SHILA. Investigation of adsorption of dyes onto modified titanium dioxide. 2016. Diss.
705. PATEL, YOGINI. Computational modelling of non-equilibrium condensing steam flows in low-pressure steam turbines. 2016. Diss.
706. LEVCHUK, IRINA. Titanium dioxide based nanomaterials for photocatalytic water treatment. 2016. Diss.
707. AMOUR, IDRISSE. Variational ensemble kalman filtering applied to data assimilation problems in computational fluid dynamics. 2016. Diss.
708. SHESTAKOVA, MARINA. Ultrasound-assisted electrochemical treatment of wastewaters containing organic pollutants by using novel Ti/Ta<sub>2</sub>O<sub>5</sub>-SnO<sub>2</sub> electrodes. 2016. Diss.
709. OLEKSIENKO, OLGA. Physico-chemical properties of sol-gel synthesized titanosilicates for the uptake of radionuclides from aqueous solutions. 2016. Diss.
710. PATALA, SAMULI. Advancing sustainability-oriented innovations in industrial markets. 2016. Diss.
711. KUORIKOSKI, TERO. Kohti resonoivaa urheilujohtamista – Tavoitteen muodostuminen urheilun kentässä. 2016. Diss.
712. LAHTELA, VILLE. Improving the properties of solid Scots pine (*Pinus sylvestris*) wood by using modification technology and agents. 2016. Diss.
713. NEVARANTA, NIKO. Online time and frequency domain identification of a resonating mechanical system in electric drives. 2016. Diss.
714. FANG, CHAO. Study on system design and key technologies of case closure welding for ITER correction coil. 2016. Diss.
715. GARCÍA PÉREZ, MANUEL. Modeling the effects of unsteady flow patterns on the fireside ash fouling in tube arrays of kraft and coal-fired boilers.

716. KATTAINEN, JARI. Heterarkkisen verkostoyhteistyön johtamistarpeet verkoston muotoutumisvaiheessa. 2016. Diss.
717. HASAN, MEHDI. Purification of aqueous electrolyte solutions by air-cooled natural freezing. 2016. Diss.
718. KNUKTAS, ANTTI. Increasing beneficial interactions in a computer-supported collaborative environment. 2016. Diss.
719. OVASKA, SAMI-SEPPO. Oil and grease barrier properties of converted dispersion-coated paperboards. 2016. Diss.
720. MAROCHKIN, VLADISLAV. Novel solutions for improving solid-state photon detector performance and manufacturing. 2016. Diss.
721. SERMYAGINA, EKATERINA. Modelling of torrefaction and hydrothermal carbonization and heat integration of torrefaction with a CHP plant. 2016. Diss.
722. KOTISALO, KAISA. Assessment of process safety performance in Seveso establishments. 2016. Diss.
723. LAINE, IGOR. Institution-based view of entrepreneurial internationalization. 2016. Diss.
724. MONTECINOS, WERNER EDUARDO JARA. Axial flux permanent magnet machines – development of optimal design strategies. 2016. Diss.
725. MULTAHARJU, SIRPA. Managing sustainability-related risks in supply chains. 2016. Diss.
726. HANNONEN, JANNE. Application of an embedded control system for aging detection of power converter components. 2016. Diss.
727. PARKKILA, JANNE. Connecting video games as a solution for the growing video game markets. 2016. Diss.
728. RINKINEN, SATU. Clusters, innovation systems and ecosystems: Studies on innovation policy's concept evolution and approaches for regional renewal. 2016. Diss.
729. VANADZINA, EVGENIA. Capacity market in Russia: addressing the energy trilemma. 2016. Diss.
730. KUOKKANEN, ANNA. Understanding complex system change for a sustainable food system. 2016. Diss.
731. SAVOLAINEN, JYRKI. Analyzing the profitability of metal mining investments with system dynamic modeling and real option analysis. 2016. Diss.
732. LAMPINEN, MATTI. Development of hydrometallurgical reactor leaching for recovery of zinc and gold. 2016. Diss.
733. SUHOLA, TIMO. Asiakaslähtöisyys ja monialainen yhteistyö oppilashuollossa: oppilashuoltoprosessi systeemisenä palvelukokonaisuutena. 2017. Diss.
734. SPODNIAK, PETR. Long-term transmission rights in the Nordic electricity markets: An empirical appraisal of transmission risk management and hedging. 2017. Diss.

